CHEMICAL SYNTHESIS AND CHARACTERIZATION OF 3-LAYER $Bi_{2-y}Pb_ySr_2Nb_2Ti_{1-x}Al_xO_{12-\delta}$ AURIVILLIUS IONIC CONDUCTORS AND $La_{1-x}Sr_xCoO_3$ CATHODE CERAMICS

BY

BRIAN S. LUISI

A THESIS
SUBMITTED TO THE FACULTY OF

ALFRED UNIVERSITY

IN PARTIAL FULFILLMENT OF THE REQUIREMENTS
FOR THE DEGREE OF

MASTER OF SCIENCE

IN

MATERIALS SCIENCE

ALFRED, NEW YORK

APRIL, 2003

CHEMICAL SYNTHESIS AND CHARACTERIZATION OF 3-LAYER $Bi_{2-y}Pb_ySr_2Nb_2Ti_{1-x}Al_xO_{12-\delta}$ AURIVILLIUS IONIC CONDUCTORS AND $La_{1-x}Sr_xCoO_3$ CATHODE CERAMICS

BY

BRIAN S. LUISI

B.S. ALFRED UNIVERSITY (2001)

B.A. ALFRED UNIVERSITY (2001)

SIGNATURE OF AUTHOR_____(Signature on file)_____

APPROVED BY_____(Signature on file)_____
SCOTT MISTURE, ADVISOR

_____(Signature on file)_____
DOREEN EDWARDS, ADVISORY COMMITTEE

_____(Signature on file)_____
GARRETT J. McGOWAN, ADVISORY COMMITTEE

_____(Signature on file)_____
WALTER A. SCHULZE, CHAIR, ORAL THESIS DEFENSE

ACCEPTED BY_____(Signature on file)_____
RONALD S. GORDON, DEAN,
SCHOOL OF CERAMIC ENGINEERING
AND MATERIALS SCIENCE

Acknowledgements

Well, one masters thesis done. Along with this of course comes a distinguished list of advisors, colleagues, friends and brands of alcohol that made this all possible. I would like to thank Dr. Scott Misture, my thesis advisor, for allowing me a large degree of freedom to run (or at least randomly walk around) with my research in a direction I found interesting, while at the same time providing guidance, insights, and a vast store of knowledge. My committee members, consisting of Dr. Garrett McGowan and Dr. Doreen Edwards also have my gratitude. Dr. Mc"G" for proving, through his unique teaching style, that chemistry is both interesting and fun and Dr. Edwards for seeing me through two theses now.

The x-ray technician Slawomir "Swavek" Zdzieszynski has my deepest thanks for being a miracle worker in the lab. I have heard it said that Swavek can build/fix a diffractometer with any three objects. I now believe this claim to be true. I am also grateful to the rest of the x-ray gang for acting like a think tank and support group for all of its members. In particular I would like to acknowledge Michael Haluska for his help and unique sense of humor. That group of individuals known simply as the "glassholes" also has my appreciation. I would like to thank Matt Hall for always making himself available to help a friend as well as for loaning me some Gno Foam Gnomes™ at critical times.

My roommate and brother, Kevin "Nacho" Rowland, is deserving of a function of thanks that vaguely follows the cotangent of an exactly undefined variable known as the gremlin. I am indebted to our philosophical discussions on science, style, and the true meaning of beer. In addition, this brave soul was willing to split a living establishment for a number of years with me. Unfortunately the gremlin only has a shelf life of seven years or we might be still going.

Finally, I must thank my brother Mike and my parents for their support during my tenure at Alfred in the form of phone conversations, emails, large sums of money and an abundance of understanding.

Brian Luisi

5/13/03

Table of Contents

Page:

List of Tables

Page:

List of Figures

Page:

Abstract

Aurivillius phases of the type $Bi_2Sr_2Nb_2TiO_{12}$ and $Bi_{1.6}Pb_{0.4}Sr_2Nb_2Ti_{1-x}Al_xO_{12}$ ($0.0 \leq x \leq 0.8$) were synthesized by the polymerized complex method involving an organo-metallic precursor. The effect of raising the pH of the solution on the temperature of crystallization formation was investigated through the addition of ammonium hydroxide. Infrared (IR) and nuclear magnetic resonance (NMR) spectra were obtained at various points in the reaction to aid in developing a reaction mechanism. The spectroscopic data showed the formation of an ester as well as an amide with the addition of ammonium hydroxide after polymerizing to 170 °C. Inductively coupled plasma (ICP) spectroscopy qualitatively showed that bismuth, strontium, niobium and titanium ions were all volatilizing out with solvent evaporation. Pure $Bi_2Sr_2Nb_2TiO_{12}$ was formed after heat treatment for 5 hours at 900 °C. High temperature x-ray powder diffraction showed crystalline phase formation beginning at 700 °C. Phase pure Aurivillius structures were obtained with firing temperatures as low as 700 °C when the solution pH was adjusted to 9.00**.** A solubility limit of aluminum was discovered for $Bi_{1.6}Pb_{0.4}Sr_2Nb_2Ti_{1-x}Al_xO_{12}$ at $x \geq 0.4$. For $x \geq 0.4$ two additional phases that formed were identified as bismuth oxide and strontium-aluminum oxide by x-ray diffraction (XRD). Scanning electron microscope – backscattered electron (SEM-BSE) images confirmed the presence of two additional phases at $x = 0.6$ and $x = 0.8$. Total conductivity of $Bi_{1.6}Pb_{0.4}Sr_2Nb_2Ti_{1-x}Al_xO_{12}$ at 1123 K ranged from 1.74×10^{-4} $S \bullet cm^{-1}$ for $x = 0.0$ to 4.76×10^{-3} $S \bullet cm^{-1}$ for $x = 0.8$ stemming from oxygen vacancy formation as well as the evolution of bismuth oxide past the solubility limit.

$La_{1-x}Sr_xCoO_3$ ($0.1 \leq x \leq 0.9$) ceramics were also synthesized by the polymerized complex method. Rietveld refinement of x-ray powder diffraction data indicated that $La_{1-x}Sr_xCoO_3$ adopts a cubic unit cell from $0.9 \geq x \geq 0.7$, ultimately distorting to a rhombohedral unit cell at $x \leq 0.6$. The lattice parameter in the cubic unit cell ranged from 3.833(1) Å at $x = 0.7$ to 3.838(9) Å at $x = 0.9$. The lattice parameter and cell angle in the rhombohedral unit cell ranged from 5.3935(9) Å and 60.6866(9)° at $x = 0.1$ to 5.416(4) Å and 60.080(4)° at $x = 0.6$.

1. Introduction

1.1 Fuel Cell Operation

The basics of fuel cell operation are described by electrochemistry. An electrical current is produced by a spontaneous redox reaction, supported by an anode and cathode separated by an electrolyte. The fuel supplied at the anode is oxidized, which results in the release of electrons while the oxidant at the cathode is reduced. An oxidizing agent accepts electrons and is subsequently reduced. By contrast, a reducing agent gives up electrons and is oxidized.[1] Connecting an external circuit across the anode and cathode enables a flow of electrons. The electrolyte needs to serve in a variety of capacities. In order for the redox reaction to occur, the electrolyte must be capable of transporting ions. Depending upon the type of cell that has been designed, either protons must be transported through the electrolyte to cause reduction at the cathode or oxygen ions must be transported to induce oxidation at the anode. The oxidant and reductant need to be physically separated to prevent direct chemical reaction and passing the external circuit in the process.[1] As a result, the electrolyte must also be impermeable to the reagents that are oxidized and reduced. Figure 1.1 shows the components of a fuel cell. The overall fuel cell reaction can be described by the two half reactions occurring at the anode and cathode. For an electrochemical cell incorporating an oxygen ion conducting electrolyte that utilizes oxygen as the oxidant and hydrogen as the reductant the following half reactions describe the process:[2]

Cathode: $O_2 + 4e^- \rightarrow 2O^-$ (1)

Anode: $H_2 + 2O^- \rightarrow H_2O + 2e^-$ (2)

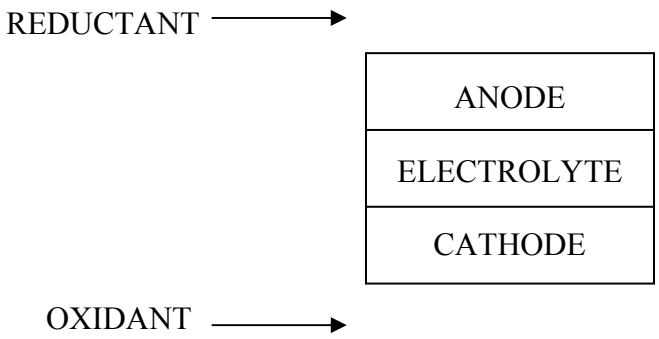

Figure 1.1. Schematic diagram of a fuel cell.

Electrical energy is produced by the free energy of oxidation of the fuel.[3] The change in free energy can be directly related to the voltage across the cell by the following equation:[1]

$$\Delta G_{rxn} = -nFV \tag{3}$$

assuming that

$$\frac{P_{H2O}}{P_{H2} * P_{O2}^{\frac{1}{2}}} = 1 \quad \text{for} \quad \Delta G_{rxn} = \Delta G_o + RT \ln \frac{P_{H2O}}{P_{H2} * P_{O2}^{\frac{1}{2}}} \tag{4) (5}$$

where n is the number of moles, F is Faraday's constant, V is the voltage, P_{H20} P_{H2} P_{O2} are the partial pressures of reactants and product and ΔG is the free energy of reaction.

A potential major advantage of a fuel cell is its theoretical unrestricted ability to operate at high efficiencies. Utilizing the free energy of a reaction to produce a current eliminates the efficiency problems experienced in heat engines by the Carnot cycle.[2] Another advantage is the absence of polluting by-products that are found in the emissions of vehicles. Other issues do arise however. In a Faradaic reaction mass and electron transfer must occur at a boundary where the electrode, electrolyte, and reacting phases are all in contact, posing some strict design specifications.[3] In addition, electrochemical kinetics will limit the electrical current.

1.2 Electrolytes

Electrolytes can either be solid or liquid so long as the design specifications are met. Fuel cells based on liquid electrolytes have been evaluated for potential use.[3,4] Alkaline fuel cells utilize pure oxygen and hydrogen as the reducing and oxidizing agents with an aqueous electrolyte containing potassium hydroxide. Alkaline fuel cells have previously been employed in aerospace applications.[3] The pure hydrogen and oxygen requirement of the cell increases the cost, however, which is likely to limit its use in commercial applications. The phosphoric acid fuel cell uses aqueous phosphoric acid as a proton conducting electrolyte. Air and a hydrocarbon are the reducing and oxidizing agents. Low cost and ease of availability of these components make this system attractive. A unit, which converts the hydrocarbon to usable hydrogen fuel is necessary, reducing the efficiency to around 40 percent.[3] Other problems that arise from liquid electrolytes involve management and containment of the liquid as well as material corrosion.[2] The difficulties that arise with liquid based electrolytes have prompted research into solid electrolytes.

Ceramic solid oxide electrolytes have several inherent advantages over liquid electrolytes. The solid electrolyte eliminates the natural problem of corrosion and the housing of a liquid.[2] In addition, the use of non-precious materials at the anode and cathode reduces cost.[2] Ceramic electrolytes also operate at temperatures greater than 600 °C. As a consequence, it possible to internally reform the hydrocarbon fuel, thus eliminating the need for an external unit.[2] A greater degree in design flexibility is also granted since all of the materials are solid. As a result, it is possible to fabricate an individual cell into very thin layers, which can be stacked on top of each other or designed into shapes that will maximize efficiency.[2] The conductivities of several potential electrolytes for solid oxide fuel cells have been measured and reported.[5-6] Yttria stabilized zirconia (YSZ) has been the electrolytic material of choice when studying solid oxide fuel cells. Zirconia assumes a cubic fluorite structure at high temperatures.[5] Doping of zirconia with yttria simultaneously stabilizes the cubic fluorite structure at lower temperatures and introduces oxygen vacancies.[6] This material still

suffers from high operating temperature requirements however, around 1000° C for thick electrolytes.[2] Several disadvantages are associated with high temperature use, such as degradation of the electrolyte over time and material stability.[5] This has prompted interest in developing new materials with lower operating temperatures.

Bismuth oxide also adopts a fluorite related structure at high temperatures in which one quarter of the oxygen sites are vacant.[5,6] The oxygen vacancies present in the high temperature δ-Bi_2O_3 phase yields a conductivity orders of magnitude higher than the low temperature phase.[5,6] Doping this structure with yttria will also stabilize the fluorite structure down to lower temperatures.[5] A problem associated with bismuth oxide is its tendency to reduce at low partial pressures of oxygen. Mixed electronic and ionic conduction will begin with reduction of Bi_2O_3.[5]

$Bi_2VO_{5.5}$ has demonstrated the highest conductivity among the Aurivillius phases to date.[5] $Bi_2VO_{5.5}$ goes through 2 structural changes, one at 450 °C and again at 570 °C. It is the high temperature γ phase that exhibits the highest conductivity.[5] Introducing dopants such as Cu into the $Bi_2VO_{5.5}$ framework helps to stabilize the γ phase at lower temperatures and results in conductivities two order of magnitude higher than undoped $Bi_2VO_{5.5}$.[5]

In the effort to increase the conductivities among those Aurivillius phases such as $Bi_2Nb_2Sr_2TiO_{12}$ that do not contain intrinsic vacancies, doping the A and B sites with aliovalent cations in order to introduce oxygen vacancies has been attempted. While this has produced some benefit, the conductivities of the extrinsic materials are still several orders of magnitude lower than their intrinsic counterparts.

1.2.1 Cogeneration

Another interesting feature of ceramic solid oxide electrolytes is the potential for cogeneration. Cogeneration is the simultaneous production of electricity and chemicals. Chemicals such as H_2S and NH_3 have ΔG values of combustion that are similar to that of molecular hydrogen.[7] Oxidation of these materials to SO_2 and NO would produce similar electrical outputs and at the same time generate chemicals that are currently

produced in commercial reactors.[7] Sulfuric acid is the most widely produced chemical in the world. The production of SO_2 from H_2S is one of the steps in that process, as shown in eq. (6).

$$H_2S + 3/2\ O_2 \longrightarrow SO_2 + H_2O \quad (6)$$

This oxidation reaction is also highly exothermic with a ΔG of –100 kcal/mole.[7] Vayenas et al.[7] have demonstrated the ability of H_2S to act as a reducing agent in a fuel cell at operating temperatures from 700 –850 °C while at the same time undergoing 99 percent oxidation to SO_3. Vayenas et al.[7] have also demonstrated the cogenerative ability of methanol fuel at temperatures between 550 and 700 °C.[7] In this reaction methanol is oxidized to formaldehyde at the anode as shown in eq. (7).

$$CH_3OH + 1/2\ O_2 \longrightarrow H_2CO + H_2O \quad (7)$$

At 650 °C the potential of this reaction is 1.089 V which is larger than that of molecular hydrogen at 1.008 V thus making this system especially attractive.[7]

1.2.2 Aurivillius Phases

Perovskite structures have been the source of recent interest as potential electrolyte materials in solid oxide fuel cells due to their oxygen conducting behavior. In particular, the perovskite-related Aurivillius phases have shown promise as oxygen conducting electrolytes at reduced temperatures.[5] Aurivillius[8] first described a class of materials containing intergrowths of bismuth oxide separating layers of perovskite blocks in 1949. Aurivillius phases are composed of perovskite layers with the composition $(A_{n-1}B_nO_{3n+1})^{2-}$ separated by sheets of $(Bi_2O_2)^{2+}$.[5,6,9,10] Combining of these two layers yields the general formula $Bi_2A_{n-1}B_nO_{3n+3}$ for Aurivillius phases, where n denotes the number of perovskite layers in the structure, A is a large electropositive cation such as Ba, Sr, Ca, Bi or Pb and B is a small transition metal such as Ti, Nb, Ta, Mo, W, or Fe.[5,9,10] Aurivillius structures with n=1 to n=4 layers have been synthesized

and tested.[5] Doping such phases with aliovalent cations will introduce oxygen vacancies, thus increasing the ionic conductivity.[5,9,10] Figure 1.2 a four-layered Aurivillius structure.

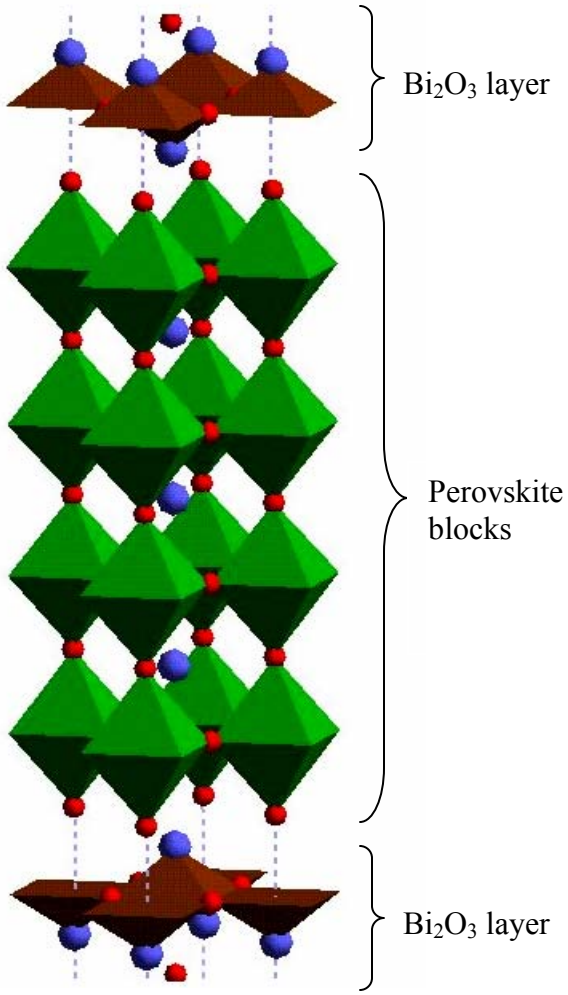

Figure 1.2. Structure of an n = 4 Aurivillius phase showing the polyhedral sites.

In 1993 Tomas et al.[9] and in 1995 Kendall et al.[10] reported on the successful substitution of gallium and aluminum into the 3-layer Aurivillius structure $Bi_2Sr_2Nb_2TiO_{12}$ by solid-state synthesis. Electrical characterization of the oxygen deficient $Bi_2Sr_2Nb_2MO_{11.5}$ led to conductivities as high as 1.2 x 10^{-2} S/cm when M = Al and 2.0 x 10^{-2} S/cm when M = Ga at 1073 K.[5] In comparison, YSZ has a conductivity of approximately 3.2 x 10^{-2} at 1073 K.[11] The potential for engineering electrolytes with extrinsic vacancies that exhibit superior conductivities seemed to be possible through selectively doping with aliovalent cations. Additional research was conducted on oxygen deficient and charge compensated Aurivillius phases by several researchers, with the goal of obtaining a better understanding of the structural and electrical mechanisms that were occurring with cation doping.[11-18] It has since been conclusively determined that there is a limit to the range of cation doping the structure will accept on the B-site.[12-14,18] In 2003, Lightfoot et al.[12] published substituting gallium for titanium in $Bi_2Sr_2Nb_2TiO_{12}$. An extra peak appeared in the x-ray powder diffraction pattern for $Bi_2Sr_2Nb_2GaO_{11.5}$ at 28° 2-theta, which was not present for $Bi_2Sr_2Nb_2TiO_{12}$.[12] Kendall et al.[10] claimed a phase pure specimen had been synthesized and indexed the extra peak as a (106) reflection. Detailed studies by Lightfoot[10-13] as well as Modi,[11] Say,[17] and Speakman[18] through x-ray and neutron powder diffraction, SEM, TEM, EDS and AC impedance spectroscopy have, in fact, proven that the extra peak is due to the evolution of bismuth oxide stemming from a solubility limit, which exists at approximately $x \geq 0.4$ for $Bi_2Sr_2Nb_2Ti_{1-x}M_xO_{12-\delta}$.

The ionic radius of $Ga^{3+}$and Ti^{4+} at 0.62 Å and 0.605 Å, respectively, are closely matched.[19] It is reasonable to conclude, therefore, that it is oxygen vacancies that the Aurivillius structure is intolerant to and not a cation size mismatch. Rentschler et al.[15,16] conducted studies on Aurivillius phases substituted with Pb^{2+} for Bi^{3+} on the A-site and charge compensated on the B-site by substituting cations such as Nb^{5+} for Ti^{4+} and Nd^{3+} for Sr^{2+}. For the n = 2 Aurivillius composition $Bi_{2-x}Pb_xSr_{1-x}Nd_xNb_2O_9$ phase pure specimens were obtained across the range $0.0 \leq x \leq 1.0$.[15] Furthermore, the 3-layer charge compensated compositions $Bi_{4-x}Pb_xTi_{3-x}Nb_xO_{12}$, $Bi_{2-x}Pb_xLa_2Ti_{3-x}Nb_xO_{12}$, $Bi_{2-x}Pb_xSr_{2-x}La_xTiNb_2O_{12}$, $(0 \leq x \leq 1)$ and $Bi_2Sr_{2-y}Pb_yTiNb_2O_{12}$ $(0 \leq y \leq 2)$ were synthesized

as phase pure specimens.[16] The work by Rentschler et al.[15,16] further supports the conclusion that it is oxide ion vacancies to which the Aurivillius crystal structure is intolerant.

1.3 AC Impedance Spectroscopy and DC Conductivity Measurements

Impedance spectroscopy has been utilized to study the electrical properties of PTCR materials,[20] ferroelectrics[21] and solid electrolytes.[11,17] AC impedance spectroscopy provides a means of distinguishing between the electrical behavior of different microstructural regions such as grains and grain boundaries in ceramics by sweeping the frequency of the measurement and analyzing the response.[20,21] An equivalent circuit, which models the behavior of the sample, is necessary in order to interpret the data.[20] The equivalent circuit is usually set up as parallel RC elements set in series, where each element in the circuit is responsible for modeling a portion of the microstrucure.[20] The individual RC elements are related to the frequency by:[22]

$$RC = \frac{1}{2\Pi\nu} \tag{8}$$

Figure 1.3 shows a schematic of the RC arcs one might expect to obtain in a typical AC impedance plot. Z'' is the complex portion of the impedance and Z' is the real component.

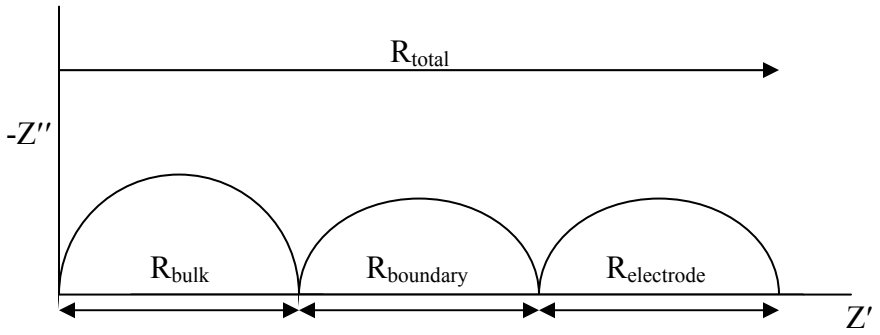

Figure 1.3. Idealized complex (Z'') and real (Z') AC impedance response of an electro-ceramic for the grain bulk, grain boundary and electrode effects.

Ideally, a series of arcs is obtained from each RC element corresponding to the resistance and capacitance of each microstructural feaure.[20,21] The high frequency arc is generally attributed to the response from the bulk of the sample, with the second arc representing the electrical behavior of the more resistive grain boundary. Finally, any electrode response will be modeled by a third, low frequency arc.[11] As a result, it can be safely assumed that a measured third low frequency arc is due to electrode behavior. Raising the temperature at measurement should result in a decrease in the conductive resistance of the sample.[11] The conductivity (σ) in Siemens per centimeter at a given temperature is then determined from the resistance and the dimensions of the sample.[11]

$$\sigma\,(T) = A * \exp\left(\frac{-E_a}{RT}\right) \tag{9}$$

where A is a constant, T is the temperature in Kelvin, R is the gas constant, and E_a is the activation energy . An Arrhenius style conductivity plot can then be constructed where the y-axis is plotted as $\log_{10}$ conductivity and the x-axis takes the form of 1000/T (Kelvin). From the slope of the graph the activation energy (E_a) can be determined, as in equation 8:[17]

$$E_a = -2.303 * k * \left[\frac{\partial \log(\sigma)}{\partial(1/T)}\right] \tag{10}$$

where k is Boltzmann's constant and T is the temperature in Kelvin.

While AC impedance involves placing an alternating current on the sample and measuring the electrical response, DC conductivity tests utilize a direct current. Under an alternating current a material's response is affected by the frequency of measurement. The effect is eliminated with a direct current. As such, phenomena that may not develop under AC, such as polarization, may occur in DC. DC conductivity tests can be valuable as a comparison to AC data to help determine a model for the sample in question.

1.4 Synthesis

Processing of mixed cation oxides has primarily proceeded by solid-state synthesis with some research involved in developing wet chemical methods.[9,10,13-16,32,33] Solid-state synthesis is a time consuming process that does not quickly generate homogenous, phase pure compounds. Wet chemical methods should drastically reduce the processing time through mixing at the atomic level. Wet chemical synthesis also naturally lends itself to highly pure, homogenous products.[30] A drawback has been the complexity of the solution chemistry of these reactions. Many variables such as temperature, pH, concentration, solvent, and aging time can have dramatic effects on the reaction mechanism if altered only slightly and so may affect the final product. If the above mentioned conditions can be addressed and optimized the potential benefits of low temperature wet chemical synthesis can be realized.

Solid-state synthesis has been a popular route for processing Aurivillius phases due to its simplicity. The powders of interest are simply mixed together and heat treated for an extended period of time. The firing temperature may be different for different compositions and several heat treatments at varying temperatures must usually be made in order to determine the optimal conditions. Solid-state synthesis is characterized by a slow cation interdiffusion process.[23] In order to achieve phase pure compounds a sufficient heating time is necessary. The total time required for heat treatment is one of the major disadvantages associated with solid-state synthesis. Somewhere between two and four days of heat treatment time is usually necessary in order to achieve phase pure compounds.[24] Nevertheless, many researchers continue to process Aurivillius phases by the solid-state route.[11-17,25]

Molten salt synthesis has been another method utilized for processing Aurivillius phases.[24,26-28] Molten inorganic salts are mixed to form a eutectic that acts as a medium for crystal growth.[24] Sodium chloride and potassium chloride are two common salts used for this process. The powders are mixed with the molten salts prior to heat treatment. Maalal et al.[26] report heat treatment times of 1 hour at 650 °C to ensure homogenization followed by further heating at 800-900 °C for 1 hour.[26] The mixture is subsequently

washed with water to remove the excess salts. Reductions in firing time and temperature as compared to solid-state synthesis are two advantages associated with this process.[24,26]

A variety of oxides have been prepared by the polymerized complex or Pechini method.[23,29-42] Figure 1.4 details the general steps that are required in an organo-metallic precursor route.[33,35,37,39] The polymerized complex method appears to be universal in its ability to generate homogenously distributed mixed cations that can later be calcined into their respective oxides. Cation salts that have been successfully used in the procedure so far include nitrates, chlorides, carbonates, isopropoxides and hydroxides.[31] The solution of mixed cations is added to citric acid and ethylene glycol. Hydrochloric or nitric acid is often used as a solvent for those cations that will not directly dissolve in citric acid or ethylene glycol. Mixing of the cations at around 60° C proceeds until the solution is totally transparent to ensure that no precipitation has occurred. Chelation of the metal ions happens at this point. Figure 1.5 depicts the chelation of a metallic cation with citric acid.[31] When the temperature is raised to 130° C the citric acid esterifies with the ethylene glycol. The esterification reaction repeats itself in the solution until a polymeric resin is obtained. Figure 1.6 illustrates a monomer in the polymeric backbone.

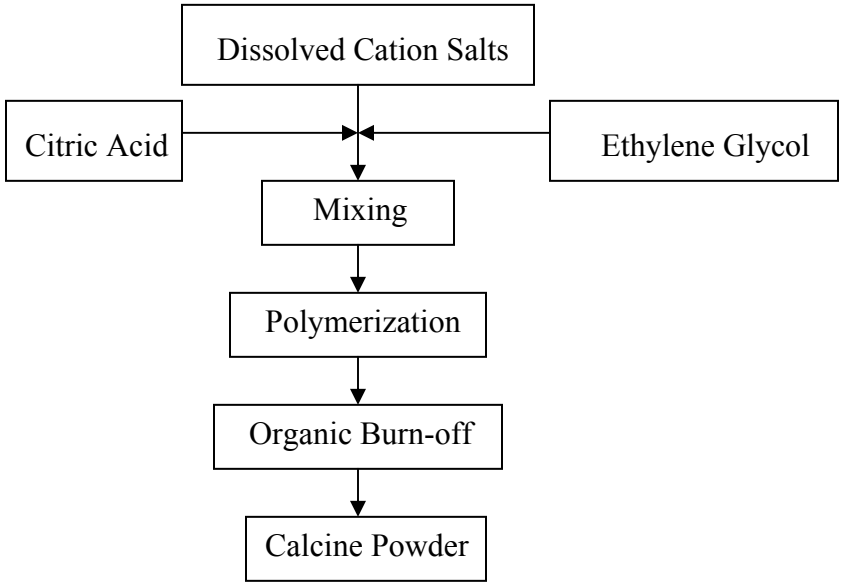

Figure 1.4. Generalized flow chart of the polymerized complex method.

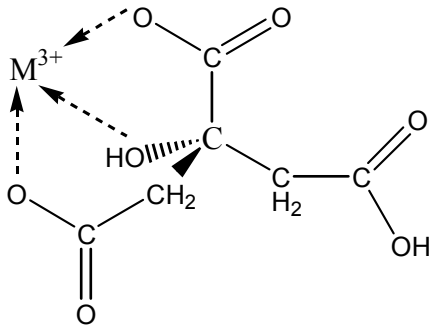

Figure 1.5. Chelation of a trivalent cation by citric acid.

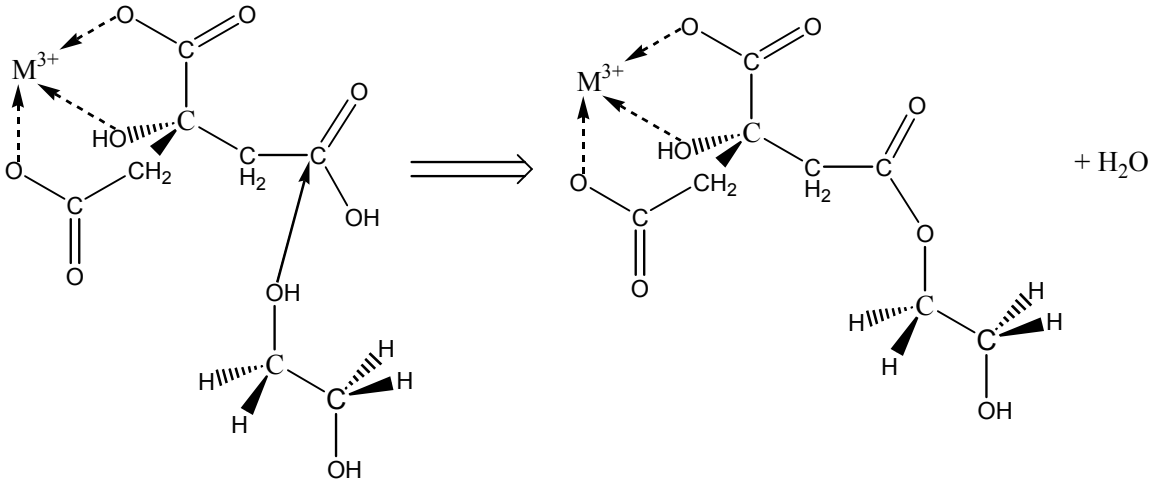

Figure 1.6. Fischer esterification of ethylene glycol with citric acid.

The mixed cations should now be atomically mixed and locked into fixed positions. Raising the temperature to 350° C will cause organic burn-off leaving a solid powder. The resulting powder is then calcined from 400° - 900 °C to form the oxide.

1.4.1 Past Synthetic Work

Udawatte et al.[39,40] have reported the synthesis of $BaSnO_3$ and $SrSnO_3$ by the polymerized complex method at reduced temperatures.[39,40] Tin chloride and barium carbonate salts were used as the reagents to form $BaSnO_3$.[39] Strontium carbonate was

used to make $SrSnO_3$.[39] The precursors were dissolved in ethylene glycol and citric acid. The resulting powders were calcined from 400 to 900 °C.[39] From XRD data, crystallization was reported to begin between 500 and 600 °C without the formation of an intermediate phase.[39] Increasing the calcining temperature from 500 to 900 °C increased the relative peak heights characteristic of $BaSnO_3$ and $SrSnO_3$.[39,40] The formation of cubic phase $BaSnO_3$ with a perovskite structure and $SrSnO_3$ with a perovskite structure was reported.[39,40] It was found that $SrSnO_3$ does not form a perfect cubic perovskite but rather one with a slightly distorted unit cell. Raman spectroscopy indicated trace amounts of $BaCO_3$, SnO_2, and $SrCO_3$ in samples heated at 900°C.[39,40] Calcining to temperatures above 1000°C eliminated the secondary phases peaks.[39,40]

Zanetti et al.[33] have reported on the successful synthesis of $SrBi_2Nb_2O_9$ thin films by chemical aqueous solution chemistry at low temperatures.[33] Strontium carbonate, niobium ammonium oxalate, and bismuth oxide were the precursors used in the reaction.[33] Chelation of the niobium by citric acid was first achieved by dissolving of the precursor in water, which precipitated as $Nb(OH)_5$ upon addition of NH_4OH.[33] The niobium hydroxide was added to citric resulting in chelation.[33] A mixture of nitric acid and water was used to get the strontium carbonate and bismuth oxide into solution.[33] The solution of strontium and bismuth ions was then added to the niobium citrate solution. Ethylenediamine was added until a slightly basic solution was obtained, whereupon ethylene glycol was introduced to induce polymerization.[33] Thin films were created by dip coating onto a $Pt/Ti/SiO_2/Si$ substrate.[33] The samples were heat treated from 400 to 700 °C.[33] Characterization was carried out by grazing incidence XRD. Crystallization of the perovskite phase at 650 °C was observed with an increase in crystallinity at higher treatment temperatures of 700° C.[33]

Schulz and Martin[36] reported on the processing of $La_{1-x}Sr_xGa_{1-y}Mg_yO_{3-(x+y)/2}$ by the polymerized complex method. Nitrate salts of the mixed cations were dissolved in ethylene glycol and citric acid.[36] Utilizing nitric acid as a catalyst the polyester gel was generated. Upon completion of the reaction the product was heated to 1000°C and held

for 24 hours.[36] Pellets were pressed out of this powder and further heat treated to 1400°C. X-ray diffraction data showed good relation to the pure parent compound, lanthanum gallate, with shifted lattice parameters caused by doping.[36] The authors report that lanthanum gallate, in addition to doped samples with compositions of $La_{0.9}Sr_{0.1}Ga_{0.9}Mg_{0.1}O_{2.9}$ and $La_{0.8}Sr_{0.2}Ga_{0.8}Mg_{0.2}O_{2.8}$ have been successfully prepared by this method.[36]

Kakihana and Domen[23] have prepared $KTiNbO_5$ photo-catalysts by the polymerized complex method. The titanium and niobium were dissolved as salts and added to a mixture of citric acid and ethylene glycol.[23] Although the monovalent potassium does not undergo chelation with citric acid it is still held in the polymeric gel.[23] As a result the potassium is homogenously distributed in the network along with the cations. The resulting powder was calcined at 700°C.[23] An attempt at synthesizing the same phase by solid-state reaction at 1100°C was also done so that a comparison could be made.[23] The X-ray diffraction pattern of the sample prepared by the polymerized complex method only contained peaks generated by $KTiNbO_5$.[23] In contrast to this, a significant amount of other unidentified phases were present in the X-ray pattern in the sample prepared by solid-state synthesis.[23] The authors attributed this to possible volatilization of potassium.[23] The loss of potassium is dependent upon temperature and heat treatment time, both of which are greater in the solid-state reaction as well as the degree of homogeneity in the mixture.[23] According to the authors, since the solid-state reaction relies upon the interdiffusion of cations by slow kinetics, some volatilization of potassium is unavoidable at a heat treatment of 1100°C prior to formation of stoichiometric $KTiNbO_5$.[23] The polymerized complex method on the other hand drastically improves cation homogeneity, which allows the reaction to proceed with minimum diffusion, thus lowering the heating time and temperature.[23] As a result a nearly stoichiometric amount of $KTiNbO_5$ is formed.[23]

Duran et al.[32] have reported the synthesis of Aurivillius phases with the composition $Bi_7Ti_4NbO_{21}$ by a metal-organic precursor method. Titanium(IV)tetrabutoxide, niobium pentachloride, and bismuth nitrate were the cationic

precursors.[32] The titanium reagent was first dissolved in ethylene glycol.[32] Nitric acid and hydrochloric acid were utilized to dissolve the other cation salts.[32] As with the experiments noted previously, the solutions were added to citric acid and ethylene glycol and heated to obtain a polymeric resin. Calcining of the powders was carried out from 400 to 800 °C.[32] X-ray diffraction and DTA data showed that the conversion from the amorphous precursors into crystalline $Bi_7Ti_4NbO_{21}$ occurred between 394 and 494 °C.[32] The authors suggested that an intermediate phase of $Bi_{20}TiO_{32}$ is first formed with a tetragonal structure.[26] The tetragonal phase was evident in the XRD pattern taken at 375°C.[26] As noted in the previous experiments an increase in the relative heights of the XRD peaks associated with the crystalline oxide occurs with increasing calcining temperature. The same holds true in this case with well crystallized orthorhombic $Bi_7Ti_4NbO_{21}$ forming at 800°C.[26]

1.5 $La_{1-x}Sr_xCoO_3$ Cathode Ceramics

$LaCoO_3$ perovskite oxides and related systems have been explored for their features in a variety of fields. The possibilities of using $La_{1-x}Sr_xCoO_3$ as an oxidation Catalyst,[2] as well as $LaNi_{1-x}Co_xO_3$[43] and $La_{1-x}Sr_xCo_{1-y}Fe_yO_{3-\delta}$[44] as potential electrode materials for solid oxide fuel cells have been studied. Sr doped $LaCoO_3$ has exhibited potential as an electrode material in oxide fuel cells and other electrochemical devices stemming from its conductive behavior.[45,46] Compositions in the $La_{1-x}Sr_xCoO_3$ family show high electrical conductivities with the material ultimately behaving like a metal at compositions of $x \geq 3$.[47] The stability of this material in air at elevated temperatures makes $La_{1-x}Sr_xCoO_3$ of particular interest. $LaCoO_3$ exists as a rhombohedral perovskite structure at room temperature.[48] The introduction of strontium atoms into the $LaCoO_3$ framework is expected to create structural changes resulting from the larger ionic radius of Sr^{2+}. Sr^{2+} has an ionic radius of 0.140 nm compared to the La^{3+} radius of 0.130 nm.[19]

There are four existing Powder Diffraction File[49] (PDF) entries for $La_{1-x}Sr_xCoO_3$ in the PDF database where $0.9 \geq x \geq 0.1$. Table I-1 lists the information found in the Powder Diffraction File. The Inorganic Crystal Structure Database[50] (ICSD) contains

structures and lattice parameters obtained by neutron powder diffraction for the $La_{1-x}Sr_xCoO_3$ family with values reported between x = 0.45 and x = 0.9. Table I-2 summarizes the information found in the ICSD. Kirchnerova and Hibbert[51], using XRD, reported oxygen deficient $La_{0.8}Sr_{0.2}CoO_{3-\delta}$ as orthorhombic and $La_{0.5}Sr_{0.5}CoO_{3-\delta}$ as tetragonal.

Table I-1. The Unit Cell Information from the PDF for $La_{1-x}Sr_xCoO_3$ Prior to This Work.

Composition	a (nm)	c (nm)	Smith-Snyder F_N	Crystal System	PDF Card #
$La_{0.7}Sr_{0.3}CoO_3$	0.54406	1.31950	F_{20}=67.2(.0119,25)	Rhombohedral	51-0405
$La_{0.5}Sr_{0.5}CoO_{2.91}$	0.543	1.32516	F_{22}=71.6(.0106,29)	Rhombohedral	48-0122
$La_{0.4}Sr_{0.6}CoO_{3-x}$	0.38342	NA	F_{18}=70.9(.0141,18)	Cubic	48-0121
$La_{0.5}Sr_{0.5}CoO_3$	0.537182	1.30780	Calculated	Rhombohedral	87-1082
$La_{0.6}Sr_{0.4}CoO_3$	0.537424	1.30750	Calculated	Rhombohedral	87-1081
$La_{0.7}Sr_{0.3}CoO_3$	0.535775	1.298481	Calculated	Rhombohedral	87-1080
$La_{0.8}Sr_{0.2}CoO_3$	0.539642	1.3084444	Calculated	Rhombohedral	87-1079
$La_{0.9}Sr_{0.1}CoO_3$	0.535935	1.298282	Calculated	Rhombohedral	87-1078

Table I-2. The Unit Cell and Space Group from the ICSD Database for $La_{1-x}Sr_xCoO_3$ Prior to This Work.

Composition (x)	a (nm)	C (nm)	Cell Volume (nm^3)	SG	Crystal System	ICSD Entry #
0.45	0.3831	NA	0.0562	Pm-3m	cubic	43178
0.5	0.535	NA	0.1089	R-3cR	trigonal	82818
0.6	0.535	NA	0.109	R-3cR	trigonal	82817
0.6	0.3874	NA	0.0581	Pm-3m	cubic	86943
0.6	0.5416	1.3192	0.3351	R-3cH	trigonal	86944
0.7	0.532	NA	0.1076	R-3cR	trigonal	82816
0.7	0.54	NA	0.1124	R-3cH	trigonal	43177
0.7	0.5441	1.3195	0.3382	R-3cH	trigonal	50708
0.8	0.536	NA	0.110	R-3cR	trigonal	82815
0.9	0.532	NA	0.1076	R-3cR	trigonal	82814

1.5 Current Work

Aurivillius phases of the type $Bi_{2-x}Pb_xSr_2Nb_2Ti_{1-y}Al_yO_{12-\delta}$ were synthesized by the polymerized complex method for electrical, microstructural, and crystal structure characterization. At various steps in the reaction process samples were taken and characterized. Infrared spectroscopy and C^{13} NMR showed how the chelation and polymerization reactions proceeded. The intensities and locations of the peak shifts depicted whether or not chelation and esterification followed by polymerization actually occurred.

X-ray diffraction and inductively coupled plasma (ICP) spectroscopy was also used to characterize the samples. High temperature X-ray diffraction (XRD) data indicated at what temperature crystallization was occurring. In addition XRD was used to analyze for phase purity and to refine lattice parameters. Evaporation of the solvent during processing may result in the loss of one or more cations, thus affecting the stoichiometry. ICP analysis of condensed solvent after evaporation indicated if any cations are lost through volatilization.

Microstructural analysis proceeded by scanning electron microscopy. Secondary electron imaging was used to measure grain size and image grain boundaries. Backscattered electron detection was utilized in conjunction with XRD to determine the presence of any secondary phases. Elemental analysis was carried out by energy dispersive spectroscopy (EDS). Electrical characterization was completed by AC and DC impedance spectroscopy.

$La_{1-x}Sr_xCoO_3$ with $0.1 \leq x \leq 0.9$ was synthesized by the polymerized complex method with the ultimate goal of refining the unit cell metrics.

2. Experimental Procedure

2.1 Aurivillius Specimens

2.1.1 Synthesis

Synthesis of all specimens was carried out by a modified Pechini process, or the polymerized complex method. Figure 2.1 depicts a flow chart of the synthetic route used to form the $Bi_2Sr_2Nb_2TiO_{12}$ and $Bi_{1.6}Pb_{0.4}Sr_2Nb_2Ti_{1-x}Al_xO_{12-\delta}$ ($0.0 \leq x \leq 0.8$) Aurivillius specimens under investigation. Stoichiometric amounts of the precursor powders were individually weighed out and mixed together in solution. The starting powders consisted of Bi_2O_3 (Alfa-Aesar, 99.99%), $Sr(NO_3)_2$ (Alfa-Aesar, 98%), $NbCl_5$ (Alfa-Aesar, 99%), Ti(IV)butoxide (Alfa-Aesar, 99+%), $Al(NO_3)_3 \bullet 9H_2O$ (Alfa-Aesar, 98%),

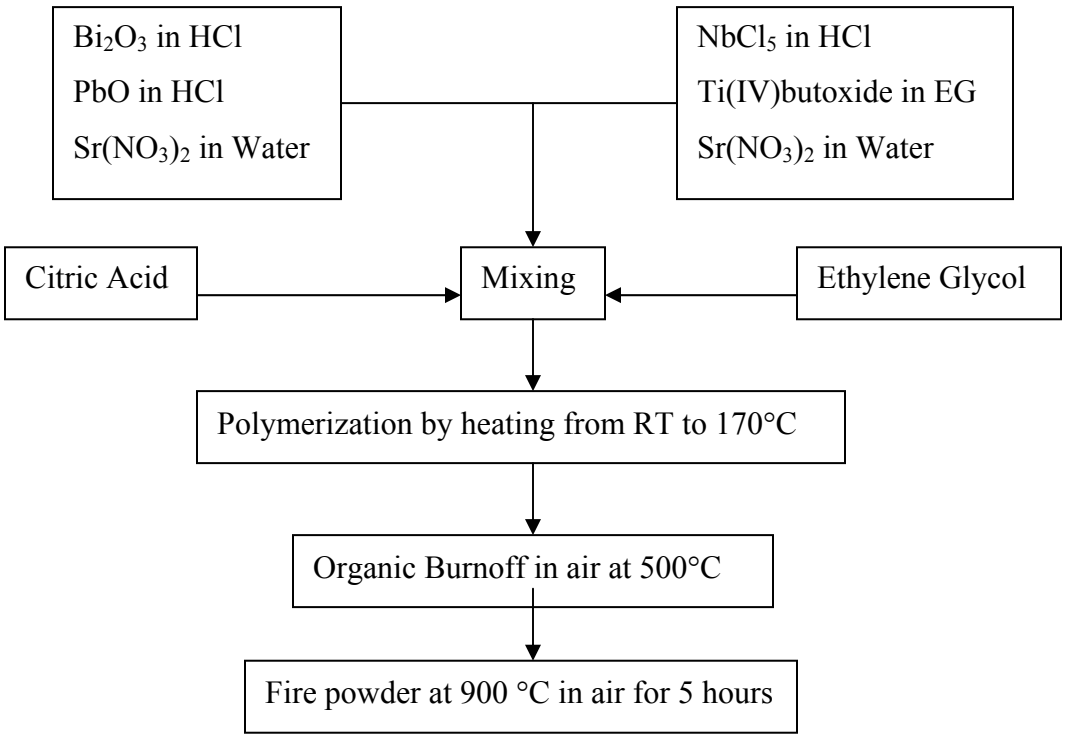

Figure 2.1 Flow chart of the synthesis of $Bi_{2-y}Pb_ySr_2Nb_2Ti_{1-x}Al_xO_{12-\delta}$ ($0.0 \leq x \leq 0.8$) (y = 0.0 and 0.4).

and PbO (Acros, 99.9+%). Strontium nitrate and aluminum nitrate were each dissolved in 20 ml of deionized water. Bismuth oxide was dissolved in a 20 ml solution of 36.5% - 38% HCl in water (Alfa-Aesar). Lead oxide was dissolved in 40 ml of a heated solution of the hydrochloric acid on a magnetic hot plate with stirring. Some evaporation of the solvent during dissolution occurred, which subsequently affected the molar concentration. The niobium(V)chloride was dispensed in a glove box under nitrogen atmosphere to prevent oxidation of the precursor and subsequently dissolved in 20 ml of the solution of hydrochloric acid. Titanium(IV)butoxide was dissolved directly into ethylene glycol. Table II-1 details the mass of the individual precursor powders used in the $Bi_{1.6}Pb_{0.4}$ $Sr_2Nb_2Ti_{1-x}Al_xO_{12-\delta}$ compositions. After all of the cations were individually dissolved they were combined in a beaker. To this solution, a 30 mole % excess of citric acid was added to chelate the metal cations. Ethylene glycol was then added in a 4:1 mole ratio with citric acid. Ammonium hydroxide was added at this point to raise the pH of the solution to the desired level. Solutions with pH levels of 3.00, 6.00, and 9.00 ± 0.05 were created to test the effect of pH on phase formation with firing temperature. The solution of mixed cations, ethylene glycol and citric acid was stirred magnetically while heating on a hot plate to 135°C to cause evaporation of the solvents. Polymerization of the citric acid with ethylene glycol resulted in the formation of a viscous liquid. The polymerization reaction was carried to completion in a drying oven in air at 170°C for 8 hours.

Table II-1. Masses of the Precursor Powders for the Composition $Bi_{1.6}Pb_{0.4}$ $Sr_2Nb_2Ti_{1-x}Al_xO_{12-\delta}$.

Composition	Mass (g) Bi_2O_3	Mass (g) $Al(NO_3)_3$	Mass (g) $Sr(NO_3)_3$	Mass (g) $NbCl_5$	Mass (g) PbO	Mass (g) Ti(IV)butoxide	Mass (g) Product
X = 0.0	3.0000	0.0000	3.4064	4.3486	0.7185	2.7392	8.1961
X = 0.2	4.0000	0.8051	4.4518	5.7982	0.9580	2.9218	10.8833
X = 0.4	2.5000	1.0063	2.8386	3.6239	0.5987	1.3696	6.7740
X = 0.6	3.0000	1.8114	3.4064	4.3486	0.7185	1.0957	8.0952
X = 0.8	3.0000	2.4152	3.4064	4.3486	0.7185	0.5478	8.0616

The organics were burned off in a Pyrex beaker at 500°C in air for 5 hours and the resulting powder fired in air in an MgO crucible at 900°C for 5 hours with a heating and cooling rate of 5°C per minute. Samples that contained lead substitution were pressed into pellets and buried in a sacrificial powder bed to prevent lead loss during firing to 900°C. Pellets were pressed to 34.5 MPa with a ½ inch die in a Carver press for one minute.

2.1.2 Phase Analysis

2.1.2.1 Infrared Spectroscopy (FT-IR)

A Thermo-Nicolet Nexus 670 infrared spectrometer was used to obtain infrared spectra of the solution and the polymerized product. Samples were drawn out of solution for IR analysis at temperatures of 85°C, 115°C, 135°C and 170°C. The samples were then allowed to cool to room temperature prior to data acquisition. The goal was to track what functional groups were present as a function of temperature and eventual polymerization. An average of 32 FT-IR scans with a resolution of 0.2 cm^{-1} was used to generate each spectrum. Spectra were obtained under transmission across sodium chloride plates for liquid samples and attenuated total reflectance for solid samples and considered with respect to percent transmission.

2.1.2.2 Nuclear Magnetic Resonance (FT-NMR)

A Perkin-Elmer Hitachi R-1500 "permanent magnet" 60 MHz FT-NMR was utilized to generate ^{1}H NMR spectra of the solution at reaction intervals of 100°C, 115°C, and 135°C. Samples for analysis were taken from the same sample stock vials and temperature intervals used for the IR experiments. The liquid samples were dissolved in deuterium oxide with 1 weight percent 3-(trimethylsilyl)-1-propane sulfonic acid sodium salt (DSS) added as a reference (Aldrich, 99.9%).

2.1.2.3 Inductively Coupled Plasma - Optical Emission (ICP-OES)

A Perkin-Elmer Optima 3000DV ICP-OES was used for qualitative elemental analysis of solvent that condensed on the walls of the fume hood during synthesis. The material was dissolved in a minimum of de-ionized water and filtered through a 0.45 μm syringe filter to remove any particulates. Optical emission lines corresponding to the elements in the 3-layer Aurivillius structure $Bi_2Sr_2Nb_2TiO_{12}$ were investiaged. De-ionized water was run as the background scan. Five scans were taken of the matrix and the sample. A student's t-test was then performed for each element to determine if there was a significant difference between the intensities of the optical emission lines in the sample and the matrix.

2.1.2.4 X-ray diffraction (XRD)

A Philips12045 X-ray diffractometer with an accelerating potential of 40 kV and 20 mA of current was utilized to generate the x-ray diffraction patterns of $Bi_{1-y}Pb_ySr_2Nb_2Ti_{1-x}Al_xO_{12-\delta}$ (y = 0 and 0.4) ($0.0 \leq x \leq 0.8$) with Cu-K_α radiation from 10° to 70° 2-θ. Powder samples were loaded into aluminum side-drifted holders. The room temperature measurements were completed at a 0.03 θ step size with a 3 second count time. Phase analysis of the diffraction data was completed with Jade6.0[52] software. Lattice parameter determinations were calculated with least squares cell refinement in Jade software. The PDF[49] was used in the identification of the present phases.

2.1.2.5 High Temperature X-ray Diffraction (HTXRD)

A Siemans diffractometer and stainless steel furnace set to 40 kV of accelerating potential and 20 mA of current was utilized to generate high temperature x-ray diffraction (HTXRD) patterns of $Bi_2Sr_2Nb_2TiO_{12}$ with Co-K_α radiation. The data was collected between 500°C and 800°C in 50°C intervals from 10° to 70° with a position sensitive detector (Mbraun). Samples were loaded onto alumina plates, which were then heated with platinum heating elements.

2.1.3 Microstructural Characterization

An Amray 1810 scanning electron microscope equipped with secondary electron and backscattered electron detectors was utilized for microstructural characterization of the sintered powders. Pellets of the reacted powders were pressed on a Carver press in a ½ inch die at 34.5 MPa with a hold time of one minute. Each sample was prepared in a vacuum impregnated epoxy mount and allowed to cure for 24 hours. Polishing followed from 400-grit grinding paper down to one micron sized diamond paste. The samples were individually cleaned in an ultrasonicator between each polishing step. A 60:40 Au:Pd conductive layer was sputter coated onto the samples.

Images were taken at increasing magnifications of 1000X, 2000X and 3000X with an accelerating potential of 20 kV. Grain boundary characterization was carried out under secondary electron imaging. Backscattered electron detection then followed to determine the presence of multiple phases in each composition. Elemental analysis of the secondary and major phases was obtained with an EVEX EDS system on a Phillips 515 electron microscope.

2.1.4 Impedance Spectroscopy

Two-point AC impedance spectroscopy data was obtained using a system that included a Solartron 1260 impedance/gain analyzer and a Centurion Qex furnace. Data was collected at 50-degree intervals from 473 K to 1123 K on ½ inch sintered pellets pressed to 34.5 MPa and coated with platinum ink. The frequency was swept from 5 Hz to 5 MHz and 100 data points were collected in the range. Measurements were made from low to high frequency. Cole-Cole plots were generated from the impedance data at each temperature interval. One full arc combing both grain boundary and bulk properties was obtained at the high frequency end of the plot as well as the beginning of a second arc at low frequency resulting from electrode effects. The conductivity in S/cm can thus be determined for each composition from the equation:[11]

$$\sigma(T) = A * \exp\left(\frac{-E_a}{RT}\right) \quad (11)$$

where T is the temperature in Kelvin, A is a constant and E_a is the activation energy. The diameter of the first arc was utilized as the impedance of the sample (Z') combining both bulk and grain boundary effects. A second arc occurring at low frequency was ignored as an electrode effect. The conductivity of each composition at a given temperature was thus determined from the Cole-Cole plots and the physical dimensions of each pellet. Confirmatory DC measurements were made from 1123 K to 670 K and compared to the AC impedance data to check for accuracy and electrode effects.

2.2 $La_{1-x}Sr_xCoO_3$ Specimens

2.2.1 Synthesis

The polymerized complex method as detailed above was used to synthesize all $La_{1-x}Sr_xCoO_3$ samples in the range $0.1 \leq x \leq 0.9$. The starting powders consisted of $La(NO_3)_3 \bullet 6H_2O$ (Alfa-Aesar, 99.9%), $Co(NO_3)_2 \bullet 6H_2O$ (Alfa-Aesar, 98%), and $Sr(NO_3)_2$ (Alfa-Aesar, 98%). All of the precursors were soluble in deionized water. Table II-2 details the masses of the precursors utilized to produce the final compositions. The organics were burned off at 500°C in air in a Pyrex beaker for 5 hours and the resulting powder was fired at 1200°C in air for 15 hours in an MgO crucible with a heating and cooling rate of 4°C per minute.

2.2.2 Unit Cell Characterization

The fired $La_{1-x}Sr_xCoO_3$ phases were subject to unit cell indexing and lattice parameter refinement. The samples were ground for 5 minutes in acetone with a mortar and pestle then allowed to dry. The sample powder with composition $0.1 \leq x \leq 0.5$ was then loaded into a side-drifted sample holder. There was insufficient powder of compositions $0.6 \leq x \leq 0.9$ to fully load a side-drifted holder; as a result these specimens were applied to a zero background holder.

Table II-2. Masses of the Precursor Powder in Grams for the Composition $La_{1-x}Sr_xCoO_3$.

Composition	Mass (g) $La(NO_3)_3 6H_2O$	Mass (g) $Co(NO_3)_2 6H_2O$	Mass (g) $Sr(NO_3)_2$
x = 0.1	4.6765	3.4924	0.2540
x = 0.2	4.1569	3.4924	0.5079
x = 0.3	3.6373	3.4924	0.7619
x = 0.4	3.1177	3.4924	1.0158
x = 0.5	2.5981	3.4924	1.2698
x = 0.6	2.0785	3.4924	1.5238
x = 0.7	1.5589	3.4924	1.7778
x = 0.8	1.0393	3.4924	2.0318
x = 0.9	0.5197	3.4924	2.2858

A Siemens D500 diffractometer set to 40 kV and 30 mA with Cu K_α radiation was utilized to generate the x-ray diffraction patterns from 20° to 150° 2-θ. A graphite diffracted-beam monochromator was used with 1° divergence and 0.05° receiving slits. The measurements were completed at 23°C ± 2°C using a step size of 0.02° and a count time of 8 seconds. Rietveld refinement was then completed with Topas[53] software. A LaB_6 standard was used to define the instrument parameters and obtain fundamental parameter profiles. The fundamental parameters were applied to the $La_{1-x}Sr_xCoO_3$ peaks in the Rietveld refinement.

The reference intensity ratio to corundum (I/I_C) was obtained by mixing 50/50 weight fractions of sample and National Institute of Standards and Technology (NIST) SRM 676 alumina powder in an aluminum side-drifted holder. Mixing was done with a mortar and pestle for 5 minutes. Measurements were made on a Phillips 12045 x-ray diffractometer with Cu K_α radiation set to 40 kV of accelerating potential and 20 mA of current from 31° to 35° 2-θ and 42.5° to 46.5° 2-θ with a step size of 0.02-θ and a count time of 5 seconds. The ratio for each composition was made in triplicate by unpacking and reloading the sample holder prior to making another measurement. The average of three was calculated as the I/I_C value.

3. Results and Discussion

3.1 Solution Chemistry

3.1.1 Infrared Spectroscopy (FT-IR)

Infrared spectra were collected at room temperature for the $Bi_2Sr_2Nb_2TiO_{12}$ composition while in solution with citric acid and ethylene glycol. Samples were taken from solution at the temperatures 85°C, 115°C, 135°C and 170°C then allowed to cool to room temperature prior to data acquisition. The data was compared for a solution with the pH raised to 3.00 by the addition of ammonium hydroxide and for an unaltered solution. Figure 3.1 shows an overlay of the infra-red spectra for the unaltered solution at 85°C, 115°C, and 135°C. The viscosity of the solution gradually increased with temperature. The universal absorption at 2900 cm^{-1} is due to aliphatic carbon-hydrogen bonding. The resonant absorption at approximately 3300-3400 cm^{-1} results from unreacted hydroxyl groups on ethylene glycol and citric acid.[54] The carbonyl peak is located at 1735 cm^{-1}, which is indicative of carboxylic acid groups.[54]

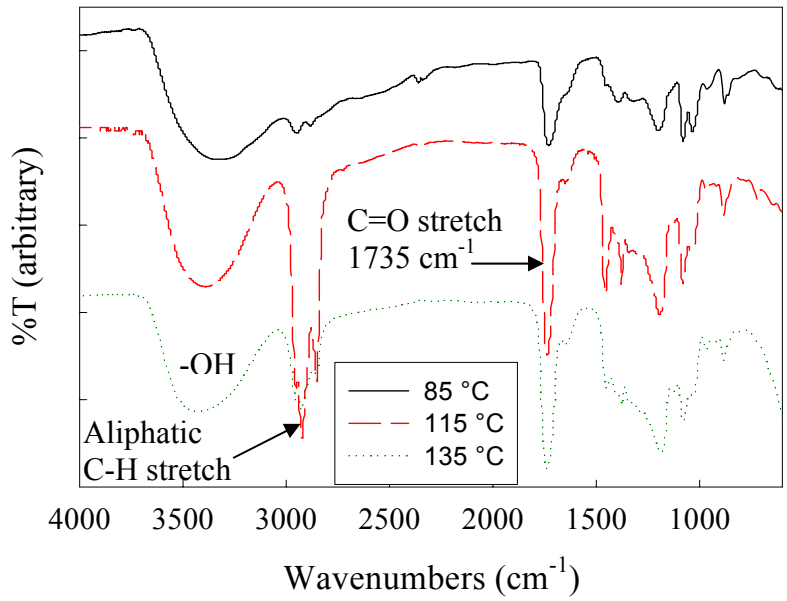

Figure 3.1. Infrared spectra of the reaction mixture measured in transmission after heating to 85°C, 115°C and 135°C.

Figure 3.2 shows the attenuated total reflectance (ATR) infrared spectrum of the fully polymerized product after heating in a drying oven at 170°C for eight hours then cooling to room temperature. A solid amorphous gel was produced upon completion of the reaction. The carbonyl absorption has shifted from 1735 cm^{-1} to 1715 cm^{-1} showing the completed reaction of the carboxylic acid and hydroxyl groups to form an ester.[54] In addition, the absence of a significant peak at 3300 cm^{-1} exhibits the lack of hydroxyl functional groups left on ethylene glycol.

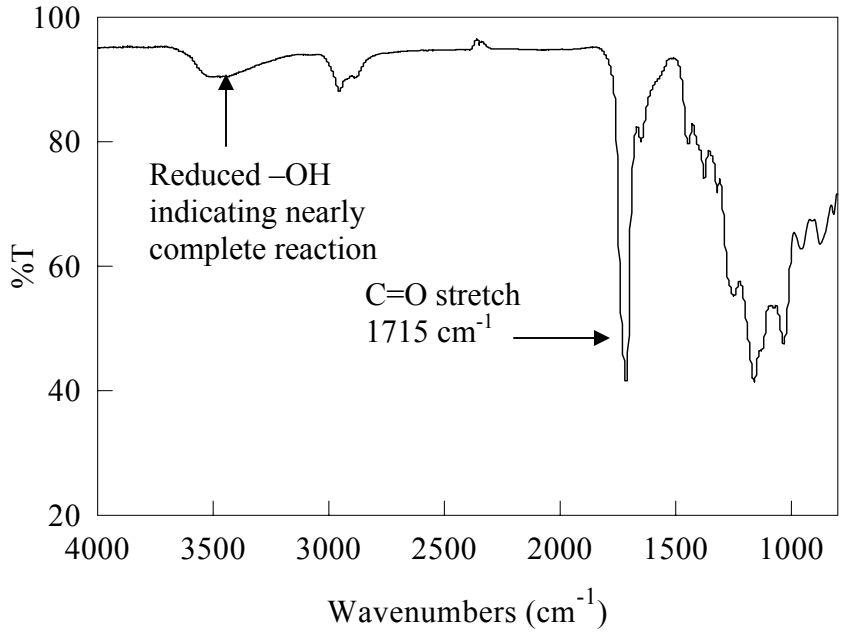

Figure 3.2. Infrared spectrum of the reaction mixture after the completed reaction at 170°C measured using attenuated total reflectance.

Infrared spectra were also collected for the $Bi_2Sr_2Nb_2TiO_{12}$ composition while in solution with citric acid and ethylene glycol when the pH was raised to 3.00 by the addition of ammonium hydroxide. The reaction is characterized by a color change from clear to black upon heating to 100°C, eventually becoming a highly viscous tar like substance at 135°C. After completion of the reaction at 170°C for eight hours a hard black amorphous gel was produced, which was dissolved in deionized water to obtain an infrared transmission spectrum as shown in Figure 3.3. A peak at 1642 cm^{-1} in addition to the ester peak is present in the data. The peak at 1642 cm^{-1} is attributed to the formation of an amide[54] resulting from the reaction of the nitrogen in ammonium hydroxide with a carbonyl carbon in citric acid as detailed in Figure 3.4. The peak at 3400 cm^{-1} is due to the presence of water as a solvent.

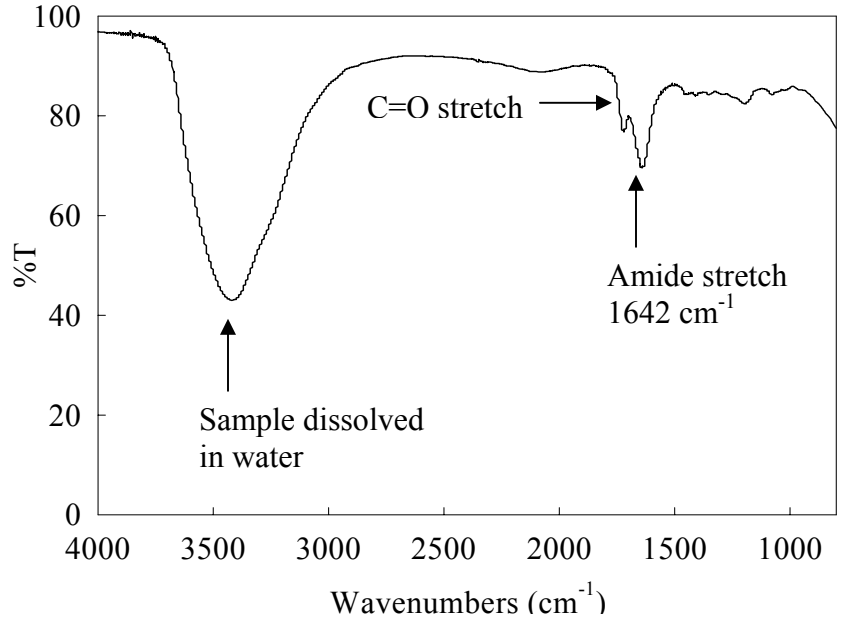

Figure 3.3. Infrared spectrum for a solution with the pH raised to 3.00 by the addition of ammonium hydroxide.

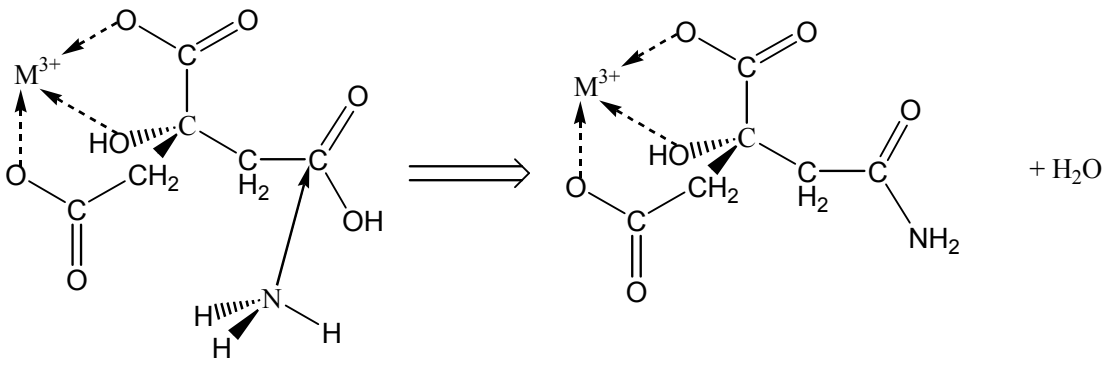

Figure 3.4. A schematic of the reaction of ammonium with citric acid shows the formation of an amide.

Infrared spectroscopy results indicate the formation of an ester from citric acid and ethylene glycol after polymerization has occurred. Furthermore, ammonium hydroxide will undergo nucleophilic substitution with citric acid to form an amide.

3.1.2 Nuclear Magnetic Resonance (FT-NMR)

Room temperature (RT) H^1 NMR spectra were collected for the $Bi_2Sr_2Nb_2TiO_{12}$ composition while in solution with citric acid and ethylene glycol. Samples were drawn from solution at the temperatures 100°C, 115°C, and 135°C and cooled to RT. NMR spectra were also collected at RT for samples of citric acid and ethylene glycol without metal cations drawn at 100°C and 135°C for comparison. All of the data was referenced to 3-(trimethylsilyl)-1-propane sulfonic acid sodium salt (DSS). Figures 3.5 and 3.6 show the proton NMR spectrum for citric acid and ethylene glycol after heating to 100°C and 135°C. The chemical shift at 5.046 ppm is due to the four hydrogens in the ethyl group (–CH_2-CH_2-) in ethylene glycol.[54] The two peaks at 2.924 and 2.970 ppm result from the two –CH_2- groups in citric acid.[54] Hydroxyl groups are causing the singlet at 3.657 ppm.[54] The growth of multiple peaks is evident, centered at 4 ppm. The peak at 5.046 ppm, which has shifted to 4.697 ppm, can be attributed to the formation of an ester. The pair of hydroxyl groups on ethylene glycol that were causing the previous shift of 5.046 ppm have been replaced with an ester. As a result, the protons in (–CH_2-CH_2-) are not shifted as strongly down field.

PEAKLIST

LINE	POINT	HZ	PPM	INTENSITY	REL_INT	LABEL
1	4603	302.84	5.046	209339	101.033	1
2	5286	219.43	3.657	104149	50.265	2
3	5623	178.23	2.970	5630	2.717	3
4	5646	175.49	2.924	6391	3.084	4
5	7084	-0.15	-0.002	2007	0.969	5

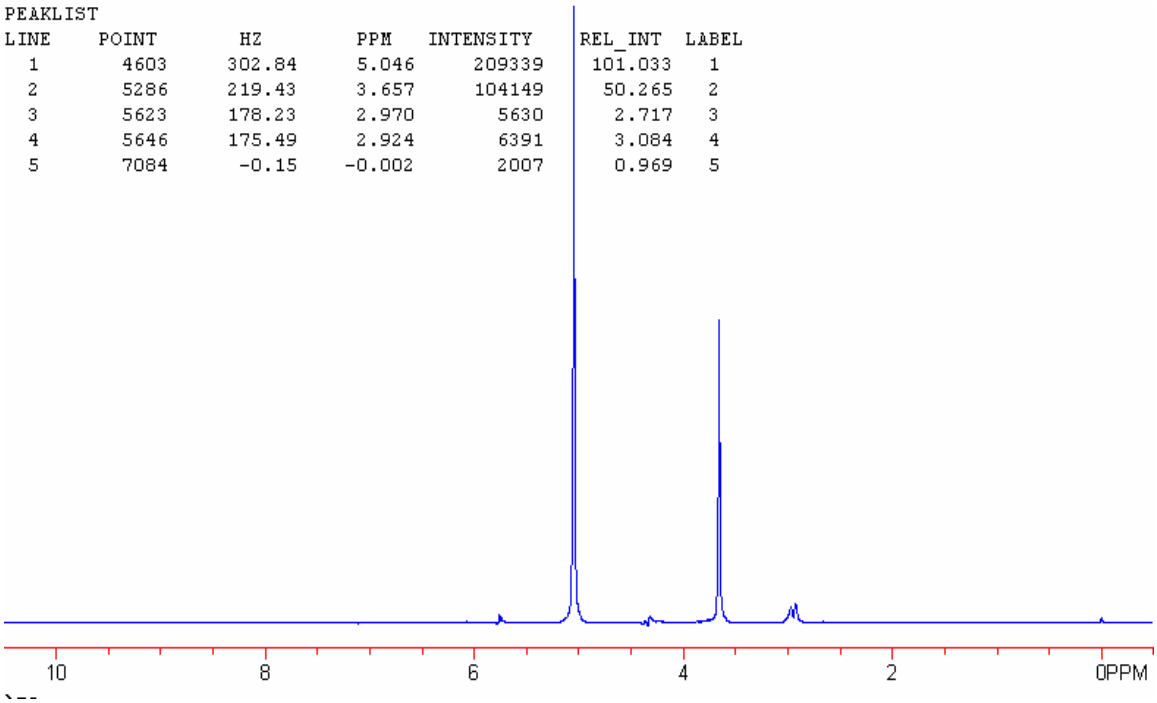

Figure 3.5. Room temperature proton NMR spectrum of the citric acid-ethylene glycol mixture after heating to 100°C.

PEAKLIST

LINE	POINT	HZ	PPM	INTENSITY	REL_INT	LABEL
1	4489	281.85	4.697	114092	98.863	1
2	4720	253.61	4.226	6846	5.932	2
3	5002	219.14	3.652	44722	38.752	3
4	5327	179.52	2.991	8953	7.758	4
5	6797	-0.00	-0.000	16510	14.306	5

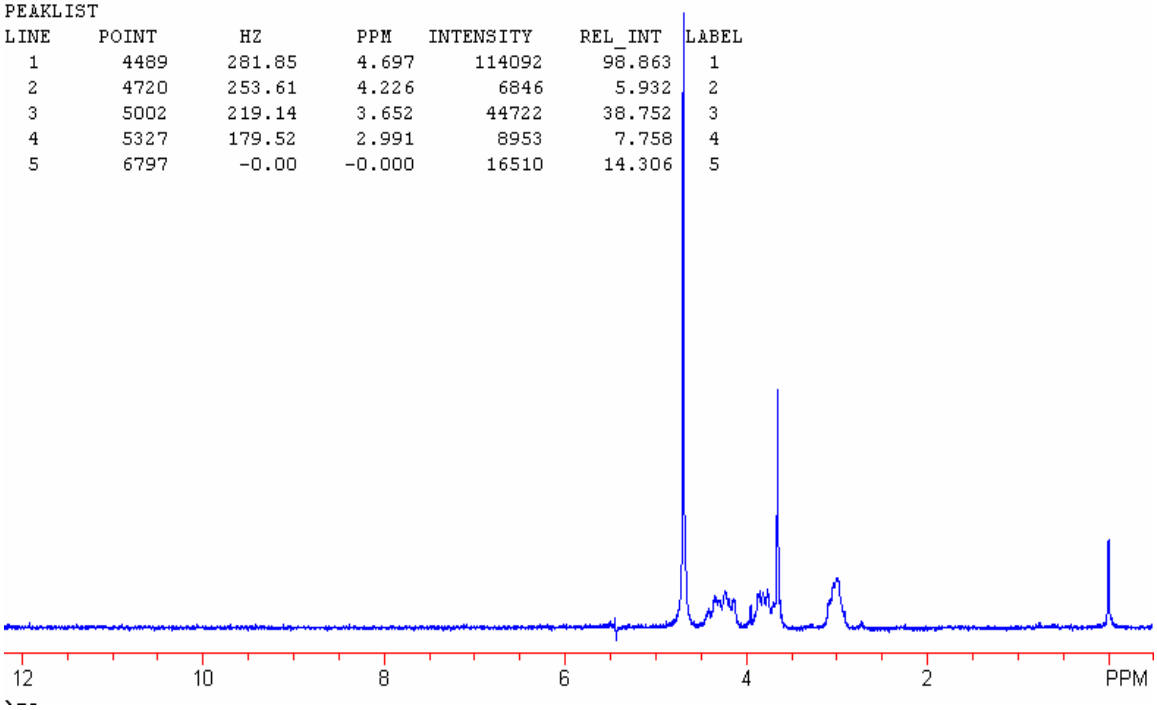

Figure 3.6. Room temperature proton NMR spectrum of the citric acid-ethylene glycol mixture after heating to 135°C.

Figure 3.7 shows the proton NMR spectrum acquired at room temperature of Bi-Sr-Nb-Ti ions in solution with citric acid and ethylene glycol after heating to 100°C. Several of the same features are evident in Figures 3.5 and 3.7. The hydroxyl peaks are present at 4.232 ppm, as well as the shift at 5.390 ppm from the ethyl group. The two shifts associated with citric acid at approximately 3 ppm have blended into what appears to be a single broad peak. Figures 3.8 and 3.9 show the proton NMR spectra acquired at room temperature of Bi-Sr-Nb-Ti ions in solution with citric acid and ethylene glycol after heating to 115°C and 135°C. The singlet at 5.387 ppm has shifted down to 4.722-4.727 ppm. The peak associated with oxygen-hydrogen bonding in ethylene glycol is visibly decreasing with temperature from 100°C to 135°C, due to the substitution reaction that is occurring, resulting in a replacement of the alcohol groups with an ester. There does not appear to be an effect on the spectra stemming from the presence of the cations.

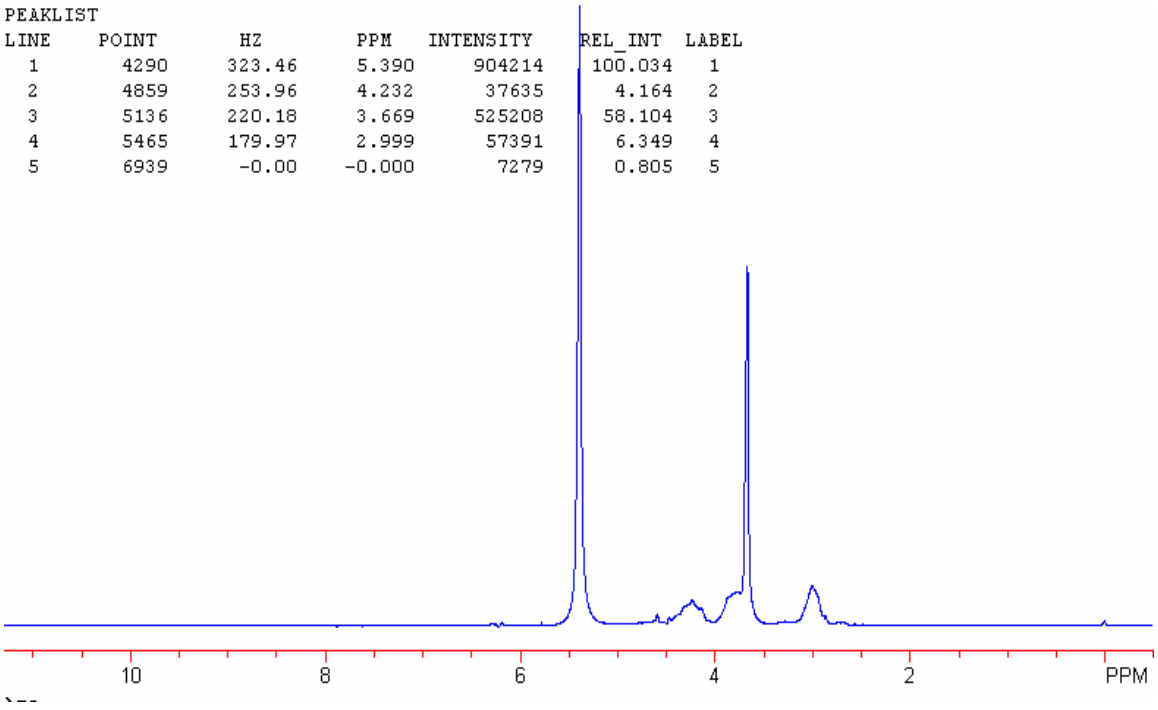

Figure 3.7. Room temperature proton NMR spectrum of the reaction mixture after heating to 100°C.

PEAKLIST

LINE	POINT	HZ	PPM	INTENSITY	REL_INT	LABEL
1	4302	282.31	4.704	37802	103.643	1
2	4540	253.31	4.221	1826	5.006	2
3	4821	218.96	3.649	16443	45.082	3
4	5141	179.85	2.997	2529	6.935	4
5	6615	0.00	0.000	3055	8.376	5

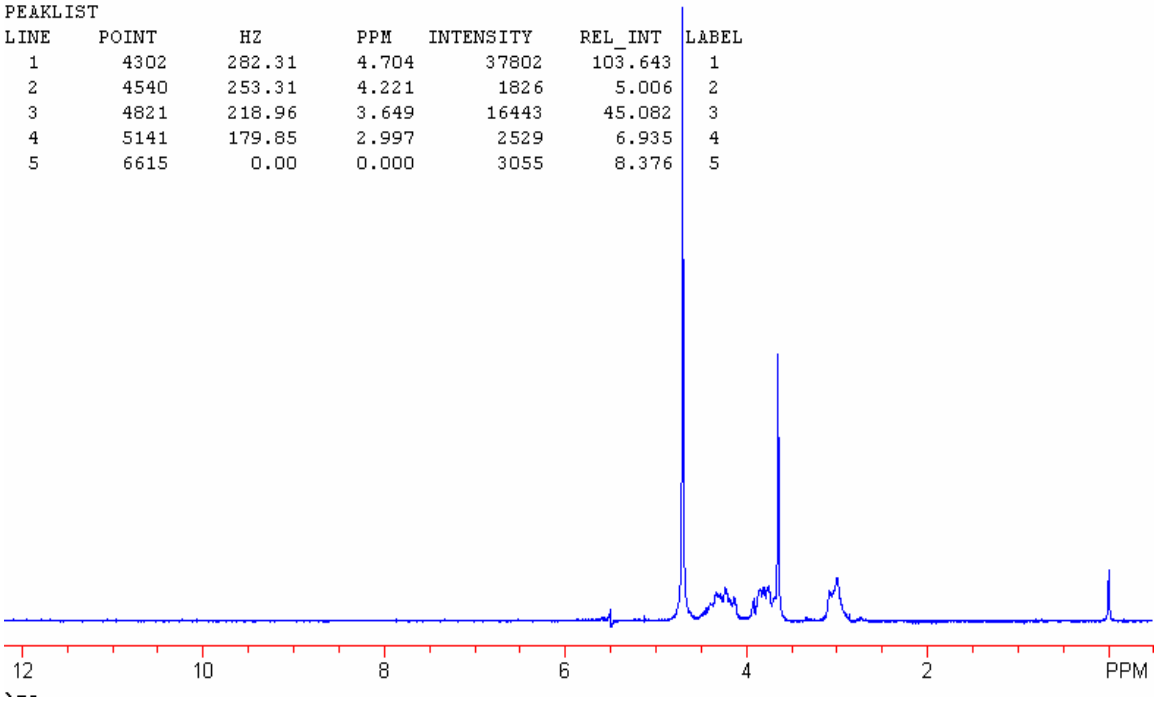

Figure 3.8. Room temperature proton NMR spectrum of the reaction mixuture after heating to 115°C.

PEAKLIST

LINE	POINT	HZ	PPM	INTENSITY	REL_INT	LABEL
1	4387	283.66	4.727	23824	100.114	1
2	4581	260.03	4.333	2316	9.732	2
3	4917	218.96	3.649	7140	30.003	3
4	5234	180.30	3.005	2604	10.942	4
5	6711	-0.00	-0.000	2520	10.588	5

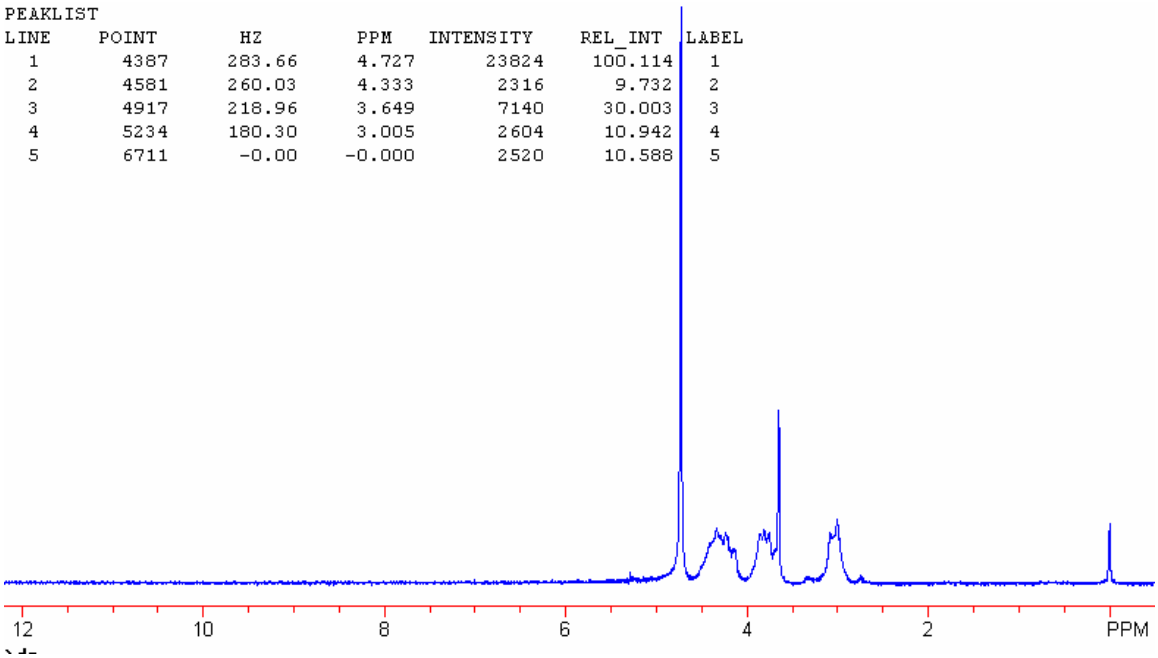

Figure 3.9. Room temperature proton NMR spectrum of the reaction mixture after heating to 135°C.

Figure 3.10 shows the proton NMR spectrum acquired at room temperature for a solution of Bi-Sr-Nb-Ti ions with citric acid and ethylene glycol after heating to 135°C where the pH has been raised to 3.00 by the addition of ammonium hydroxide. The apparent peak at 5.595 ppm is a spinning side band. There appears to be a separate distinct peak at approximately 4.5 ppm not present in solutions that do not contain NH_3OH. The IR data presented in section ***3.1.1*** demonstrated the formation of an amide with the addition of ammonium hydroxide. The peak at 4.5 ppm might be ascribed to hydrogen bonded to nitrogen as part of an amide.

Through the NMR spectra it is possible to track what is occurring with the organic reaction of citric acid and ethylene glycol. At this point, however, it is not possible to comment on the chelation of the individual cations by the polymer. The H^1 spectra and IR data do not indicate how the ions are behaving in solution.

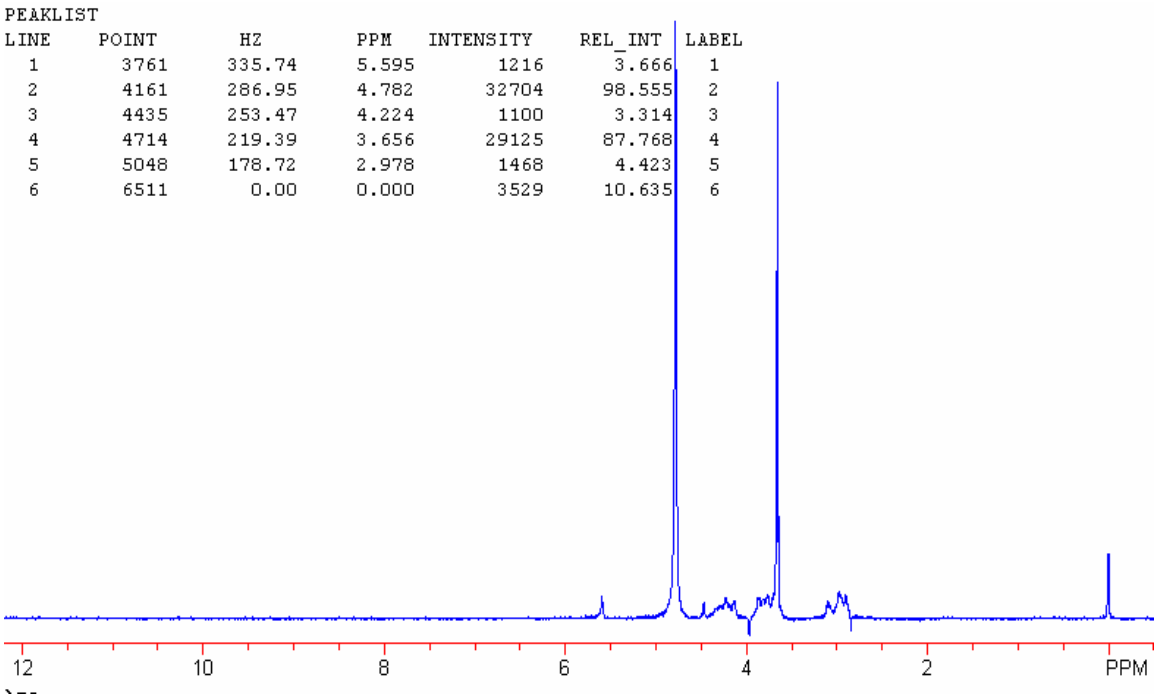

Figure 3.10. Room temperature Proton NMR spectrum of the reaction mixture after heating to 135°C, where the pH has been raised to 3.00 from the addition of ammonium hydroxide.

Infrared spectra of the pre-polymerized solutions show the presence of alcohol functional groups as well as carboxylic acid carbonyl groups at 3300 cm^{-1} and 1735 cm^{-1} respectively. Upon completion of the reaction however, the carbonyl absorbance band has shifted to 1715 cm^{-1} indicating the formation of an ester. The alcohol band has also decreased in intensity, indicating the reaction of ethylene glycol with citric acid. The infrared spectrum of the polymerized solution with ammonium hydroxide contains an absorbance stretch at 1642 cm^{-1} as well as the ester band, resulting from the additional formation of an amide. The H^1 NMR spectra support the conclusions drawn from IR analysis. Prior to polymerization, the hydrogen peak stemming from the ($-CH_2-CH_2-$) group on ethylene glycol is at approximately 5.300 ppm, as a result of the magnitude of the chemical shift caused by the hydroxyl groups. After the reaction between ethylene glycol and citric acid has occurred, the peak moves to approximately 4.700 ppm indicating the formation of an ester. Furthermore, the alcohol peak at 4.300 ppm is also decreasing as the reaction progresses. At this point, however, it is not possible to comment on the chelation of the individual cations by the polymer. The H^1 spectra and IR data do not indicate how the ions are behaving in solution.

3.1.3 Inductively Coupled Plasma – Optical Emission (ICP-OES)

Solvent was condensing on the walls of the fume hood during heating of the solutions. Qualitative elemental analysis was made on the condensed material using inductively coupled plasma (ICP-OES) spectroscopy. The sample was dissolved in de-ionized water. The elements in the 3-layer Aurivillius structure $Bi_2Sr_2Nb_2TiO_{12}$ were investigated. Their corresponding optical emission lines are summarized in Table III-1.

Table III-1. The Optical Emission Lines for the Cations in Composition $Bi_2Sr_2Nb_2TiO_{12}$.

Cation	Line (nm)
Ti	334.941
Sr	421.552
Bi	306.772
Nb	309.418

De-ionized water was run as the background measurement. Five measurements were first made on the background and then on the sample. A student's t-test with a 95% confidence interval was then performed between each element and the matrix to determine if there was a significant difference. A t-test is capable of determining if there is a significant difference between two sets of measurements.[1] The test was conducted assuming unequal variances between the means. The results of the t-test are summarized in table III-2.

Table III-2. Student's t-test Results for the ICP-OES Data Collected for Composition $Bi_2Sr_2Nb_2TiO_{12}$.

Cation	t-critical	t-statistic
Ti	2.02	12.94
Sr	1.94	247.10
Bi	1.94	10.03
Nb	2.02	2.30

The t-critical is determined from the degrees of freedom (n-1) where n = the number of measurements and the desired confidence interval. The t-statistic is a measurement of the difference between the two sets of replicate measurements, in this case assuming unequal variances, calculated from the equation:[1]

$$t_{statistic} = \frac{(\bar{X}_1 - \bar{X}_2)}{S_{pooled} * \left(\frac{n_1 * n_2}{n_1 + n_2}\right)^{\frac{1}{2}}} \tag{12}$$

where $\bar{X}_1$ and $\bar{X}_2$ are the means of the respective sets of measurements, n_1 and n_2 are the number of replicates and S_{pooled} is a pooled standard deviation of both data sets. S_{pooled} is calculated from:[1]

$$S_{pooled} = \left[\frac{S_1^2(n_1 - 1) + S_2^2(n_2 - 1)}{n_1 + n_2 - 2}\right]^{\frac{1}{2}} \tag{13}$$

The t-test results show that there is a significant difference between the sample and the background. It can therefore be concluded with 95% confidence that at least to some degree all of the elements in the $Bi_2Sr_2Nb_2TiO_{12}$ composition are volatilizing out with the solvent. The stoichiometry of the powder that is fired to form the oxide is thus certainly affected.

3.2 X-Ray Diffraction (XRD)

3.2.1 $Bi_2Sr_2Nb_2TiO_{12}$

The composition $Bi_2Sr_2Nb_2TiO_{12}$ was synthesized by the polymerized complex method involving an organo-metallic precursor and heat treated at 900°C in air for 5 hours and again for 15 hours to determine the effect of heating on phase evolution. Heat treatment resulted in the formation of a white powder in the porcelain crucible. Figure 3.11 shows an overlay of the XRD patterns for $Bi_2Sr_2Nb_2TiO_{12}$ heat treated at the above mentioned temperatures with the $SrBi_3NbTi_2O_{12}$ stick pattern (PDF #49-1589). The collected data closely matches the PDF card for a corresponding 3-layer Aurivillius phase with some differences. Several of the peaks are either very broad or poorly resolved. Broad peaks are due to stacking faults or small particle size. After the second firing there is evidence of some of the peaks becoming better defined while increasing in relative height. All the peaks can, however, be accounted for in terms of the Aurivillius phase. As such it can be concluded that this is a phase pure specimen that perhaps contains stacking faults that have not been annealed out in such a short firing cycle, or small crystallite sizes.

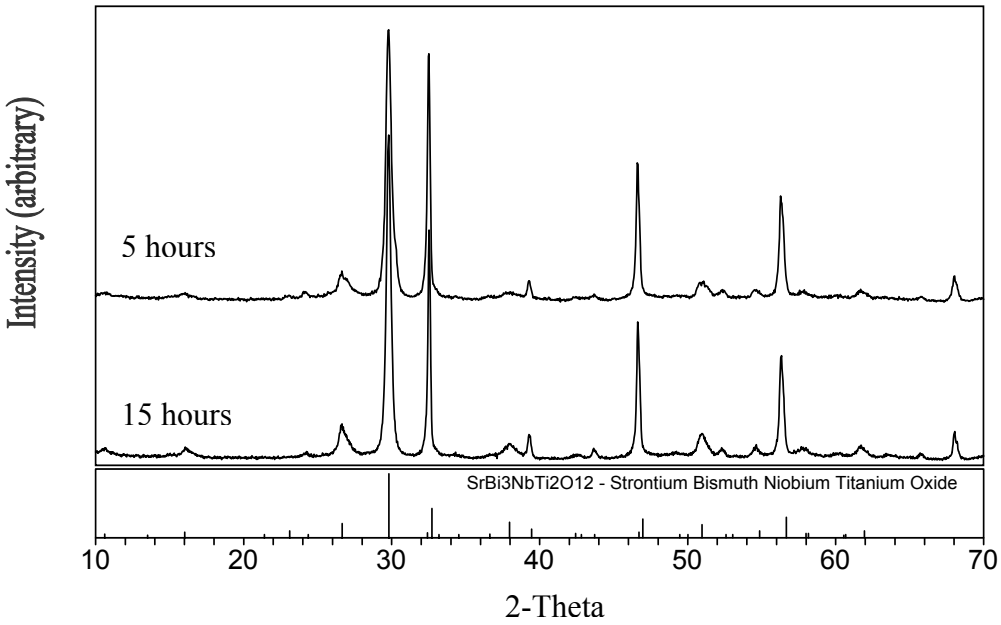

Figure 3.11. XRD measurements with Cu radiation of $Bi_2Sr_2Nb_2TiO_{12}$ fired at 900°C for 5 hours and 15 hours.

The Aurivillius phase $Bi_2Sr_2Nb_2TiO_{12}$ was also synthesized in solutions where the pH was adjusted to 3.00, 6.00 and 9.00 through the addition of ammonium hydroxide. Raising the pH of the solution will remove hydrogen from the carboxylic acids on the chelating agent. By placing a negative charge on the chelating functional groups there should be a stronger attraction with the metal cations in solution. Improving chelation will, perhaps, then reduce the necessary firing temperature by improving the pre-fired properties of the powder after organic burn-off. Figure 3.12 shows an overlay of the x-ray diffraction patterns for $Bi_2Sr_2Nb_2TiO_{12}$ synthesized in solutions of pH 3.00, 6.00 and 9.00 and fired to 700°C in air for 5 hours. A phase pure Aurivillius structure begins to form for the pH = 9.00 sample with a firing temperature as low as 700°C. When the pH equals 3.00 unreacted phases are present in addition to the Aurivillius phase. At a pH level of 6.00, the multiple phases have disappeared and there is poor formation of the Aurivillius structure. The solution with pH = 9.00 produces the best peak resolution. Firing times and temperatures as low as 700°C for 5 hours marks a significant

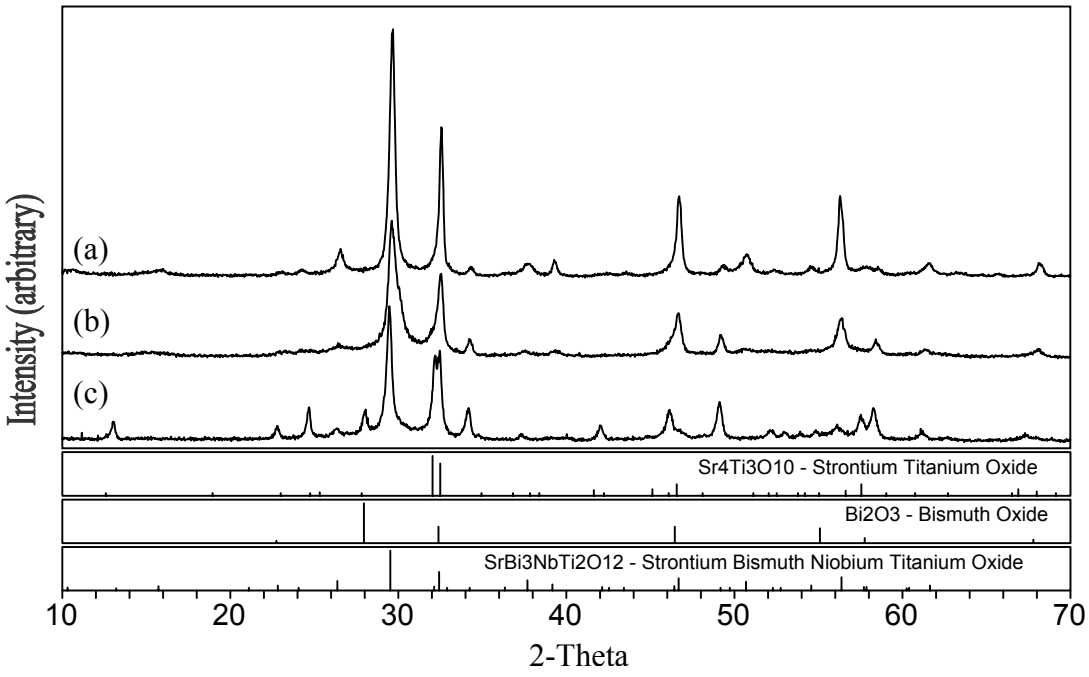

Figure 3.12. XRD measurements with Cu radiation of $Bi_2Sr_2Nb_2TiO_{12}$ fired at 700°C in air for 5 hours with solution pH levels of (a) 9.00, (b) 6.00 and (c) 3.00.

improvement over solid-state synthesis where 50 hours of heat treatment is often necessary at temperatures greater than 1000°C[11,17].

Figure 3.13 shows the $Bi_2Sr_2Nb_2TiO_{12}$ composition produced in pH = 9.00 solution. It is evident that the Aurivillius crystal structure is formed after firing to 700°C. What is interesting to note is how little the x-ray diffraction patterns change after firing to increased temperatures. There appears to be little benefit in increasing the heat treatment temperature. The ability to produce mixed cation oxides at temperatures less than 800°C can have significant advantages. As discussed in experimental Section *2.1.1* when making composition $Bi_{1.6}Pb_{1.6}Sr_2Nb_2Ti_{1-x}Al_xO_{12-\delta}$ it was necessary to use a sacrificial powder bed to prevent lead loss when heating to 900°C. In addition to the energy savings associated with lower processing temperatures it would be a benefit to materials savings if it was no longer necessary to use sacrificial powder when working with lead or any other substance that might volatilize above 700°C.

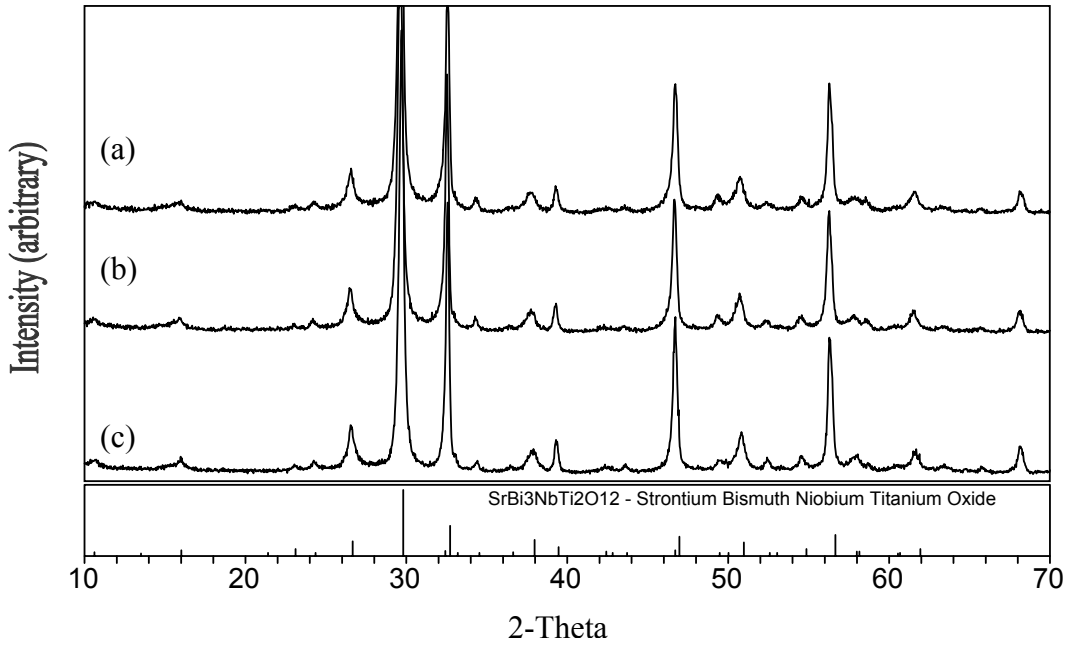

Figure 3.13. XRD measurements with Cu radiation of $Bi_2Sr_2Nb_2TiO_{12}$ synthesized in a solution pH of 9.00 and fired at (a) 700°C (b) 800°C and (c) 900°C in air for 5 hours.

3.2.1.1 High Temperature XRD (HTXRD) of $Bi_2Sr_2Nb_2TiO_{12}$

The composition $Bi_2Sr_2Nb_2TiO_{12}$ yielded yellow-white powders after organic burn-off at 500°C in air for 5 hours. HTXRD data was obtained for powders heat treated to 500°C and containing Bi-Sr-Nb-Ti stoichiometrically mixed to form the $Bi_2Sr_2Nb_2TiO_{12}$ oxide after firing to 900°C. HTXRD patterns were acquired from 10° to 70° 2-θ between 500°C and 800°C with Co-K_α radiation for a solution where NH_3OH had been added to raise the pH to 3.00 and for a solution without NH_3OH addition. Figure 3.14 shows the HTXRD measurement for $Bi_2Sr_2Nb_2TiO_{12}$ attained for a solution without addition of NH_3OH. Formation of the Aurivillius phase begins at 750°C. The Aurivillius peaks at 34°, 36°, 57° and 68° 2-θ start to become clearly resolved at 750°C and increase in relative intensity to 800°C. In addition, formation of the two peaks at 45° and 46° 2-theta are clearly beginning at 750°C.

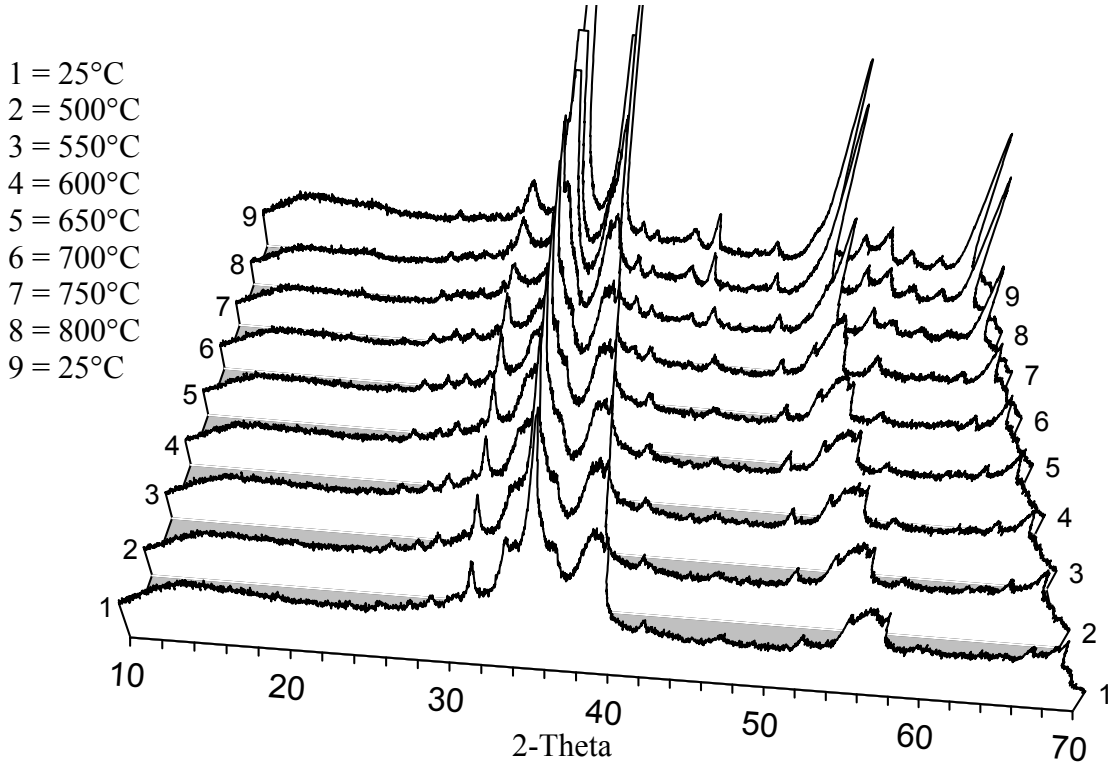

Figure 3.14. HTXRD patterns with Co radiation of $Bi_2Sr_2Nb_2TiO_{12}$ from 500°C to 800°C.

Figure 3.15 shows the HTXRD patterns for $Bi_2Sr_2Nb_2TiO_{12}$ acquired for a solution where the pH was raised to 3.00 by the addition of NH_3OH. Formation of the Aurivillius structure begins at approximately 750°C. The Aurivillius peaks at 57° and 68° 2-theta are clearly resolved at 750°C and the peaks at 45° and 46° 2-θ are beginning to form. Moreover, secondary peaks at 14° and 33° are removed at 750°C as well as a series of five peaks between 63° and 68° 2-θ. The impurity peaks noted above are also present in Figure 3.13, which depicts and x-ray diffraction pattern for $Bi_2Sr_2Nb_2TiO_{12}$ heat treated to 700°C, where the solution pH was 3.00. Interestingly, the phase causing the diffraction of those peaks is not present for the system that did not contain NH_3OH or for the systems where the pH was raised above 3.00 to 6.00 and 9.00. The HTXRD data shows the removal of the phase at 750°C. There does not appear to be a significant difference between Figures 3.14 and 3.15 as to where formation of the Aurivillius structure is beginning. In order to derive the benefits of reduced firing temperature by increasing the solution pH it is evident that the pH level must be above 3.00.

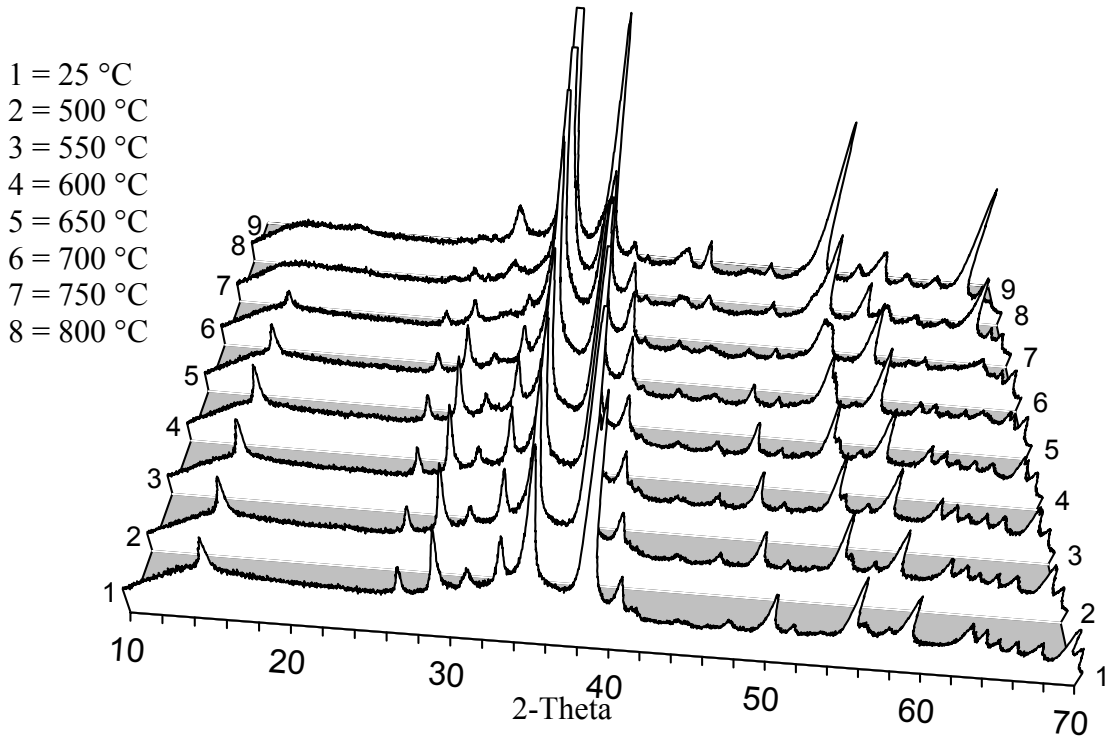

Figure 3.15. HTXRD patterns from 500 °C to 800 °C with Co radiation of $Bi_2Sr_2Nb_2TiO_{12}$ synthesized in a solution pH of 9.00.

3.2.2 $Bi_{1.6}Pb_{0.4}Sr_2Nb_2Ti_{1-x}Al_xO_{12-\delta}$ ($0.0 \leq x \leq 0.8$)

3.2.2.1 Phase Analysis

The composition $Bi_{1.6}Pb_{0.4}Sr_2Nb_2Ti_{1-x}Al_xO_{12-\delta}$ where $0.0 \leq x \leq 0.8$ was synthesized by the polymerized complex method and heat-treated at 900°C in air for 5 hours. In contrast to $Bi_2Sr_2Nb_2TiO_{12}$, $Bi_{1.6}Pb_{0.4}Sr_2Nb_2Ti_{1-x}Al_xO_{12-\delta}$ formed white powders at $x \leq 0.2$ and yellow colored products at $x \geq 0.4$. Figure 3.16 shows an overlay of the $Bi_{1.6}Pb_{0.4}Sr_2Nb_2Ti_{1-x}Al_xO_{12-\delta}$ compositional range. Phase pure Aurivillius structures are obtained when $x = 0$ and $x = 0.2$. In the $x \leq 0.2$ range all of the peaks present in the diffraction pattern can be assigned to a 3-layer structure similar to $SrBi_3NbTi_2O_{12}$ (PDF # 49-1589). When $x \geq 0.4$, however, two additional phases begin to develop, indicating a substitutional solubility limit in the Aurivillius crystal structure. Data indicating the presence of a solubility limit is supported by the work reported by Modi,[11] as well as Lightfoot[12] and Say.[17] The second and third phases are the result of stabilized δ-bismuth oxide (PDF # 27-0052) and strontium aluminum oxide (PDF # 74-1810) forming.

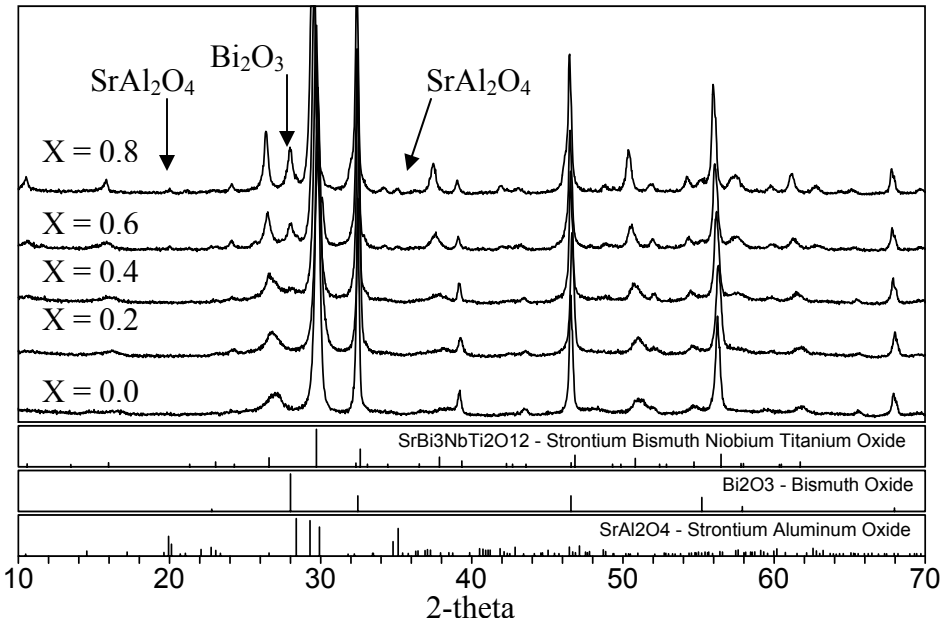

Figure 3.16. XRD measurements with Cu radiation of $Bi_{1.6}Pb_{0.4}Sr_2Nb_2Ti_{1-x}Al_xO_{12-\delta}$ fired at 900°C for 5 hours.

As the aluminum content increases past 0.4, the peaks corresponding to bismuth oxide sharpen and increase in relative intensity. Simultaneously, a third compensating phase attributed to strontium aluminum oxide starts to form in conjunction with the bismuth oxide phase. It is evident from the location of the low angle peaks that as multiple phases begin to develop the actual Aurivillius crystal structure remains 3-layer. In order for this to hold true a third phase must necessarily evolve with bismuth oxide. Due to the smaller atomic scattering factor of the strontium aluminum oxide, the peaks associated with this phase are not as prevalent and are somewhat compressed into the background. Several of the peaks associated with the Aurivillius phase are broad at low levels of x and begin to sharpen at higher levels. The evolution of multiple phases when $x \geq 0.4$ might be attributed to a high strain in the crystal structure at this composition. Since the sharpening of the Aurivillius phase peaks occurs at high aluminum concentration, it is likely that the broader peaks at $x \leq 0.4$ are due to stacking faults that have not been annealed out in such a short firing cycle.

3.2.2.2 Lattice Parameter Refinement

The lattice parameters for $Bi_{1.6}Pb_{0.4}Sr_2Nb_2Ti_{1-x}Al_xO_{12-\delta}$ were refined by a least squares refinement method in Jade6.0. Initial peak positions and hkl planes were obtained from PDF # 49-1589. The room temperature measurements were completed at a 0.03 θ step size with a 3 second count time. Samples were loaded into aluminum side-drifted holders and measured with Cu-K_α radiation from 10° to 70° 2-theta. Figure 3.17 and Figure 3.18 detail the effect of aluminum substitution on the tetragonal lattice parameter along the a and c axes. The a-axis lattice parameter ranged from 0.403(0.013) nm at x = 0.0 to 0.38508(0.00068) nm at x = 0.8. The c-axis lattice parameter ranged from 3.44(0.12) nm at x = 0.0 to 3.3015(.0039) nm at x = 0.8. The lattice parameters decreased with increasing aluminum substitution across the entire compositional range. The effect is non-linear however, with initial substitutional concentrations producing the largest changes. The effective ionic radius of aluminum is 0.54 nm compared to 0.61 nm for titanium. Decreasing lattice parameters with increasing aluminum substitution is expected as a result of the difference in ionic radii.

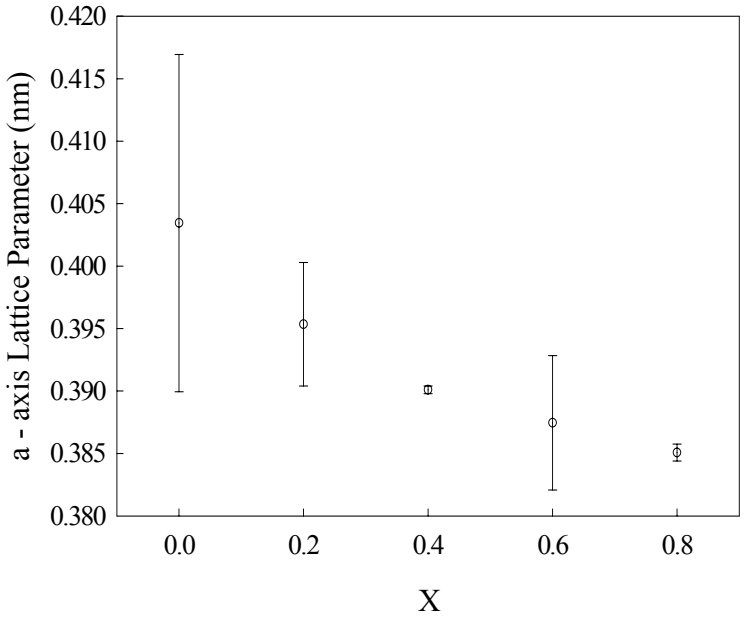

Figure 3.17. The a-axis lattice parameter in nm of $Bi_{1.6}Pb_{0.4}Sr_2Nb_2Ti_{1-x}Al_xO_{12-\delta}$ is plotted for increasing values of x. The error bars represent plus/minus one standard deviation from the cell refinement.

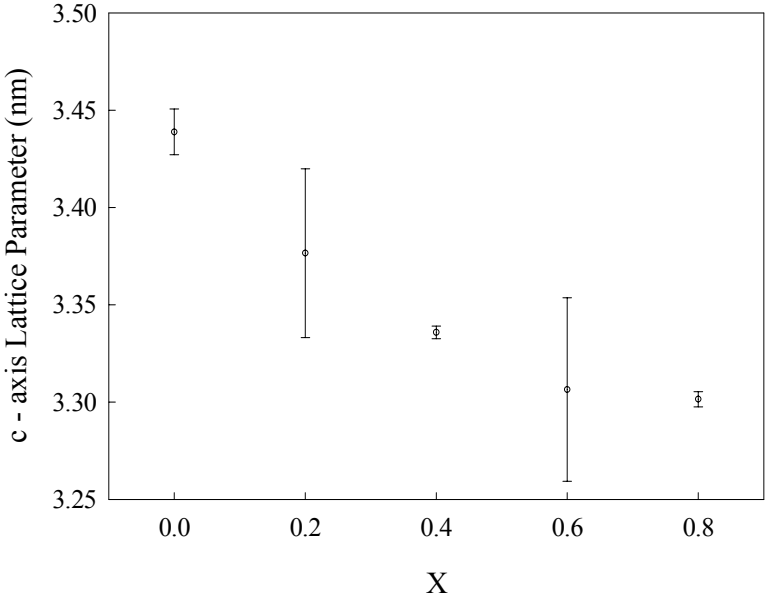

Figure 3.18. The c-axis lattice parameter in nm of $Bi_{1.6}Pb_{0.4}Sr_2Nb_2Ti_{1-x}Al_xO_{12-\delta}$ is plotted for increasing values of x. The error bars represent plus/minus one standard deviation from the cell refinement.

3.3 Electrical Characterization of $Bi_{1.6}Pb_{0.4}Sr_2Nb_2Ti_{1-x}Al_xO_{12-\delta}$ ($0.0 \leq x \leq 0.8$)

AC impedance spectroscopy was carried out on pressed pellets $Bi_{1.6}Pb_{0.4}Sr_2Nb_2Ti_{1-x}Al_xO_{12-\delta}$ sintered to 900°C from 473 K to 1123 K. The data collection was halted at 1123 K to prevent lead loss during testing. Impedance measurements were taken at 50-degree temperature intervals. Figure 3.19 shows an overlay of the Arrhenius conductivity plots for $Bi_{1.6}Pb_{0.4}Sr_2Nb_2Ti_{1-x}Al_xO_{12-\delta}$ and 8% yttria-stabilized zirconia (YSZ). DC conductivity of the x = 0.2 composition is also shown for comparative purposes. There is a general trend in all specimens of increasing conductivity with increasing temperature. The un-substituted $Bi_2Sr_2Nb_2TiO_{12}$ phase has a conductivity of approximately 10^{-5} S/cm at 1123 K. Substitution of lead for bismuth results in an increase in conductivity of 1.5 orders of magnitude at 1123 K. Conductivities at 1123 K ranged from 1.74 x 10^{-4} S•cm^{-1} when x = 0, to 4.6 x 10^{-3} S•cm^{-1} when x = 0.8.

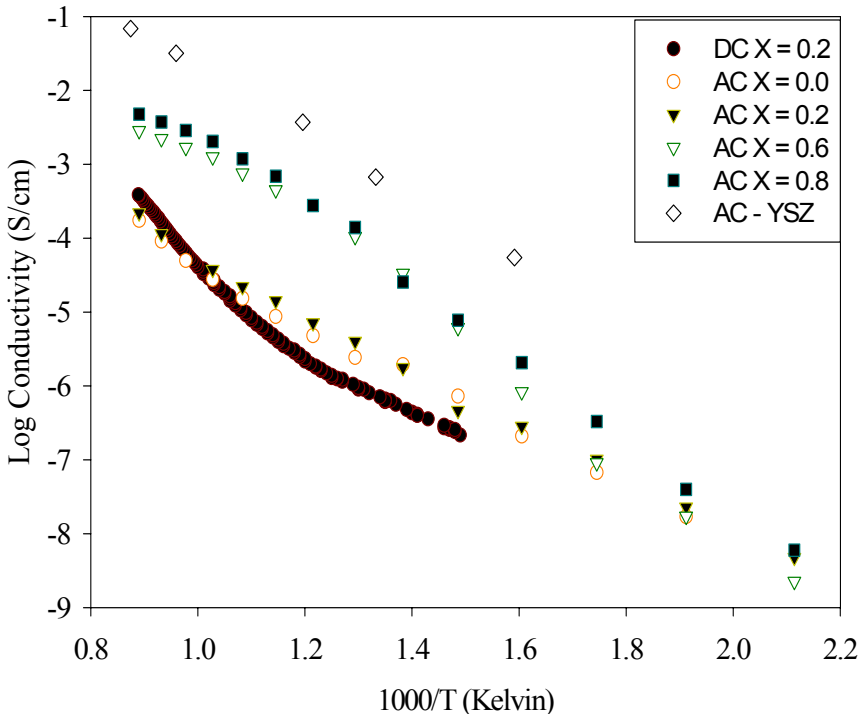

Figure 3.19. Total conductivity of $Bi_{1.6}Pb_{0.4}Sr_2Nb_2Ti_{0.2}Al_{0.8}O_{12-\delta}$ and YSZ[11] from 2-point AC impedance and DC 2-point conductivity between 473 K and 1123 K.

The higher conductivity of specimen of composition $Bi_{1.6}Pb_{0.4}Sr_2Nb_2Ti_{0.2}Al_{0.8}O_{12-\delta}$ is due at least in part to the presence of bismuth oxide, which conducts oxygen ions more readily than does the base Aurivillius structure. Moreover, since x-ray analysis indicates that aluminum is incorporating itself into the structure across the whole substitutional range the number of oxygen vacancies in the Aurivillius phase is also increasing. The jump in conductivity of approximately one order of magnitude between compositions x = 0.2 and x = 0.6 can also be attributed to the formation of bismuth oxide. The x-ray diffraction data indicated the formation of bismuth oxide beginning at x = 0.4. The electrical characterization verifies the effect. As a comparison, yttria-stabilized zirconia exhibits a conductivity around 3.2 x 10^{-2} $S \bullet cm^{-1}$ at 1123K[6], approximately an order of magnitude higher than $Bi_{1.6}Pb_{0.4}Sr_2Nb_2Ti_{0.2}Al_{0.8}O_{12-\delta}$. The activation energies of $Bi_{1.6}Pb_{0.4}Sr_2Nb_2Ti_{1-x}Al_xO_{12-\delta}$ are summarized in table III-3.

Table III-3. Activation Energies for $Bi_{1.6}Pb_{0.4}Sr_2Nb_2Ti_{1-x}Al_xO_{12-\delta}$ and YSZ Calculated from the Slope of the Corresponding Conductivity Plots between 473 K and 1123 K.

Composition	Activation Energy (eV)
X = 0.0	0.74
X = 0.2	0.74
X = 0.6	1.05
X = 0.8	1.01
YSZ	0.86

DC conductivity of the x = 0.2 specimen matches up well with the AC data at high temperatures but begins to drop lower at around 900 K. The change in trend between the AC and DC conductivity at 900 K is due to electrode effects. Figures 3.20 and 3.21 show the cole-cole impedance plots of $Bi_{1.6}Pb_{0.4}Sr_2Nb_2Ti_{0.2}Al_{0.8}O_{12-\delta}$ at 600°C. The plots are typical of the entire temperature range. The semicircular arcs depicted in the graphs represent the real (Z') and imaginary (Z'') impedances in the bulk of the samples. As a result, the intercept at Z' is utilized to determine the real component of the impedance. In specimens of compositions x = 0.6 and x = 0.8 however, after reaching

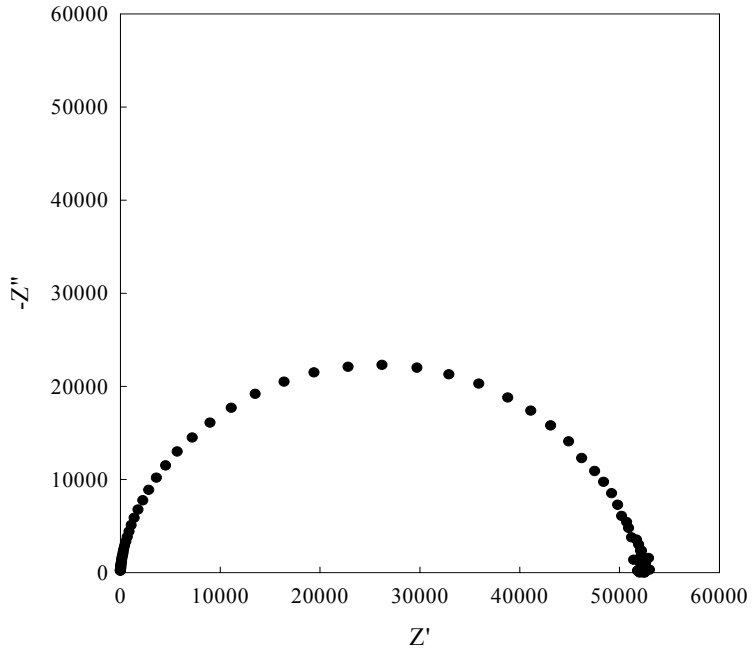

(a)

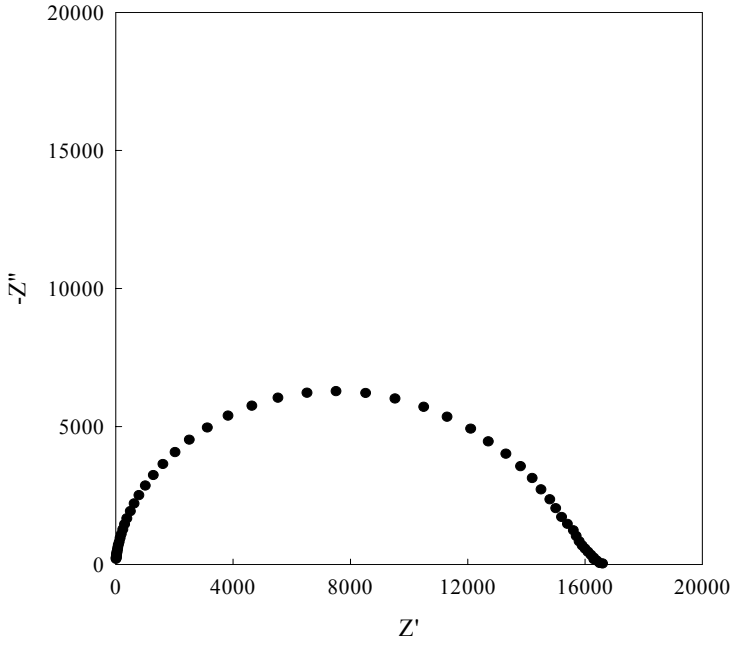

(b)

Figure 3.20. Cole-Cole impedance plots of $Bi_{1.6}Pb_{0.4}Sr_2Nb_2Ti_{1-x}Al_xO_{12-\delta}$ at 600°C for (a) x = 0.0 and (b) x = 0.2.

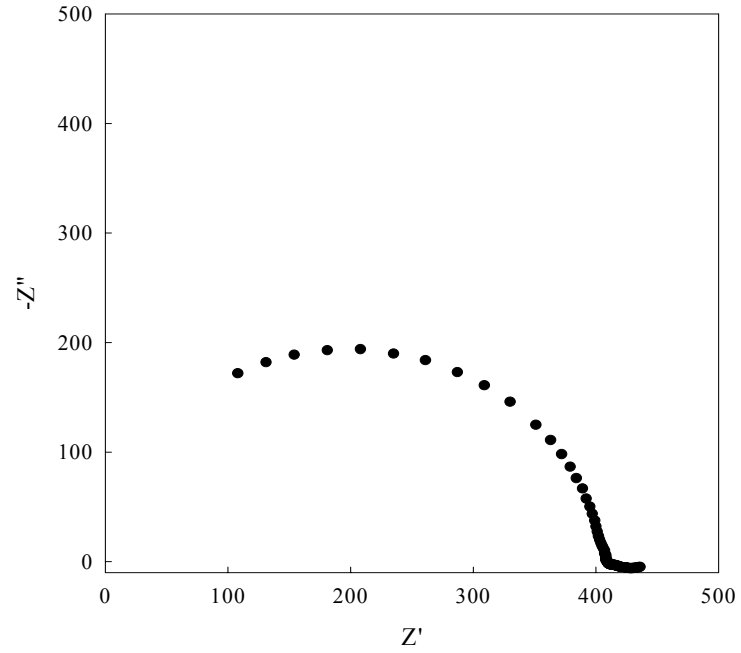

(a)

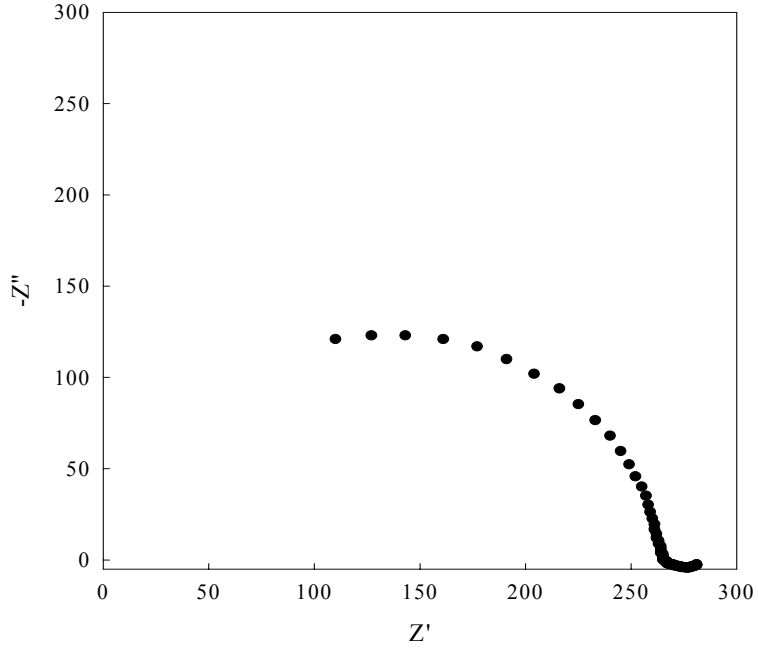

(b)

Figure 3.21. Cole-Cole impedance plots of $Bi_{1.6}Pb_{0.4}Sr_2Nb_2Ti_{1-x}Al_xO_{12-\delta}$ at 600°C for (a) x = 0.6 and (b) x = 0.8.

the Z′ intercept the graphs start the formation of a second arc, which is possibly related to an electrode effect. At lower frequency polarization is induced at the platinum electrodes in the 2-point test apparatus, resulting in an electrode component to the conductivity. It is possible to distinguish between the electrical responses due to grain conduction in the sample and polarization with AC impedance. Under DC measurement however, it is possible for a significant electrode component to occur, but it is not possible to separate the individual contributions to the overall response. As a result, the DC plot at x = 0.2 shows electrode effect occurring by the difference in conductivity with the AC plot at x = 0.2.

3.3.1 $Bi_{1.6}Pb_{0.4}Sr_2Nb_2Ti_{1-x}Al_xO_{12-\delta}$ ($0.0 \leq x \leq 0.8$) Percent Yields

Some loss of material occurred for $Bi_{1.6}Pb_{0.4}Sr_2Nb_2Ti_{1-x}Al_xO_{12-\delta}$ during chemical processing and upon heat treating to 900ºC for 5 hours. The percent yields of each composition are cited in table III-4. Yields were obtained by individually weighing each empty crucible prior to firing and then reweighing after firing. The difference was calculated as the final product mass. The theoretical 100% masses were determined from the batch calculations and are listed in table II-1.

Table III-4. Percent Yields Calculated for $Bi_{1.6}Pb_{0.4}Sr_2Nb_2Ti_{1-x}Al_xO_{12-\delta}$ upon Heat Treatment to 900ºC.

Composition	% Yield
X = 0.0	94.5
X = 0.2	94.1
X = 0.4	93.7
X = 0.6	94.0
X = 0.8	93.3

3.4 Microstructural Characterization of $Bi_{1.6}Pb_{0.4}Sr_2Nb_2Ti_{1-x}Al_xO_{12-\delta}$

3.4.1 Microstructural Analysis of $Bi_{1.6}Pb_{0.4}Sr_2Nb_2TiO_{12-\delta}$

Scanning electron microscope (SEM) images and energy dispersive spectroscopy (EDS) data were acquired for $Bi_{1.6}Pb_{0.4}Sr_2Nb_2TiO_{12-\delta}$. Figure 3.22 shows the SEM micrographs generated for $Bi_{1.6}Pb_{0.4}Sr_2Nb_2TiO_{12-\delta}$ prepared by the polymerized complex method. Samples of composition x = 0.0 show a continuous gray phase with backscattered electron imaging, indicating a single phase specimen. Secondary electrons show some surface roughness and some minor surface porosity.

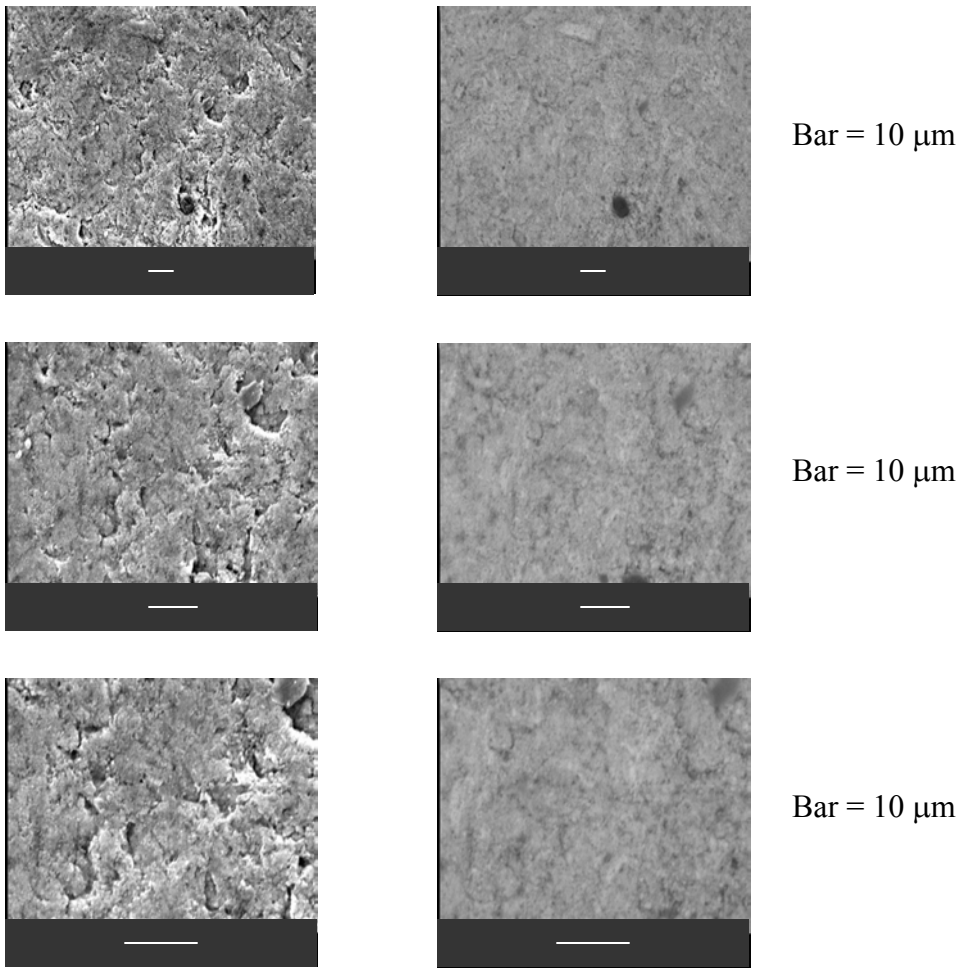

Figure 3.22. SEM micrographs for $Bi_{1.6}Pb_{0.4}Sr_2Nb_2TiO_{12-\delta}$ using (a) SE detection and (b) BSE detection.

Figure 3.23 depicts the backscattered electron image of the region utilized for EDS analysis for specimen $Bi_{1.6}Pb_{0.4}Sr_2Nb_2TiO_{12-\delta}$. A gray matrix and a potential bright region are depicted in the micrograph in addition to some porosity. Figures 3.24 and 3.25 show the EDS spectra of the two regions obtained for the x = 0.0 sample. Both regions contain bismuth, strontium, niobium titanium, and lead. There is no discrepancy between the qualitative EDS spectra of the surface of $Bi_{1.6}Pb_{0.4}Sr_2Nb_2TiO_{12-\delta}$. The XRD data presented in section *3.2.2.1* indicated the presence of a single phase at x = 0.0. EDS analysis shows that the two potentially different regions in the sample contain all of the elements in the 3-layer $Bi_{1.6}Pb_{0.4}Sr_2Nb_2TiO_{12-\delta}$ Aurivillius structure. In conjunction with the x-ray data, it is reasonable to conclude that the x = 0.0 sample is phase pure.

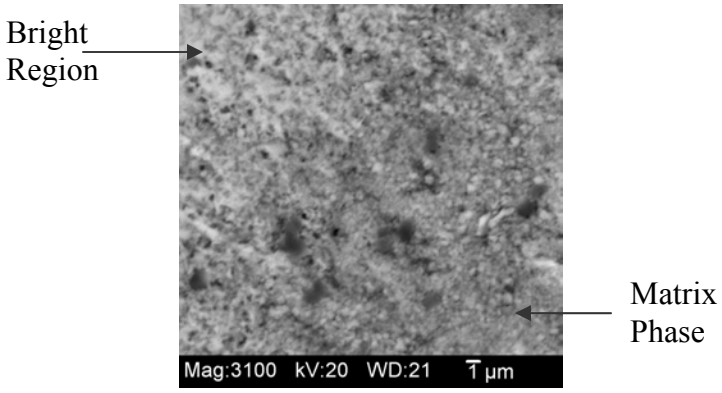

Figure 3.23. Backscattered electron image of the region of $Bi_{1.6}Pb_{0.4}Sr_2Nb_2TiO_{12-\delta}$ that was utilized for EDS analysis.

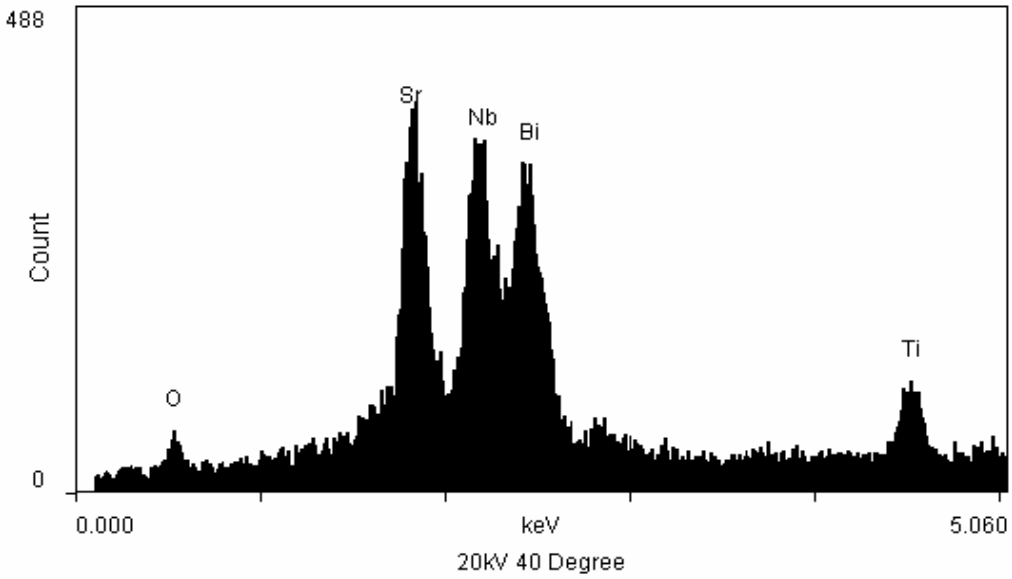

Figure 3.24. EDS spectrum for the gray matrix of composition $Bi_{1.6}Pb_{0.4}Sr_2Nb_2TiO_{12-\delta}$.

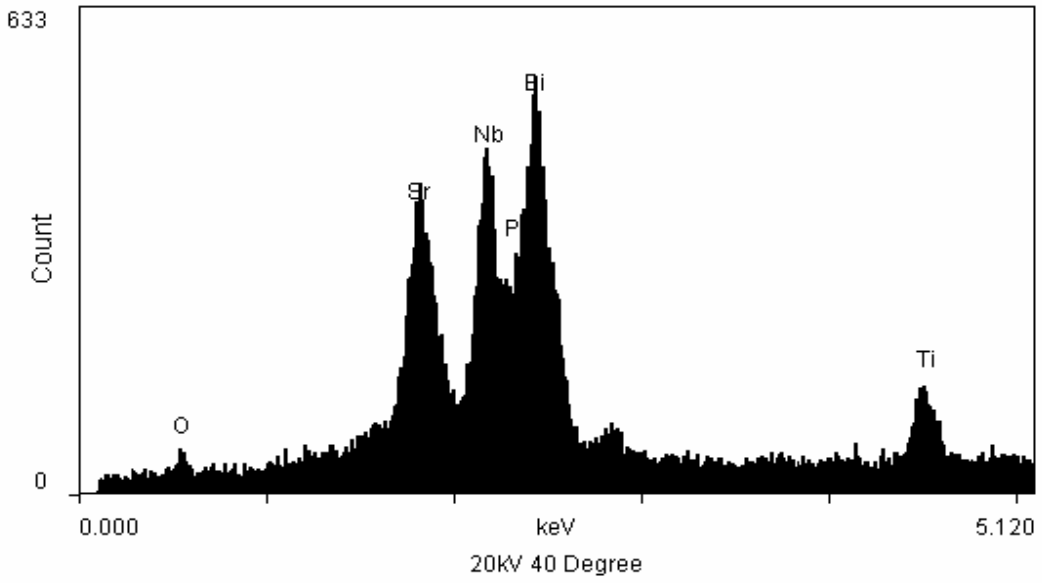

Figure 3.25. EDS spectrum of the bright phase of composition $Bi_{1.6}Pb_{0.4}Sr_2Nb_2TiO_{12-\delta}$.

3.4.2 Microstructural Analysis of $Bi_{1.6}Pb_{0.4}Sr_2Nb_2Ti_{0.8}Al_{0.2}O_{12-\delta}$

Scanning electron micrographs and EDS data was acquired for $Bi_{1.6}Pb_{0.4}Sr_2Nb_2Ti_{0.8}Al_{0.2}O_{12-\delta}$. Figure 3.26 shows the SEM micrographs generated for $Bi_{1.6}Pb_{0.4}Sr_2Nb_2Ti_{0.8}Al_{0.2}O_{12-\delta}$ prepared by the polymerized complex method. Composition x = 0.2 contains a matrix, and what appears to be a gray phase in addition to some porosity. The gray region appears to be distributed randomly throughout the matrix.

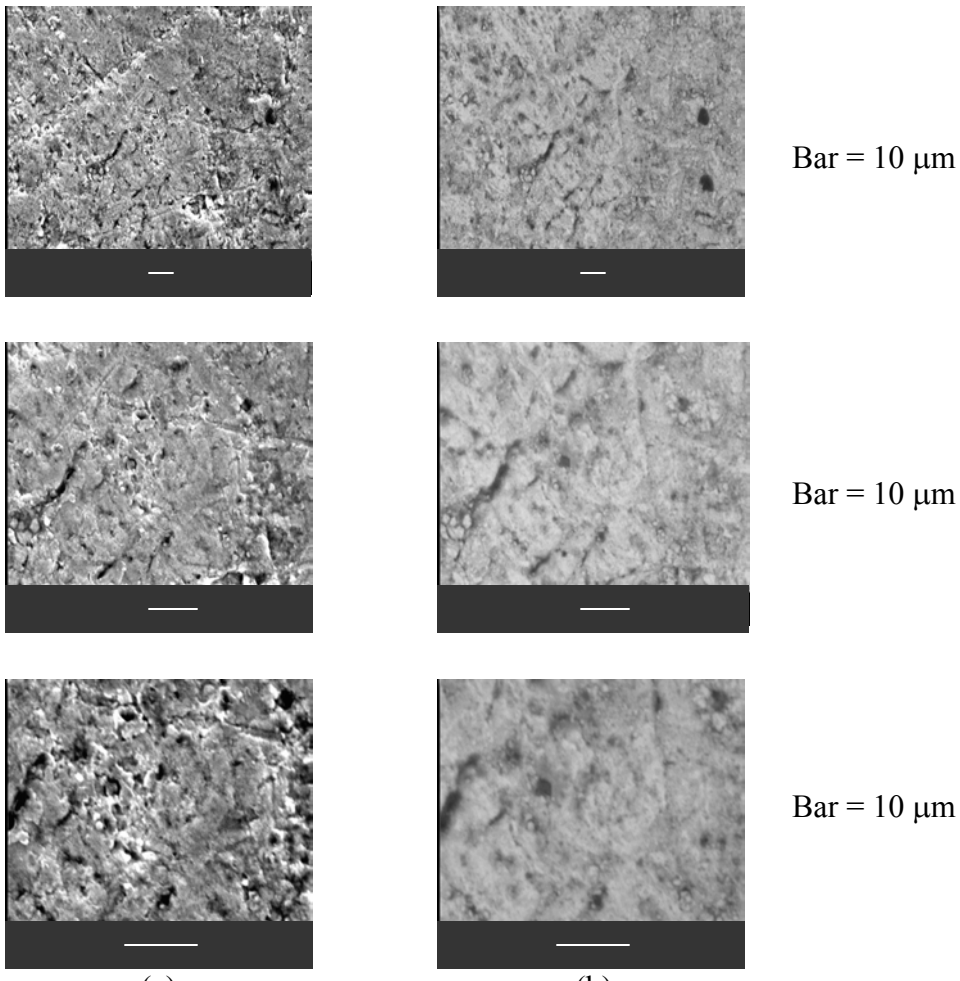

Figure 3.26. SEM micrographs for $Bi_{1.6}Pb_{0.4}Sr_2Nb_2Ti_{0.8}Al_{0.2}O_{12-\delta}$ under (a) SE detection and (b) BSE detection.

Figure 3.27 depicts the backscattered electron image of the region utilized for EDS analysis for specimen $Bi_{1.6}Pb_{0.4}Sr_2Nb_2Ti_{0.8}Al_{0.2}O_{12-\delta}$. The matrix and gray region are both present in the image. Figures 3.28 and 3.29 show the EDS spectra obtained for this sample. Similar to specimen x = 0.0 both phases contain all of the elements present in the $Bi_{1.6}Pb_{0.4}Sr_2Nb_2Ti_{0.8}Al_{0.2}O_{12-\delta}$ composition. The secondary gray phase has a significantly larger quantity of aluminum however. The existence of a second phase at this composition stands in opposition to the x-ray diffraction data in section *3.2.2.1*, which showed a phase pure specimen at x = 0.2. There is no discrepancy between the two qualitative EDS spectra with respect to the bismuth, lead, strontium, niobium, and titanium elements however. As such, when considering both the x-ray and EDS data, it is reasonable to conclude that the matrix and what appears to be a gray phase both exist as an Aurivillius structure. Two Aurivillius phases of slightly different composition would also help to explain the broad peaks witnessed in the x-ray diffraction patterns. It is also possible that the secondary gray region is due to topographical effects.

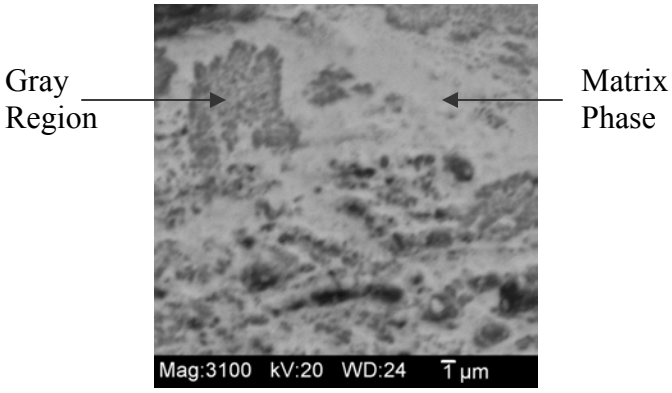

Figure 3.27. Backscattered electron image of the region of $Bi_{1.6}Pb_{0.4}Sr_2Nb_2Ti_{0.8}Al_{0.2}O_{12-\delta}$ that was utilized for EDS analysis.

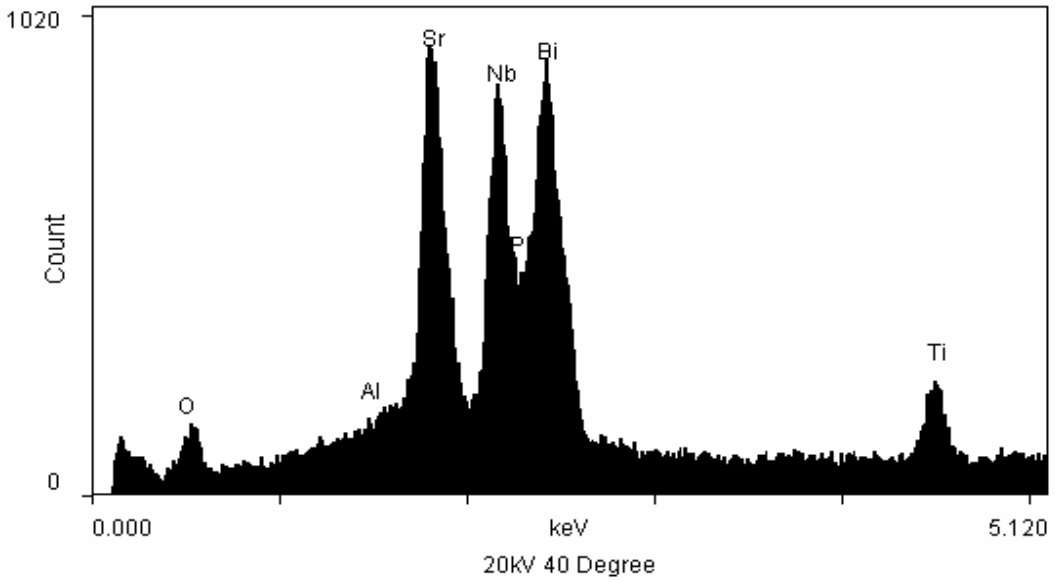

Figure 3.28. EDS spectrum of the matrix of composition $Bi_{1.6}Pb_{0.4}Sr_2Nb_2T_{0.8}Al_{0.2}O_{12-\delta}$.

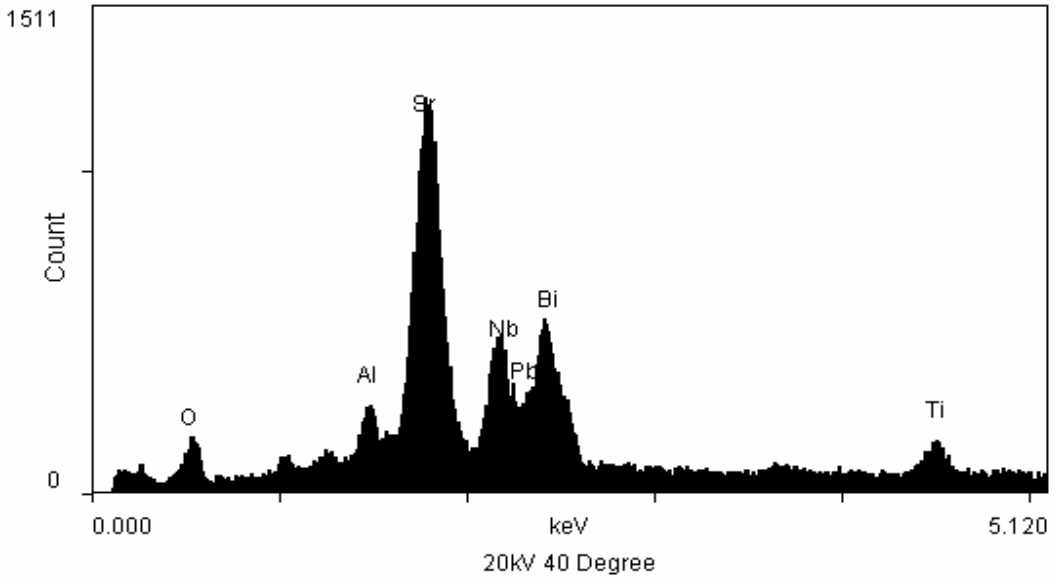

Figure 3.29. EDS spectrum of the gray phase of composition $Bi_{1.6}Pb_{0.4}Sr_2Nb_2T_{0.8}Al_{0.2}O_{12-\delta}$.

3.4.3 Microstructural Analysis of $Bi_{1.6}Pb_{0.4}Sr_2Nb_2Ti_{0.4}Al_{0.6}O_{12-\delta}$

Scanning electron micrographs and EDS data was acquired for $Bi_{1.6}Pb_{0.4}Sr_2Nb_2Ti_{0.4}Al_{0.6}O_{12-\delta}$. Figure 3.30 shows the SEM micrographs generated for $Bi_{1.6}Pb_{0.4}Sr_2Nb_2Ti_{0.4}Al_{0.6}O_{12-\delta}$ prepared by the polymerized complex method. Composition x = 0.6 contains a matrix, a gray phase and an elongated rectangular dark phase. Grains of the gray phase have become larger and more prevalent at this composition. In addition, it is clear that the dark phase has adopted a rectangular morphology.

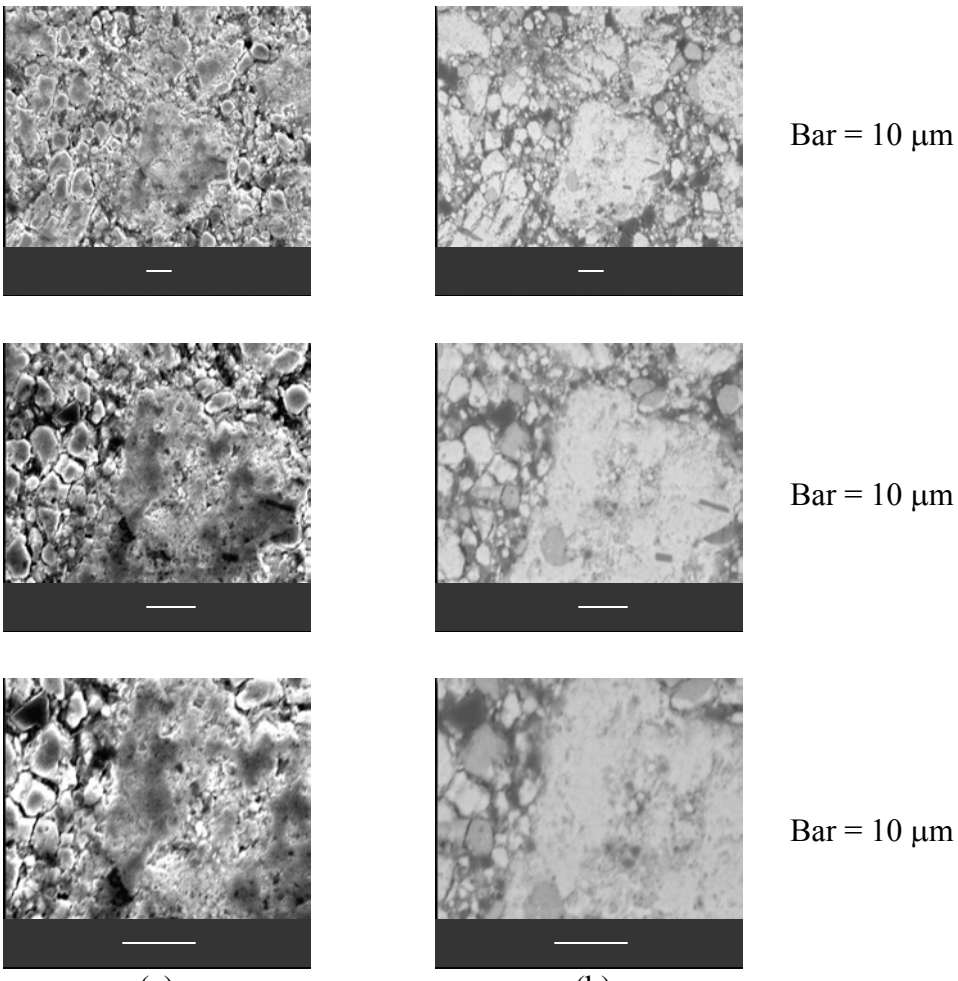

Figure 3.30. SEM micrographs for $Bi_{1.6}Pb_{0.4}Sr_2Nb_2Ti_{0.4}Al_{0.6}O_{12-\delta}$ using (a) SE detection and (b) BSE detection.

Figure 3.31 depicts the backscattered electron image of the region scanned for EDS analysis for specimen $Bi_{1.6}Pb_{0.4}Sr_2Nb_2Ti_{0.4}Al_{0.6}O_{12-\delta}$. A matrix, gray phase, and dark phase are present in the image. Figures 3.32 to 3.34 show the EDS spectra of the three phases obtained for this sample. The x-ray diffraction results presented in section *3.2.2.1* indicated the evolution of two additional phases at x = 0.6. This conclusion is supported by the SEM data. The matrix appears as the brightest phase under BSE detection. EDS analysis confirms that the matrix contains all of the elements in the Aurivillius structure. Similar to composition x = 0.2 however, there is very little aluminum substitution evident in the matrix. Most of the aluminum has formed in the secondary phases. There are significant amounts of strontium and aluminum in the gray phase and elongated dark phase. The secondary phases appear to be aluminum-strontium oxides. It is evident from EDS that titanium and lead only exist in the matrix. The interaction area of the EDS analysis, on the order of 5 μm, is larger than the grain size of the secondary phases. As a consequence there will be some interaction with the matrix, resulting in the niobium and bismuth peaks in the EDS spectra of the gray and dark phases.

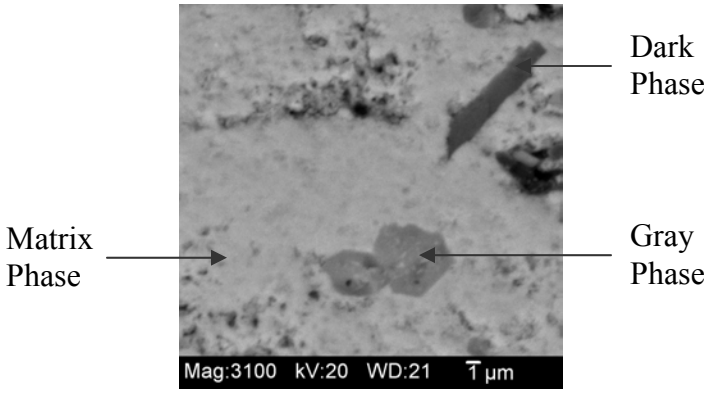

Figure 3.31. Backscattered electron image of the region of $Bi_{1.6}Pb_{0.4}Sr_2Nb_2Ti_{0.4}Al_{0.6}O_{12-\delta}$ that was utilized for EDS analysis.

Conspicuously absent is the presence of bismuth oxide, which was clearly forming in the x-ray diffraction patterns at x = 0.6. Bismuth oxide must appear as a brighter phase in backscattered electron imaging. At this point it is not possible to conclusively determine the location of the Bi_2O_3. It is possible that the grain size of bismuth oxide is small enough so that it is not possible to image them with the SEM and they are distributed throughout the secondary phases.

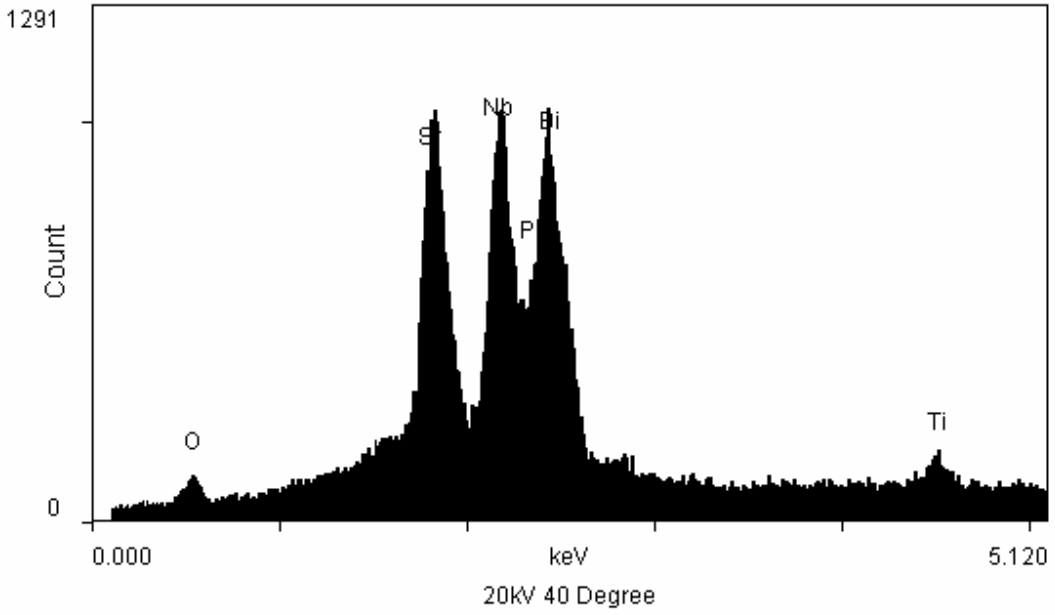

Figure 3.32. EDS spectrum of the matrix of composition $Bi_{1.6}Pb_{0.4}Sr_2Nb_2T_{0.4}Al_{0.6}O_{12-\delta}$.

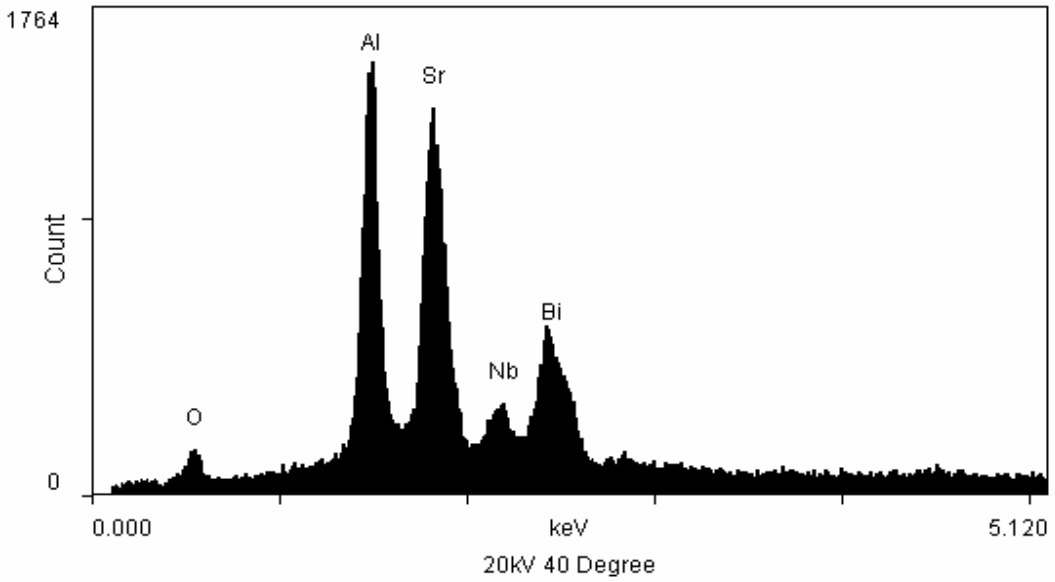

Figure 3.33. EDS spectrum of the gray phase of composition $Bi_{1.6}Pb_{0.4}Sr_2Nb_2T_{0.4}Al_{0.6}O_{12-\delta}$.

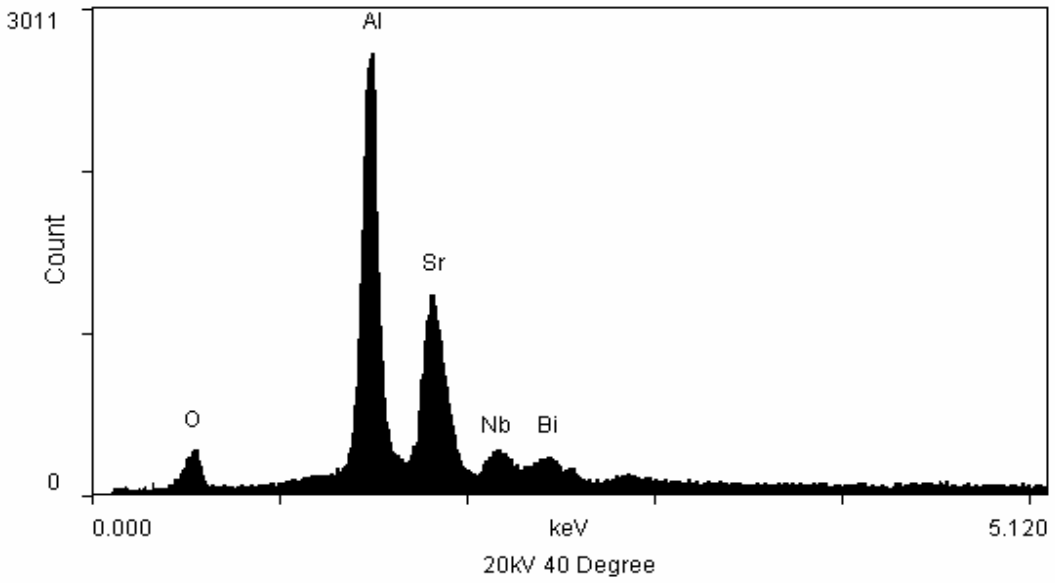

Figure 3.34. EDS spectrum of the dark phase of composition $Bi_{1.6}Pb_{0.4}Sr_2Nb_2T_{0.4}Al_{0.6}O_{12-\delta}$.

3.4.4 Microstructural Analysis of $Bi_{1.6}Pb_{0.4}Sr_2Nb_2Ti_{0.2}Al_{0.8}O_{12-\delta}$

Scanning electron microscope images and EDS data was acquired for $Bi_{1.6}Pb_{0.4}Sr_2Nb_2Ti_{0.2}Al_{0.8}O_{12-\delta}$. Figure 3.35 shows the SEM micrographs generated for $Bi_{1.6}Pb_{0.4}Sr_2Nb_2Ti_{0.2}Al_{0.8}O_{12-\delta}$ prepared by the polymerized complex method. Composition x = 0.8 contains a matrix, and substantial secondary phases depicted as a gray phase and an elongated dark phase. Grains of the gray phase have increased in size compared to specimen x = 0.6 and occupy a larger percentage of the area. Furthermore, the dark phase has also become more prevalent while maintaining its elongated shape.

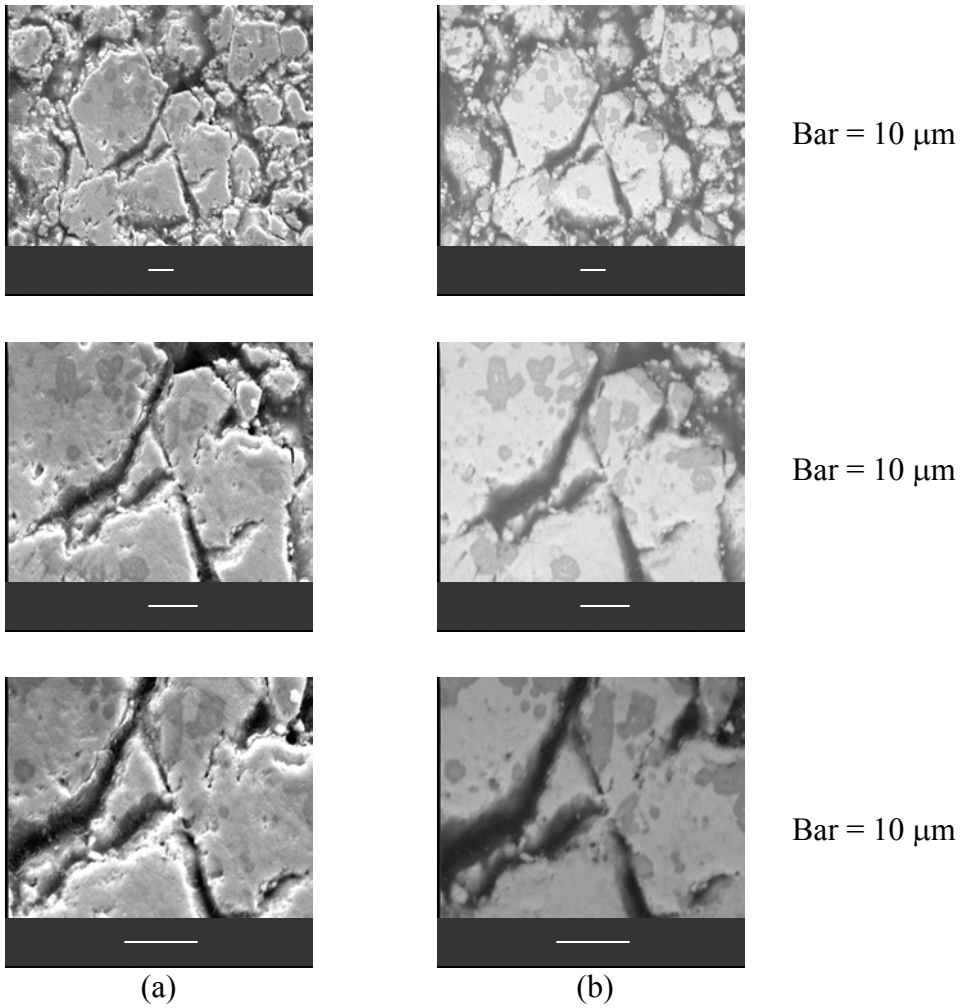

Figure 3.35. SEM micrographs for $Bi_{1.6}Pb_{0.4}Sr_2Nb_2Ti_{0.2}Al_{0.8}O_{12-\delta}$ using (a) SE detection and (b) BSE detection.

Figure 3.36 depicts the backscattered electron image of the region scanned for EDS analysis for specimen $Bi_{1.6}Pb_{0.4}Sr_2Nb_2Ti_{0.2}Al_{0.8}O_{12-\delta}$. A matrix, as well as multiple grains of the gray and dark phases are all present in the image. Figures 3.37 to 3.39 show the EDS spectra of the three phases obtained for this sample. The trend involving the evolution of multiple phases has developed further at x = 0.8. The x-ray diffraction data presented in section *3.2.2.1* showed relative growth and sharpening of the secondary phase peaks as well as the Aurivillius peaks. BSE images show the continued growth and distribution of secondary phase grains. Similar to the x = 0.6 composition, EDS analysis of the matrix at x = 0.8 shows the presence of the elements in the $Bi_{1.6}Pb_{0.4}Sr_2Nb_2Ti_{0.2}Al_{0.8}O_{12-\delta}$ sample. The titanium peak is only present in the matrix but has decreased due to increased aluminum content. Almost all of the aluminum is present in the secondary phases. From the EDS spectra the secondary phases appear to be aluminum-strontium oxides. The apparent presence of bismuth and niobium is due to the interaction area of the EDS, on the order of 5 μm, which is larger than the grain size. X-ray diffraction data of $Bi_{1.6}Pb_{0.4}Sr_2Nb_2Ti_{0.2}Al_{0.8}O_{12-\delta}$ showed the evolution of bismuth oxide, which is missing from the SEM images. It is not possible to conclusively say where the bismuth oxide is located, as it should appear as a brighter region with backscattered electron imaging. It is possible that the Bi_2O_3 grains are small enough that they cannot be imaged with the SEM and are distributed within the secondary phases.

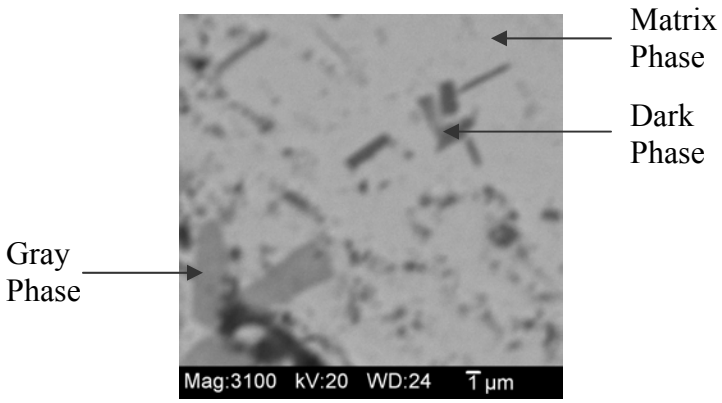

Figure 3.36. Backscattered electron image of the region of $Bi_{1.6}Pb_{0.4}Sr_2Nb_2Ti_{0.2}Al_{0.8}O_{12-\delta}$ that was utilized for EDS analysis.

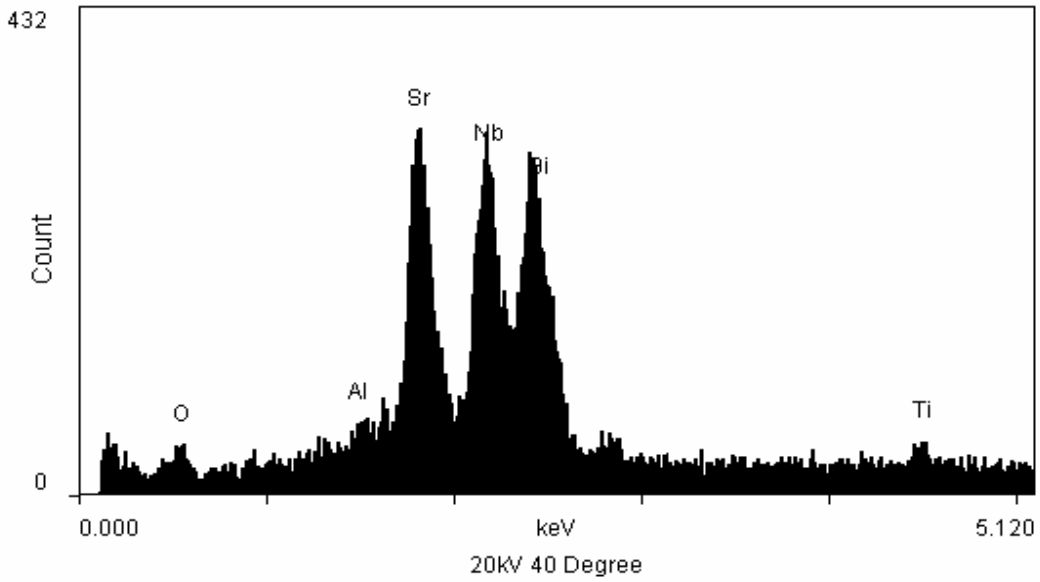

Figure 3.37. EDS spectrum of the matrix of composition $Bi_{1.6}Pb_{0.4}Sr_2Nb_2T_{0.2}Al_{0.8}O_{12-\delta}$.

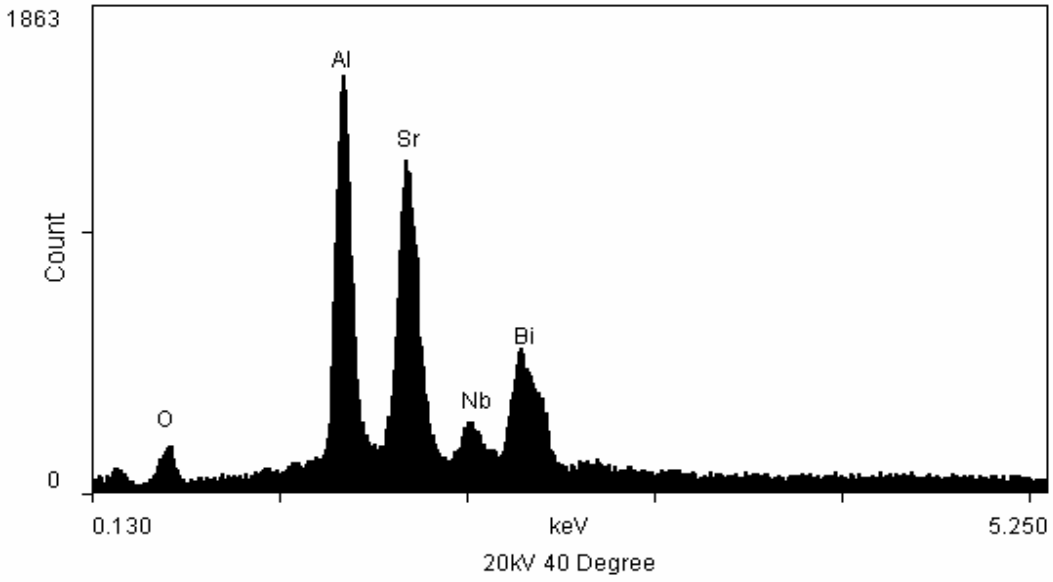

Figure 3.38. EDS spectrum of the gray phase of composition $Bi_{1.6}Pb_{0.4}Sr_2Nb_2T_{0.2}Al_{0.8}O_{12-\delta}$.

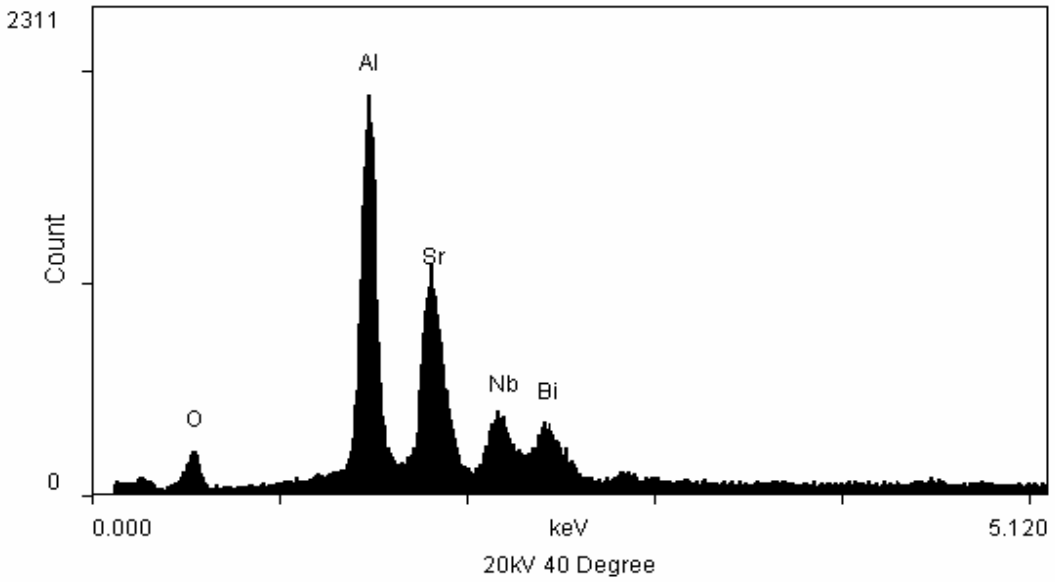

Figure 3.39. EDS spectrum of the dark phase of composition $Bi_{1.6}Pb_{0.4}Sr_2Nb_2T_{0.2}Al_{0.8}O_{12-\delta}$.

3.5 $La_{1-x}Sr_xCoO_3$ Crystal Structure Characterization

The composition $La_{1-x}Sr_xCoO_3$ ($0.1 \leq x \leq 0.9$) was synthesized by the polymerized complex method and heat-treated to 1200°C for 15 hours in air. Figures 3.40 and 3.41 show diffraction patterns at the extremes of the compositional range, when $x = 0.1$ and $x = 0.9$. According to the X-ray diffraction results, the $La_{1-x}Sr_xCoO_3$ powders were single-phase materials. The peak splitting that occurred at high concentration levels of lanthanum decreased with the addition of strontium before disappearing at $x = 0.7$. Introduction of strontium ions onto the lanthanum site causes a structural change at $x = 0.6$. The larger ionic radius of strontium gradually decreased the distortion from rhombohedral symmetry to cubic symmetry.

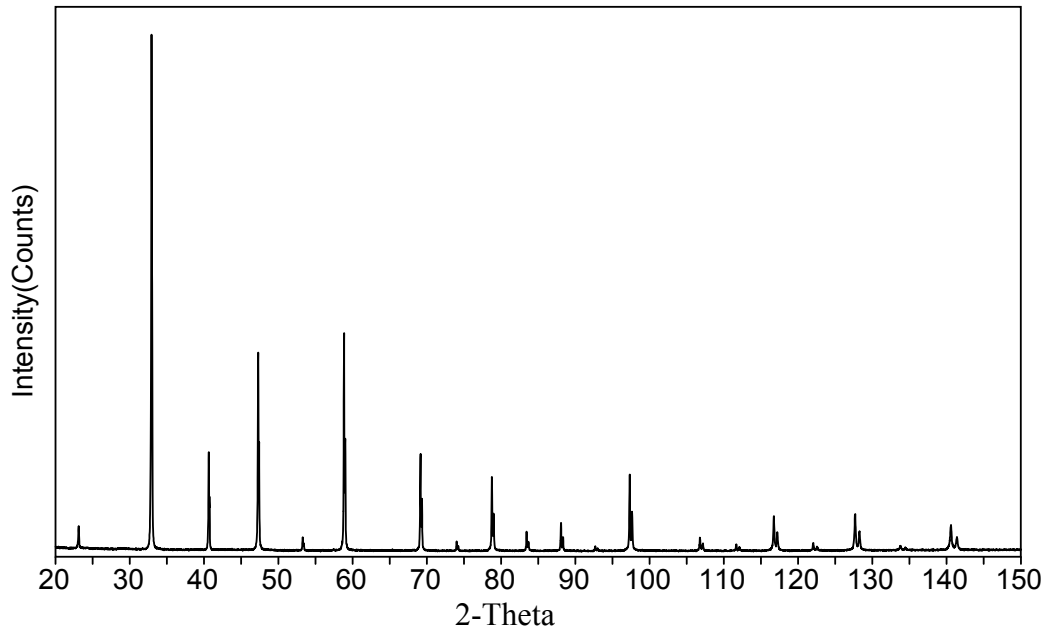

Figure 3.40. X-ray diffraction pattern for $La_{0.1}Sr_{0.9}CoO_3$ utilized in the Rietveld refinement.

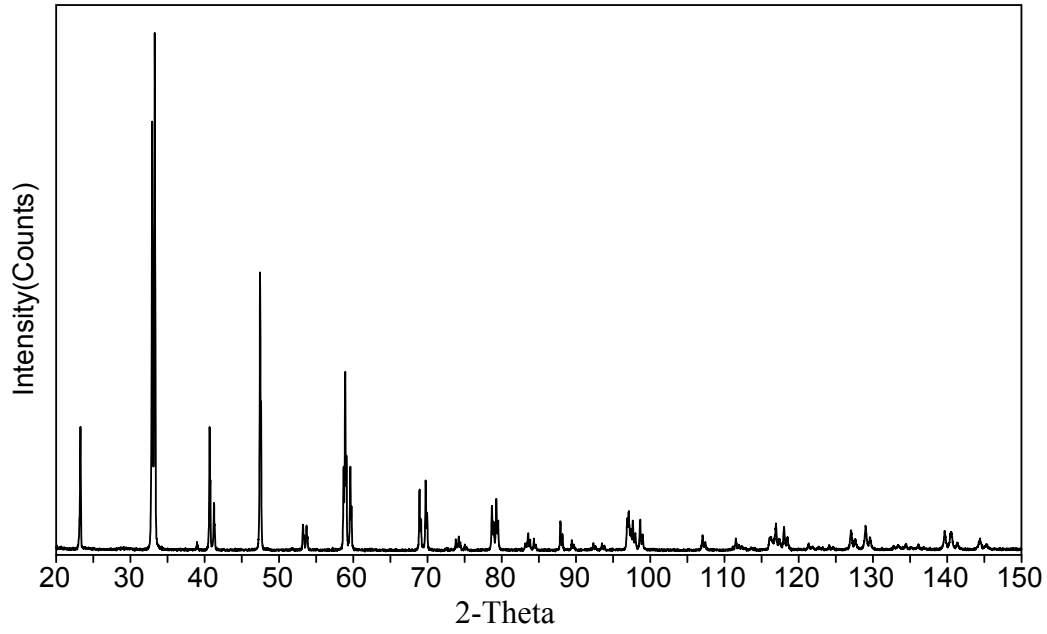

Figure 3.41. X-ray diffraction pattern for $La_{0.9}Sr_{0.1}CoO_3$ utilized in the Rietveld refinement.

Table III-5 lists the crystallographic data for $La_{1-x}Sr_xCoO_3$ while Table III-6 details the weighted pattern residual error (R_{wp}) and goodness of fit (gof) that was calculated for the corresponding composition.

Table III-5. Unit Cell Metrics and Rietveld Refinement Results for $La_{1-x}Sr_xCoO_3$.

Composition	a (Å)	Angle	Cell Volume ($Å^3$)	Density (g/cm^3)	Crystal System
X = 0.1	5.3935(9)	60.6866(9)	112.66	7.10	rhombohedral
X = 0.2	5.403(1)	60.565 (1)	112.93	6.93	rhombohedral
X = 0.3	5.407(1)	60.447 (1)	112.92	6.78	rhombohedral
X = 0.4	5.410(6)	60.320(6)	112.76	6.64	rhombohedral
X = 0.5	5.412(2)	60.218(2)	112.67	6.49	rhombohedral
X = 0.6	5.416(4)	60.080(4)	112.52	6.65	rhombohedral
X = 0.7	3.833(1)	90.0	56.32	6.19	cubic
X = 0.9	3.838(1)	90.0	56.53	6.17	cubic

Table III-6. Goodness of Fit Indicators from the Rietveld Refinement for $La_{1-x}Sr_xCoO_3$.

Composition	R (weighted pattern)	χ (goodness-of-fit)
X = 0.1	12.36	1.22
X = 0.2	11.82	1.24
X = 0.3	11.34	1.21
X = 0.4	8.34	1.73
X = 0.5	11.05	1.28
X = 0.6	8.92	1.73
X = 0.7	7.63	1.48
X = 0.9	7.11	1.30

$La_{1-x}Sr_xCoO_3$ exists as a cubic unit cell from $0.7 \leq x \leq 0.9$ and as a rhombohedral unit cell from $0.1 \leq x \leq 0.5$. At $0.6 \leq x \leq 0.9$ the (110) plane is responsible for the reflection at 33° 2-θ. From $0.1 \leq x \leq 0.6$ the appearance of the (012) plane in addition to the (110) plane is causing the doublet at 33° 2-θ. The a-axis in the cubic unit cell increased with strontium concentration from 3.833(1) Å at x = 0.7 to 3.838(9) Å at x = 0.9 as expected from the solid solution. Similarly, the rhombohedral a-axis also consistently increased with strontium concentration while the unit cell angle decreased from 5.3935(6) Å and 60.6866(6)° at x = 0.1 to 5.416(4) Å and 60.080(4)° at x = 0.6. Figure 3.42 details the effect of strontium substitution on the rhombohedral lattice parameter and cell angle. The density of $La_{1-x}Sr_xCoO_3$, which was calculated from the diffraction data, gradually decreased from 7.10 g/cm^3 at x = 0.1 to 5.87 g/cm^3 at x = 0.9. Figure 3.43 shows the change in density with composition. The cell volume for the rhombohedral unit cell decreased with strontium substitution from 112.93 Å^3 to 112.52 Å^3 between x = 0.2 and x = 0.6. The $La_{0.9}Sr_{0.1}CoO_3$ cell volume represents an outlier and could not be refined to a reasonable value. When the crystal system changes to cubic at x = 0.7, however, the cell volume begins to increase with the addition of strontium from 56.32 Å^3 at x = 0.7 to 56.53 Å^3 at x = 0.9. The relationship between cell volume and composition is plotted in figure 3.44. The volume of the cubic unit cells was doubled so that the data of the two crystal systems could be plotted on the same axis.

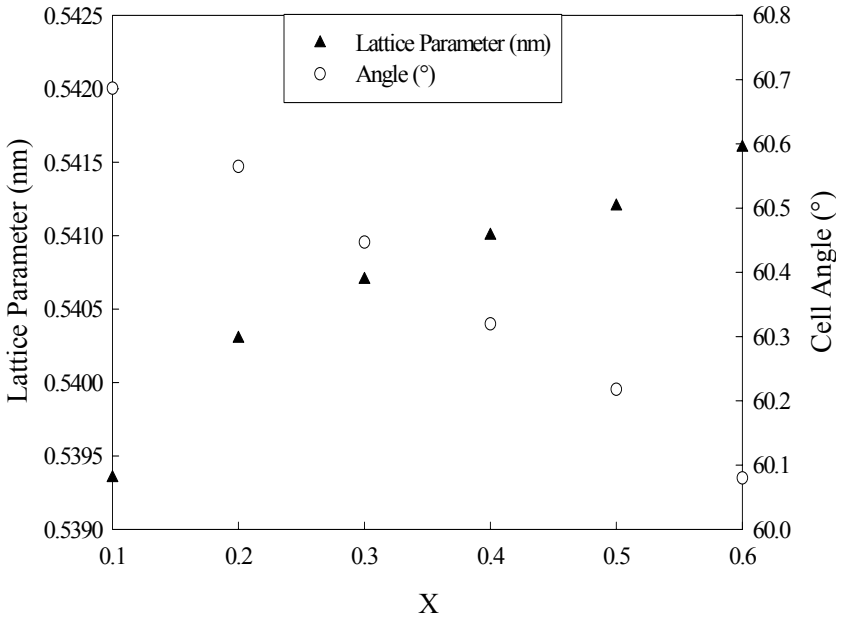

Figure 3.42. The rhombohedral lattice parameter and cell angle of $La_{1-x}Sr_xCoO_3$ with increasing values of x. The error bars are smaller than the size of the data points.

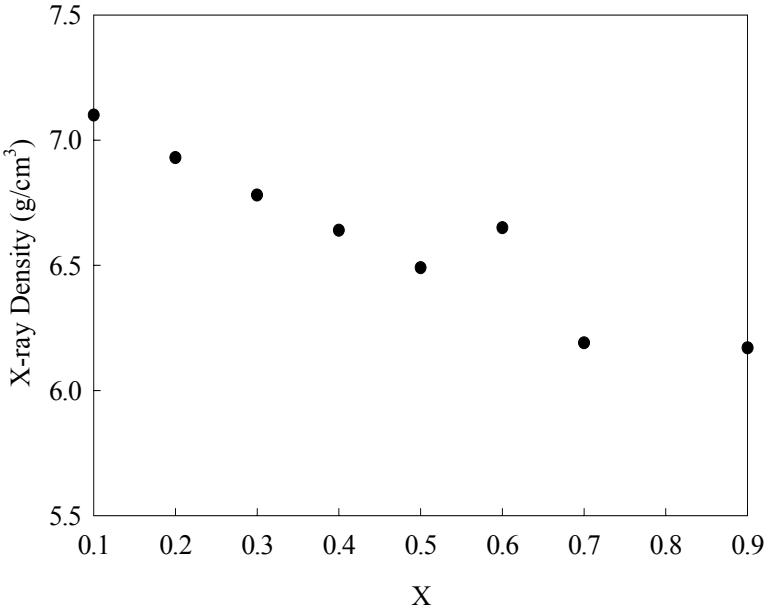

Figure 3.43. The cell density of $La_{1-x}Sr_xCoO_3$ with increasing values of x, calculated from the x-ray data.

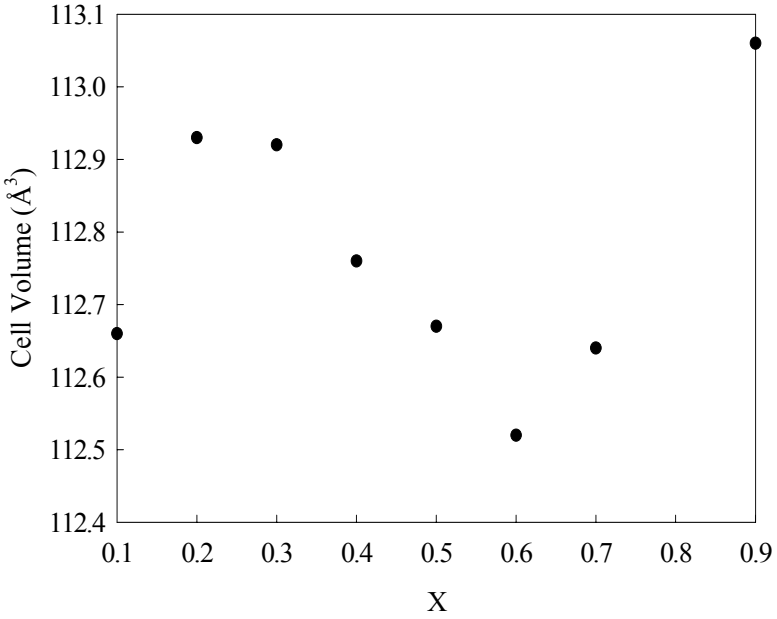

Figure 3.44. The unit cell volume of $La_{1-x}Sr_xO_3$ with increasing values of x. The error bars are smaller than the size of the data points.

The reference intensity ratio of $La_{1-x}Sr_xCoO_3$ to corundum (I/I_C) was made from the 100% lines of $La_{1-x}Sr_xCoO_3$ at 33° 2-theta and corundum at 43° 2-theta. The average of three runs at each composition was calculated and is reported in table III-6.

Table III-6. The I/I_C Values with Standard Deviation for $La_{1-x}Sr_xCoO_3$ from $0.1 \leq x \leq 0.5$.

Composition	I/I_C	S.D.
X = 0.5	3.61	0.31
X = 0.3	3.22	0.07
X = 0.1	3.23	0.08

The largest ratio is obtained at composition x = 0.5. Peak splitting that is occurring in the other two samples reduces the absolute intensity of the 100% line. Although $La_{0.5}Sr_{0.5}CoO_3$ exists in a rhombohedral unit cell there is, as yet, not much evidence of peak splitting. As a result, the I/I_C values for x = 0.1 and x = 0.3 are lower.

4. Summary

Three layer Aurivillius specimens of the type $Bi_2Sr_2Nb_2TiO_{12}$ and $Bi_{1.6}Pb_{0.4}Sr_2Nb_2Ti_{1-x}Al_xO_{12-\delta}$ ($0.0 \leq x \leq 0.8$) in steps of 0.2 were synthesized by the polymerized complex method. Infrared, ICP-OE, and NMR spectroscopy were used to characterize the solution chemistry. Infrared spectroscopy indicated the formation of an ester upon polymerization at 170°C from the shift of the carbonyl peak from 1735 cm^{-1} to 1715 cm^{-1}. In addition, IR spectra obtained for solutions that contained ammonium hydroxide showed the formation of an amide after polymerization was completed at 170°C. Proton NMR spectra supported the conclusions drawn from IR analysis. Elemental analysis of condensed solvent by ICP-OES showed with 95% confidence that at least to some degree all of the cations in the $Bi_2Sr_2Nb_2TiO_{12}$ structure were volatilizing out with the solvent.

X-ray diffraction data was used to investigate phase purity among the compositions and determine crystal structure information. $Bi_2Sr_2Nb_2TiO_{12}$ was processed as a phase pure sample after 5 hours of heating in air at 900°C. Some sharpening of the peaks occurred after 10 additional hours of firing at 900°C. Broad peaks in the XRD patterns are likely due to stacking faults that were not annealed out in the short firing cycle or to small crystallite size. In experiments where the solution pH was raised to 9.00 phase purity was obtained after firing to only 700°C for 5 hours. As such, it can be concluded that the production of an amide during synthesis does not inhibit the formation of the fired oxide. In addition, although it was qualitatively determined that there is some loss in stoichiometry from ICP-OES, a 3-layer Aurivillius structure was still formed.

$Bi_{1.6}Pb_{0.4}Sr_2Nb_2Ti_{1-x}Al_xO_{12-\delta}$ was processed from $0.0 \leq x \leq 0.8$ in steps of 0.2. Multiple phases were formed for $x \geq 0.4$. The x-ray diffraction data in section *3.2.2.1* indicated phase pure specimens at $x = 0.0$ and $x = 0.2$. SEM-BSE analysis showed, however, that a possible secondary phase of higher atomic number compared to the Aurivillius phase existed when $x = 0.0$ and a possible third phase of lower atomic number at $x = 0.2$. Elemental EDS analysis showed that all of the elements in the $Bi_{1.6}Pb_{0.4}Sr_2Nb_2Ti_{1-x}Al_xO_{12-\delta}$ composition were present in both regions. It is likely that

the suspect secondary phases are in reality Aurivillius structures with slightly different compositions. At x = 0.4 aluminum substitution however, three phases began to evolve. The second and third phases appear to be strontium-aluminum oxides. The bismuth oxide, which x-ray diffraction clearly showed evolving beyond x = 0.4 could not be identified in the SEM. As the aluminum content was increased to x = 0.6 and x = 0.8 the peaks corresponding to the Aurivillius structure sharpened and increased in intensity. The broad peaks at low levels of x might then be due to stacking faults stemming from crystal structure strain. The tetragonal lattice parameters of $Bi_{1.6}Pb_{0.4}Sr_2Nb_2Ti_{1-x}Al_xO_{12-\delta}$ decreased non-linearly over the compositional range studied, thus showing that aluminum is substituted into the Aurivillius crystal structure for titanium even beyond the apparent solubility limit. The a-axis decreased from 0.4035 nm at x = 0.0 to 0.3851 nm at x = 0.8. The c-axis also declined from 3.4388 nm at x = 0.0 to 3.3015 nm at x = 0.8.

The electrical behavior of $Bi_{1.6}Pb_{0.4}Sr_2Nb_2Ti_{1-x}Al_xO_{12-\delta}$ followed what was occurring with the phase and vacancy formations. The conductivity increased from 1.74 x 10^{-4} S•cm^{-1} when x = 0.0 to 4.76 x 10^{-3} S•cm^{-1} when x = 0.8. The parent $Bi_2Sr_2Nb_2TiO_{12}$ exhibits a conductivity on the order of 10^{-5} S/cm. The conductivity also rose slightly between compositions of x = 0.0 and x = 0.2 where the conductivity was 2.2 x 10^{-4} S•cm^{-1}, thus showing an effect from vacancy formation. The large jump in conductivity between x = 0.2 and x = 0.6 is due at least in part to the presence of bismuth oxide in the specimens.

$La_{1-x}Sr_xCoO_3$ was synthesized by the polymerized complex method in the range $0.0 \leq x \leq 0.9$. Rietveld refinement yielded unit cell metrics. $La_{1-x}Sr_xCoO_3$ exists as a cubic crystal system from $0.7 \leq x \leq 0.9$ and as a rhombohedral crystal system from $0.1 \leq x \leq 0.6$. The a lattice parameter in the cubic unit cell ranged from 3.833(1) Å at x = 0.7 to 3.838(9) Å at x = 0.9. The a lattice parameter and cell angle in the rhombohedral unit cell ranged from 5.3935(9) Å and 60.6866(9)° at x = 0.1 to 5.416(4) Å and 60.080(4)° at x = 0.6. The cell density consistently decreased with strontium addition from 7.10 g/cm^3 at x = 0.1 to 6.17 g/cm^3 at x = 0 .9.

5. Conclusions

The polymerized complex method was successfully employed to synthesize $Bi_{1-y}Pb_ySr_2Nb_2Ti_{1-x}Al_xO_{12-\delta}$ (x = 0.0 and x = 0.2) (y = 0.0 and 0.4) at 900°C in air for 5 hours and $La_{1-x}Sr_xCoO_3$ ($0.0 \leq x \leq 0.9$) at 1200°C in air for 15 hours. An amide forms in addition to an ester with the addition of ammonium hydroxide to control solution pH. Phase pure $Bi_2Sr_2Nb_2TiO_{12}$ was synthesized at 700°C in air for 5 hours when the solution pH was raised to 9.00. Additional phases begin to form for $Bi_{1.6}Pb_{0.4}Sr_2Nb_2Ti_{1-x}Al_xO_{12-\delta}$ at $x \geq 0.4$. The conductivity of $Bi_{1.6}Pb_{0.4}Sr_2Nb_2Ti_{1-x}Al_xO_{12-\delta}$ ranged from 4.76×10^{-3} $S \bullet cm^{-1}$ at x = 0.8 to 1.74×10^{-4} $S \bullet cm^{-1}$ at x = 0.0. $La_{1-x}Sr_xCoO_3$ adopts a cubic unit cell between $0.9 \leq x \leq 0.7$ and a rhombohedral cell from $0.6 \leq x \leq 0.1$.

References

1) D.C. Harris, *Quantitative Chemical Analysis*, 5th ed.; Ch. 14. W.H. Freeman and Company, New York, 1999.

2) N.Q. Minh, "Ceramic Fuel Cells," *J. Am. Ceram. Soc.*, **76** [3] 563-568 (1993).

3) B.C.H. Steele, "Materials Engineering and Fuel Cell Development," *MRS Bull.*, **14** [6] 19-23 (1989).

4) B.C.H. Steele, "Materials for Electrochemical Energy Conversion and Storage Systems," *Ceram. Int.*, **19** [4] 269-277 (1993).

5) K.R. Kendall, C. Navas, J.K. Thomas, and H.C. zur-Loye, "Recent Developments in Oxide Ion Conductors: Aurivillius Phases," *Chem. Mater.*, **8** [3] 642-649 (1996).

6) K.R. Kendall, C.N. Navas, J.K. Thomas, and H.C. zur-Loye, "Recent Developments in Perovskite-based Oxide Ion Conductors," *Solid State Ionics*, **82** [4] 215-223 (1995).

7) C.G. Vayenas, S.I. Bebelis, and C.C. Kyriazis, "Cogeneration: Electricity + Chemicals Part 1: Solid Electrolytes?," *Chem. Technol.*, **21**, 422-428 (1991).

8) B. Aurivillius, "Mixed Bismuth Oxides with Layer Lattices," *Ark. Kemi*, **1**, 499-512 (1949).

9) J.K. Thomas, M.E. Anderson, W.E. Krause, and H.C. zur-Loye, "Oxygen Ion Conductivitiy in a New Class of Layered Bismuth Oxide Compounds," *Mater. Res. Soc. Symp. Proc.*, **293**, 295-299 (1993).

10) K.R. Kendall, J.K. Thomas, and H.C. zur-Loye, "Synthesis and Ionic Conductivity of a New Series of Modified Aurivillius Phases," *Chem. Mater.*, **718** [1] 50-57 (1995).

11) V.B. Modi, "Electrical and Microstructural Characterization of N=3 Type Aurivillius Phases"; M.S. Thesis, Alfred University, Alfred, NY, 2002.

12) A. Snedden, S.M. Blake, and P. Lightfoot, "Oxide Ion Conductivity in Ga-Doped Aurivillius Phases-a Reappraisal," *Solid State Ionics*, **156** [2] 439-445 (2003).

13) S.M. Blake, M.J. Falconer, M. McCreedy, and P. Lightfoot, "Cation Disorder in Ferroelectric Aurivillius Phases of the Type $Bi_2ANb_2O_9$ (A = Ba, Sr, Ca)," *J. Mater. Chem.*, **7** [8] 1609-1613 (1997).

14) C.H. Hervoches and P. Lightfoot, "Cation Disorder in Three-Layer Aurivillius Phases: Structural Studies of $Bi_{2-x}Sr_{2+x}Ti_{1-x}Nb_{2+x}O_{12}$ ($0 \leq x \leq 0.8$) and $Bi_{4-x}La_xTi_3O_{12}$ (x = 1 and 2)," *J. Solid State Chem.*, **153** [1] 66-73 (2000).

15) T. Rentschler, M. Karus, A. Wellm, and A. Reller, "Synthesis and Characterization of the Aurivillius Phases $Bi_{2-x}Pb_xSr_{1-x}Nd_xNb_2O_9$," *Solid State Ionics*, **90** [1] 49-55 (1996).

16) T. Rentschler, "Substitution of Lead into the Bismuth Oxide Layers of the n = 2 and n = 3 – Aurivillius Phases," *Mater. Res. Bull.*, **32** [3] 351-369 (1997).

17) C. Say, "Electrical and Compositional Study of N=3 Aurivillius Structures for Oxygen Conducting Devices"; M.S. Thesis, Alfred University, Alfred, NY, 2002.

18) S.A. Speakman, "The Crystal Chemistry of Brownmillerite and n = 3 Aurivllius-Type Ceramic Conductors for Fuel Cell Applications"; Ph.D. Thesis, Alfred University, Alfred, NY, 2002.

19) R.D. Shannon, "Revised Effective Ionic Radii and Systematic Studies of Interatomic Distances in Halides and Chalcogenides," *Acta. Cryst. A*, **32** [5] 751-766 (1976).

20) D.C. Sinclair and A.R. West, "Impedance and Modulus Spectroscopy of Semiconducting $BaTiO_3$ Showing Positive Temperature Coefficient of Resistance," *J. Appl. Phys.*, **66** [8] 3850-3856 (1989).

21) A.R. West, D.C. Sinclair, and N. Hirose, "Characterization of Electrical Materials, Especially Ferroelectrics, by Impedance Spectroscopy," *J. Electroceram.*, **1** [1] 65-71 (1997).

22) J.R. Macdonald, *Impedance Spectroscopy: Emphasizing Solid Materials and Systems*. Ch. 1-2. Wiley and Sons, New York, 1987.

23) M. Kakihana and K. Domen, "The Synthesis of Photocatalysts Using the Polymerizable-Complex Method," *MRS Bull.*, **21** [9] 27-31 (2000).

24) R. Maalal, M. Manier, J.P. Mercurio and J. Frit, "Grain Oriented $B_7Ti_4NbO_{21}$ Ceramics," *Silic. Ind.*, **59** [5-6] 161-163 (1994).

25) W.J. Yu, Y.I. Kim, D.H. Ha, J.H. Lee, Y.K. Par, S. Seong, and N.H. Hur, "A New Manganese Oxide with the Aurivillius Structure: $Bi_2Sr_2Nb_2MnO_{12-\delta}$," *Solid State Commun.,* **111** [12] 705-709 (1999).

26) R. Maalal, M. Manier, and J.P. Mercurio, "Dielectric Properties of the Mixed Aurivillius Phases $M^{II}Bi_8Ti_7O_{27}$ (M^{II} = Ca, Sr, Ba, and Pb)," *J. Eur. Ceram. Soc.,* **15** [11] 1135-1140 (1996).

27) K.M. Fox, "Synthesis and Characterization of Layered Aurivillius-Derived Ionic Conductors"; B.S. Thesis, Alfred University, Alfred, NY, 2000.

28) S.R. Wagner, "Synthesis and Characterization of Layered Aurivillius-Derived Ionic Conductors"; B.S. Thesis, Alfred University, Alfred, NY, 1999.

29) M. Pechini, "Method of Preparing Lead and Alkaline Earth Titanates and Niobates and Coating Method Using the Same to Form a Capacitor," U.S. Pat. 3,330,697, 1967.

30) K. Huang and J.B. Goodenough, "Wet Chemical Synthesis of Sr- and Mg- Doped $LaGaO_3$, a Perovskite-Type Oxide-Ion Conductor," *J. Solid State Chem.*, **136** [2] 274-283 (1998).

31) P.A. Lessing, "Mixed-Cation Oxide Powders via Polymeric Precursors," *Am. Ceram. Soc. Bull.*, **68** [5] 1002-1007 (1989).

32) P. Duran, F. Capel, C. Moure, M. Villegas, J.F. Fernandez, J. Tartaj, and A.C. Caballero, "Processing and Dielectric Properties of the Mixed-Layer Bismuth Titanate Niobate $Bi_7Ti_4NbO_{21}$ by the Metal-Organic Precursor Synthesis Method," *J. Eur. Ceram. Soc.*, **21** [1] 1-8 (2001).

33) S. M. Zanetti, E.B. Araujo, E.R. Leite, E. Longo, and J.A. Varela, "Structural and Electrical Properties of $SrBi_2Nb_2O_9$ Thin Films Prepared by Chemical Aqueous Solution at Low Temperature," *Mater. Lett.*, **40** [1] 33-38 (1999).

34) F.M. Pontes, E. Longo, E.R. Leite, and J.A. Varela, "Study of the Dielectric and Ferroelectric Properties of Chemically Processed $Ba_xSr_{1-x}TiO_3$," *Thin Solid Films*, **386** [1] 91-98 (2001).

35) B.D. Stojanovic, C.R. Foschini, M. Cilense, M.A. Zaghete, A.A. Cavalheiro, C.O. Paiva-Santos, E. Longo, and J.A. Varela, "Structural Characterization of Organometallic-Derived 9.5/65/35 PLZT Ceramics," *Mater. Chem. Phys.*, **68** [2] 136-141 (2001).

36) O. Schulz and M. Martin, "Preparation and Characterization of $La_{1-x}Sr_xGa_{1-y}Mg_yO_{3-(x+y)/2}$ for the Investigation of Cation Diffusion Processes," *Solid State Ionics*, **135** [3] 549-555 (2000).

37) H.U. Anderson, M.J. Pennell, and J.P. Guha, "Polymeric Synthesis of Lead Magnesium Niobate Powders," pp. 91-98 in Advances in Ceramics, Vol. 21, *Ceramic Powder Science*. Edited by G.L. Messing. American Ceramic Society, Westerville, OH. 1987.

38) W. Liu, G.C. Farrington, F. Chaput, and B. Dunn, "Synthesis and Electrochemical Studies of Spinel Phase $LiMn_2O_4$ Cathode Materials Prepared by the Pechini Process," *J. Electrochem. Soc.*, **143** [3] 879-882 (1996).

39) C.P. Udawatte, M. Kakihana, and M. Yoshimura, "Low Temperature Synthesis of Pure $SrSnO_3$ and the $(Ba_xSr_{1-x})SnO_3$ Solid Solution by the Polymerized Complex Method," *Solid State Ionics*, **128** [4] 217-226 (2000).

40) C.P. Udawatte, M. Kakihana, and M. Yoshimura, "Preparation of Pure Perovskite Type $BaSnO_3$ Powders by the Polymerized Complex Method at Reduced Temperature," *Solid State Ionics*, **108** [1] 23-30 (1998).

41) T.MT.N. Tennakoon, G. Lindbergh, and B. Bergman, "Performance of $LiCoO_2$ Cathodes, Prepared Using the Pechini Method, in Molten Carbonate Fuel Cells," *J. Electrochem. Soc.*, **144** [7] (1997).

42) M.K. Kakihana, M.M. Milanova, M. Arima, T. Akubo, M. Yashima, and M. Yoshimura, "Polymerized Complex Route to Synthesis of Pure $Y_2Ti_2O_7$ at 750 °C Using Yttrium-Titanium Mixed-Metal Citric Acid Complex," *J. Am. Ceram. Soc.*, **79** [6] 1673-1676 (1996).

43) M. Hrovat, N. Katsarakis, K. Reichmann, S. Bernik, D. Kuscer, and J. Holc, "Characterization of $LaNi_{1-x}Co_xO_3$ as a Possible SOFC Cathode Material," *Solid State Ionics*, **81** [2] 99-105 (1996).

44) T. Nobunaga, K. Okamoto, N. Miura, and N. Yamazoe, " Influence of Constituent Metal Cations in Substituted $LaCoO_3$ on Mixed Conductivity and Oxygen Permeability," *Solid State Ionics,* **48** [3] 207-212 (1991).

45) J.F.M. Cillessen, R.M. Wof, and A.E.M. DeVeirman, "Hetero-Epitaxial Oxidic Conductor $La_{1-x}Sr_xCoO_3$ Prepared by Pulsed Laser Deposition," *Appl. Surf. Sci.*, **69** [2] 212-215 (1993).

46) V. Craciun and D. Craciun, "Droplet Formation during Extended Time Pulsed Laser Deposition of $La_{0.5}Sr_{0.5}CoO_3$ Thin Layers," *J. Appl. Phys.*, **85** [5] 3310-3313 (1999).

47) H. Huang, "Preparation, Electrical Properties and Phase Compatibility Studies of $La_{1-x}Sr_xCoO_3$ for Electrode Applications in Ceramic Multilayer Devices"; M.S. Thesis, Alfred University, Alfred, NY, 2000.

48) H. Ohbayashi, T. Kudo, and T. Gejo, "Crystallographic, Electric and Thermochemical Properties of the Perovskite-Type $La_{1-x}Sr_xCoO_3$ (Ln: Lanthanoid Element)," *Jpn. J. Appl. Phys.*, **13** [1] 1-7 (1974).

49) Powder Diffraction File (PDF-2), [CD-ROM] Database Sets 1-47; International Center for Diffraction Data, Newton Square, PA, 2000.

50) Chemical Database Service Program, Inorganic Crystal Structure Database (ICSD) [CD-ROM] Daresbury Laboratory, Warrington, UK, 1998.

51) J. Kirchnerova and D.B. Hibbert, "Vacancy Ordering in $La_{1-x}Sr_xCoO_3$ Prepared by Calcination of Freeze-Dried Powders of Nitrates," *MRS Bull.*, **25** [5] 585-592 (1990).

52) Jade v.6.0.3 [Computer Program] Materials Data, Livermore, CA, 2002.

53) Bruker AXS, *TOPAS V2.0:* General Profile Analysis Software for Powder Diffraction Data. - User Manual. Bruker AXS, Karlsruhe, Germany, 2000.

54) J. McMurry, *Organic Chemistry*, 4^{th} ed.; pp. 439-446, 464-466. Brooks/Cole, Pacific Grove, CA, 1996.